Applications of FM Noise Radar Waveforms: Spatial Modulation and Polarization Diversity

By

Garrett D Zook

Submitted to the graduate degree program in Electrical Engineering and the Graduate Faculty of the University of Kansas in partial fulfillment of the requirements for the degree of Master of Science.

Dr. Shannon Blunt, Chair

Committee members

Dr. Christopher Allen

Dr. James Stiles

Date defended: 08/24/2018

The Thesis Committee for Garrett D Zook certifies
that this is the approved version of the following thesis :

Applications of FM Noise Radar Waveforms: Spatial Modulation and Polarization Diversity

Dr. Shannon Blunt, Chair

Date approved: 08/24/2018

Abstract

Two possible radar application spaces are explored through the exploitation of high-dimensional nonrecurrent FM-noise waveforms. The first involving a simultaneous dual-polarized emission scheme that provides good separability with respect to co- and cross-polarized terms and the second mimicking the passive actuation of the human eye with a MIMO emission. A waveform optimization scheme denoted as pseudo-random optimized (PRO) FM has been shown to generate FM-noise radar waveforms that are amenable to high power transmitters. Each pulse is generated and optimized independently and possesses a non-repeating FM-noise modulation structure. Because of this the range sidelobes of each pulse are unique and thus are effectively suppressed given enough coherent integration.

The PRO-FM waveform generation scheme is used to create two independent sets of FM-noise waveforms to be incorporated into a simultaneous dual-polarized emission; whereby two independent PRO-FM waveforms will be transmitted simultaneously from orthogonal polarization channels. This effectively creates a polarization diverse emission. The random nature of these waveforms also reduce cross-correlation effects that occur during simultaneous transmission on both channels. This formulation is evaluated using experimental open-air measurements to demonstrate the effectiveness of this high-dimensional emission.

This research aims to build upon previous work that has demonstrated the ability to mimic fixational eye movements (FEM) employed by the human eye. To implement FEM on a radar system a MIMO capable digital array must be utilized in conjunction with spatial modulation beamforming. Successful imitation of FEM will require

randomized fast-time beamsteering from a two-dimensional array. The inherent randomness associated with FEM will be paired with the PRO-FM waveforms to create an emission possessing randomness in the space and frequency domains, called the FEM radar (FEMR). Unlike traditional MIMO, FEMR emits a coherent and time-varying beam. Simulations will show the inherent enhancement to spatial resolution in two-dimensional space (azimuth and elevation) relative to standard beamforming using only the matched filter to process returns.

Acknowledgements

Sponsored by the Office of Naval Research (ONR) under Contract #N00014-16-C-2029.

Contents

List of Figures

List of Tables

Chapter 1

Introduction

Since its inception in the early 1900s radar systems have improved in all aspects quite dramatically, though the fundamental operation and physics contributing to its continued success and innovation has not. The advent of arrays and increasingly complex digital signal processing both on transmit and receive has improved the ability for radar systems to interrogate the environment [2–5]. The advent of arbitrary waveform generation capabilities and adaptive signal processing techniques has continued to solve the problems that past generations of radar engineers once thought impossible. This work explores multiple facets of *waveform diversity* [6–10] and the applications it has to polarization diverse [11, 12] and spatially diverse emissions [13, 14] like multiple-input multiple-output (MIMO) [15–18].

Traditional polarization diverse radar systems transmit LFM (or LFM-like) waveforms using either an interleaved or simultaneous pulse schedule. There are benefits and hindrances associated with both emission styles. Transmitting LFMs simultaneously on orthogonal polarizations introduces ambiguity since the transmitted waveforms are very similar. By instead utilizing an emission that never repeats in the form of FM-noise waveforms the ability to separate co-polarized and cross-polarized responses is improved. A portion of this work is motivated by biological sensing animals that exhibit exceptional performance characteristics across a wide breadth of environments and applications [19]. Observing the product of thousands of years of evolution and mimicking the functionality and processing techniques employed by biological sensor systems could lead to better performance in man-made systems. The pseudo-random optimized (PRO) FM waveform optimization scheme is used throughout this work to create random FM-noise emissions [20]. The primary motivation for this work stems from exploring the flexibility of the PRO-FM waveform

and the many potential applications it has across multiple facets of radar. While this work focuses only on the application of the PRO-FM waveform (explained in detail in section 2.10) to polarization and and spatial modulation, other FM-noise waveforms could be used in its place ([21] for example). The application of FM noise waveforms to cognitive spectrum sensing [22], radar and communications spectrum cohabitation [23–31], and other various applications have been explored [32–35].

This work is organized into five main chapters with the second providing background knowledge of basic radar principles and phenomenology required to fully understand the third and fourth, finishing with a conclusions and future work chapter. Contained within the background chapter are the concepts used to formulate and evaluate the two applications of FM-noise radar described within the proceeding chapters. Chapter 2 includes descriptions of basic radar system parameters and fundamental equations/relationships. Concepts like pulse compression, signal-to-noise ratio, and bandwidth are considered in detail.

Chapter 3 provides the formulation and analysis of a simultaneous dual-polarized emission scheme. The approach described within exploits the high-dimensionality of two independently generated sets of PRO-FM waveforms that provide good cross-correlation between orthogonal polarization channels. Good cross-correlation equates good co- and cross-polarization separation [36]. This emission scheme will be compared with traditional full polarimetric emissions. The goal is to provide an emission that does not require computationally expensive processing on transmit or receive but instead draws its benefits from coherent integration and high dimensionality. The benefits of such an approach is estimation of coherent polarimetric scattering matrices that could potentially lead to enhanced target discrimination.

In Chapter 4 the waveform diverse array is expanded upon to facilitate random fast-time steering of a coherent beam to mimic the fixational eye movements (FEM) observed by mammals possessing fovea [37–39]. This fast-time dithering of the coherent mainbeam is referred to spatial modulation [1, 40–44]. Waveform degrees of freedom will be exploited by pairing random spatial modulation with the PRO-FM noise waveform to add an additional level of randomness [20, 45].

This work was motivated by interest in biomimetic radar systems due to the exceptional performance demonstrated by natural sensors [19, 46–48]. Just as the human eye aids in cognition, the approach described here could be used as the emission scheme for cognitive radar modes of operation [49].

Chapter 2

Background

To fully understand the concepts and methods described within this work one must first be familiar with basic radar phenomenology, notation, and functions. This chapter will introduce relevant fundamentals as well as more narrowed topics leveraged for this research. Specialized derivations and extrapolations pertaining to the unique emission schemes described in this work are placed within the corresponding research chapters (3 and 4), but build upon the basic concepts outlined here. This chapter provides a brief introduction to radar and some of the concepts leveraged for this work. Though every minute detail of how a radar system functions will not be explained, the relevant information, theorems, and concepts will. An in-depth commentary on the many facets of radar can be found in [50–53] with many practical examples of real systems and implementations therein.

2.1 Pulse Repetition Interval

Radars that transmit pulsed waveforms do so during short time intervals called the pulse width, designated by T_{p}. During the pulse width an amplified electromagnetic signal is emitted into the environment. Unless the radar possesses a separate receive antenna, the receiver of the system will be switched off during transmission to avoid being damaged by the (typically) high-powered transmitter. Once the pulse has been sent the radar then listens for an allotted time to collect reflected target echoes before transmitting another pulse. The time between starting points of adjacent pulses is called the pulse repeition interval or *PRI*. To explain this parameter consider the example transmission schedule shown in Figure 2.1. This figure displays a sequence of time

delayed pulses, each possessing pulsewidth, T_p, representing the time that the transmitter is turned on. The space between pulses is separated by the dead time (or listening time) determined as $(PRI - \tau)$.

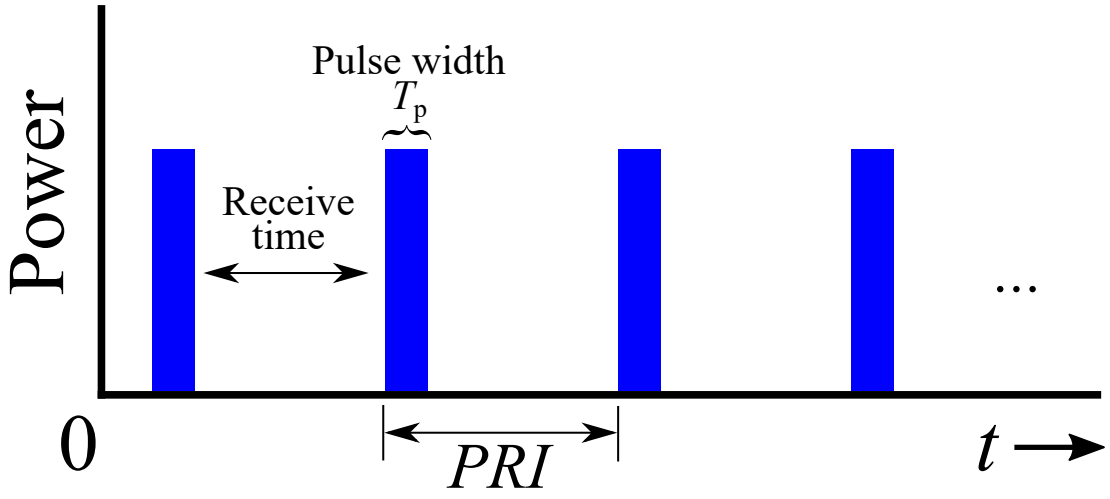

Figure 2.1: A pulsed radar transmission schedule.

The ranging ability of a radar system is determined by the time delay from the moment a pulse is transmitted to the moment the reflected pulse is received. This time delay is then converted to range by knowing the propagation rate of the pulse through air (or perhaps dirt/ice for ground penetrating radars). In Figure 2.1 the pulses (shown in blue) are spaced by the receive time of the system. The target returns corresponding to each pulse must fall within the proper receive time for each received echo to be considered unambiguous in range. If a return from pulse ℓ arrives during the receive time of pulse $\ell + 1$, an example situation is shown in Figure 2.2, then the radar signal processor will think that target is closer than its true range. To avoid this situation the *PRI* is determined on a system-specific basis. Long-range radars typically have long *PRI*'s and short range radars typically have short *PRI*'s. Although the previous statement is not always 100% correct, due to other system constraints and the use of *PRI* staggering or even multiple *PRI*s. On the most basic level, determining the proper *PRI* is required to reduce or eliminate the possibility

of receiving ambiguous range data from scatterers.

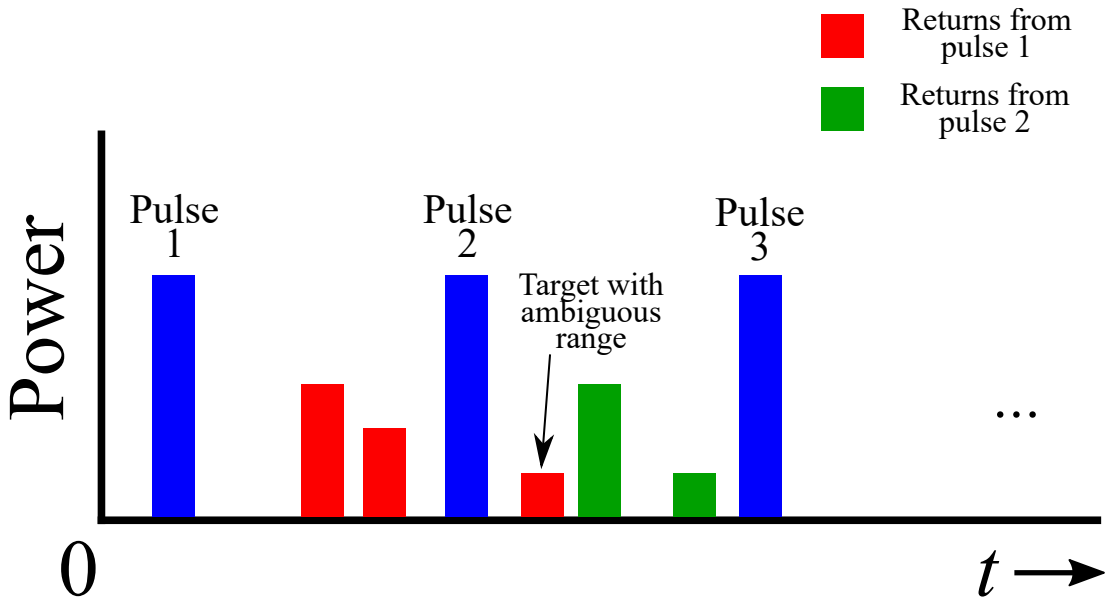

Figure 2.2: A pulsed radar transmission schedule.

Similar to *PRI*, the number of pulse cycles that the radar system performs per second is called the pulse repetition frequency, or *PRF*. The *PRF* is related to the system's *PRI* and maximum range by

$$PRF = \frac{1}{PRI} = \frac{c}{2R_{\max}}. \tag{2.1}$$

The use of *PRI* and *PRF* is often interchangeable when describing this parameter. The maximum unambiguous range of a radar system is determined by the propagation time required to receive the echoes of each transmitted pulse at the maximum range of interest. Typically this parameter is used when determining a starting point for a system's *PRF*. This can be found by solving (2.1) for the maximum range as

$$R_{\max} = \frac{c}{2\,PRF}. \tag{2.2}$$

As described above, correctly choosing this parameter can determine whether the system performs as intended. However, as will be described later in section 2.7, there is a trade-space to determining the PRF for radar system due to its relationship to Doppler frequency.

2.2 Radar Cross Section

The radar cross section (RCS) of a scatterer is a fabricated representation of the cross-sectional area being illuminated as a function of the target's aspect angle and the transmit center frequency of the radar system. The formal definition of a scatterer's radar cross section is

$$\sigma = \lim_{R \to \infty} 4\pi R^2 \frac{|E_{Rx}|^2}{|E_{Tx}|^2} \tag{2.3}$$

where R is the range from radar to target, E_{Rx} is the scattered (or received) electric field strength, and E_{Tx} is the strength of the incident electric field [53]. From this definition a simple observation can be made: the RCS of a target is simply the range-dependent ratio of reflected to incident power densities. A scatterer's RCS, using the above definition, is the projected area of a metal sphere that would scatter the incident power identically to the target. From (2.3), note that the determination of RCS relies heavily on range.

This simple representation relies on the transmitted wavelength being much larger than the modeled metallic sphere. When considering target aspect angle of even the simplest targets this model begins to break down because RCS varies greatly depending on the viewing angle of the scatterer [53]. This, coupled with the reflectivity of the target, creates a characteristic that is unique to each aspect angle of every target [54]. Accurate modeling and comprehensive analysis of the RCS of specific objects becomes increasingly important, especially when considering that, at certain aspect angles, the RCS of a human, artillery round, and fighter jet are the same [55–58].

2.3 Signal-to-Noise Ratio

One of the most important parameters to any radar system is the signal-to-noise ratio (SNR). As described by its name, the SNR is a ratio of the received signal power to the received noise power, which measures (at the simplest level) the detectability of an illuminated target. Should the received echo possess a power level much lower than that of the received noise then the target will

be undetectable without further processing. The simplest form of the SNR equation, for the monostatic case, is described by

$$\frac{P_r}{P_n} = SNR = \frac{P_t G_t G_r \lambda^2 \sigma}{(4\pi)^3 R^4 k T_s B} \tag{2.4}$$

where G_t is the gain of the transmit antenna, G_r is the gain of the receive antenna, λ is the wavelength corresponding to the center frequency, σ is the target RCS, R is the range from the radar to the target, k is Boltzmann's constant, T_s is the system noise temperature, and B is the instantaneous bandwidth of the system. This equation provides a good baseline calculation for initial choices of radar parameters and simple simulations. This equation can be extrapolated to the bistatic case as well [59]. To provide more realistic insight into how a system might perform, consider the extrapolation of (2.4) to

$$SNR = \frac{G_t G_r \lambda^2 \sigma n_{\mathrm{p}}}{(4\pi)^3 R^4 k T_{\mathrm{s}} B L_{\mathrm{s}}} \tag{2.5}$$

which incorporates the use of multiple pulses (n_{p}) and system losses (L_{s}). A processing gain can be achieved by coherently integrating the responses of adjacent pulses. Most radar systems implement some form of coherent integration and multiple pulse processing to benefit from this gain. The number of pulses or length of time over which multiple pulses are processed is called the coherent processing interval (*CPI*). This equation can be solved for any number of variables, such as range, minimum detectable RCS, or required antenna gain, to facilitate determination of radar numerous system parameters.

2.4 Pulse Compression

The three fundamental parameters of a transmit radar waveform that can be adjusted within the pulse duration are phase, frequency, and amplitude. Changing one or more of these three attributes imposes the corresponding modulation type onto said waveform. By introducing an intra-pulse modulation the pulse is said to be compressed. Amplitude modulation (AM) was one of the first modulation schemes to be used commercially [60] and primarily for radio communications. The use of AM in radar introduces several potential problems including range limitations due to time-

varying transmit power, inability for transmit amplifiers to maintain saturation region operation, and various target return losses compounding with time-varying power leading less detectable returns. In practice, amplitude modulation is typically not used unless considering the transition between transmitter on and off states. The next, and most popular, form of pulse compression involves modulating the frequency of the emission in both intra-pulse and inter-pulse implementations. Frequency modulation (FM) includes both linear modulations, LFM for example, and nonlinear modulations, such as nonlinear chirps [10, 61]. Phase modulation or phase coded waveforms are created by forming a set of subpulses, called chips, where each chip contains a phase value. These phase coded waveforms can be poly-phase (such as the implementation described in section 2.9) or bi-phase where there are only two phase states.

Pulse compression in radar provides a processing gain proportional to the time-bandwidth product (BT) of the transmitted pulse. The BT of a signal, like the name suggests, is the product of the bandwidth and pulse-duration. This value is often used to gauge the dimensionality of the signal with values ranging from unity to 10^6 or more [20, 50]. Creating a pulse compressed radar waveform involves the imposition of an intra-pulse modulation that maintains the average power budget while extending the bandwidth, B, beyond the $1/T_{\mathrm{p}}$ (time-frequency) relationship. The overarching term used to describe the selection of the modulation to be imposed upon the radar signal given required system constraints and desired performance parameters falls under the umbrella of *waveform design*. An exhaustive background on the subject of waveform design and *waveform diversity* is given in [6].

2.4.1 The Matched Filter and Correlation

Received signals are filtered within the receiver to enhance target detection by improving the signal-to-noise ratio. As mentioned above, better SNR equates improved target detectability and better performance for the radar system. A very desirable property of pulse compression waveforms is the ability to create, store, and process returns with a copy of the emission. Filtering a modulated signal, defined as $s(t)$, with a version of itself is called *matched filtering* (MF). The use

of the matched filter assumes that received echoes from targets and clutter are amplitude-scaled and time-shifted copies of the transmit waveform. Thus we can define the MF as

$$w_{\mathrm{MF}}(t) = s(t). \tag{2.6}$$

Now filtering the waveform with itself as a function of continuous delay, τ, as

$$\begin{aligned} y(\tau) &= \int_0^T w_{\mathrm{MF}}^*(t-\tau)s(t)dt \\ &= \int_0^T s^*(t-\tau)s(t)dt, \end{aligned} \tag{2.7}$$

yields a response with markedly better signal-to-noise ratio when compared to other filtering techniques. Note that $(\bullet)^*$ represents complex conjugation. In fact, the matched filter provides the best received SNR when the interference mixed with the returned signal is white Gaussian noise.

A standard tool that is used to gauge the performance of a waveform is the autocorrelation function (ACF). The ACF relates closely to the MF operation with only a single subtle difference: a normalization term. This autocorrelation is normalized by the energy possessed by the signal, or by normalizing by $||s(t)||_2^2$. The autocorrelation function is defined as

$$R_{\mathrm{a}}(\tau) = \frac{1}{||s(t)||_2^2} \int_{-T}^{T} s^*(t-\tau)s(t)dt \tag{2.8}$$

and describes the expected response for a single point scatterer in an environment lacking noise and interference. A waveform's ACF is typically used as an upper performance bound or "best-case scenario". From basic Fourier analysis, the Fourier transform of a signal's autocorrelation function is the power spectral density (PSD) function

$$S(f) = \mathbb{F}\{R_{\mathrm{a}}(\tau)\} = \frac{1}{||s(t)||_2^2} \int_{-\infty}^{\infty} R_{\mathrm{a}}(\tau)\exp(-j2\pi f\tau)\,dt \tag{2.9}$$

where $\mathbb{F}$ denotes the Fourier transform. The PSD is used to characterize a signal in the frequency domain by revealing features like spectral containment, spectral shape, bandwidth, etc. Depending

on processing constraints the PSD of a waveform can be tweaked or optimized to yield desired autocorrelation characteristics too. It is often useful to compare the similarity of one waveform as it relates to a separate waveform. Similar to the ACF, the cross-correlation function (CCF) compares waveforms $s_{\ell,1}(t)$ to $s_{\ell,2}(t)$, where the subscripts (ℓ, n) represent the ℓth waveform of the nth set of waveforms. For the sake of brevity the cross-correlation will be defined relative to two different waveforms, $s_1(t)$ and $s_2(t)$, as

$$R_{\mathrm{c}}(\tau) = \frac{1}{||s_1(t)||_2 \, ||s_2(t)||_2} \int_{-T}^{T} s_1^*(t-\tau) s_2(t) dt. \tag{2.10}$$

Notice that the power normalization term differs slightly from the ACF in (2.8) because the cross-correlation must be normalized relative to the total energy contained within both waveforms. The ACF and CCF will be used throughout this work to gauge the "goodness" of the separability of two waveforms. This can be seen in section 2.10.

2.4.2 Linear Frequency Modulation

The linear frequency modulated (LFM) radar waveform is one of the most popular and earliest forms of pulse compression. Though there are many different methods to enhance the characteristics of a LFM, only basic LFM parameters and processing techniques will be explained here. Delving into the multitude of different modulation types and processing techniques is beyond the scope of this document. Linear frequency modulation is created by sweeping the frequency of the transmit waveform linearly as a function of fast-time. A decoupling of the pulse duration and energy occurs by doing so, allowing for an extension in bandwidth while maintaining the same pulse duration. At baseband, the complex representation of a LFM is

$$s_{\mathrm{LFM}}(t) = A \exp\left(j\pi \, \frac{B}{T_{\mathrm{p}}} \, t^2 \right) \quad \text{for} \quad -\frac{T_{\mathrm{p}}}{2} \leq t \leq \frac{T_{\mathrm{p}}}{2} \tag{2.11}$$

where A is the amplitude of the waveform, B is the waveform bandwidth, and T_{p} is the pulse duration. Figure 2.3 depicts the time-domain response of an LFM waveform generated using (2.11)

and possessing a time-bandwidth product of 200. From this, it is easy to observe the time-changing frequency characteristics of the LFM waveform.

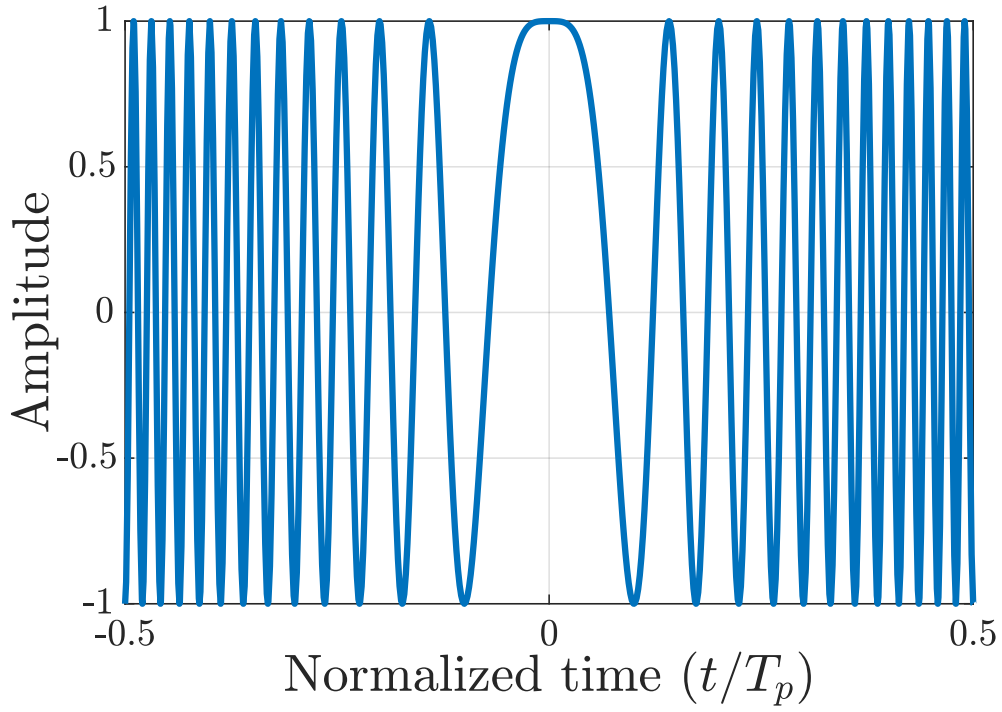

Figure 2.3: The time-domain response of a LFM pulse with a BT of 200.

Next consider the frequency spectrum of the LFM described above. This frequency response is determined by the inverse Fourier transform of the time-domain signal. Notice the relatively flat region in the center of the spectrum bounded by regions with steep spectral roll-off. This characteristic of the LFM makes it a desirable waveform for applications requiring strict spectral containment and wide functional bandwidths.

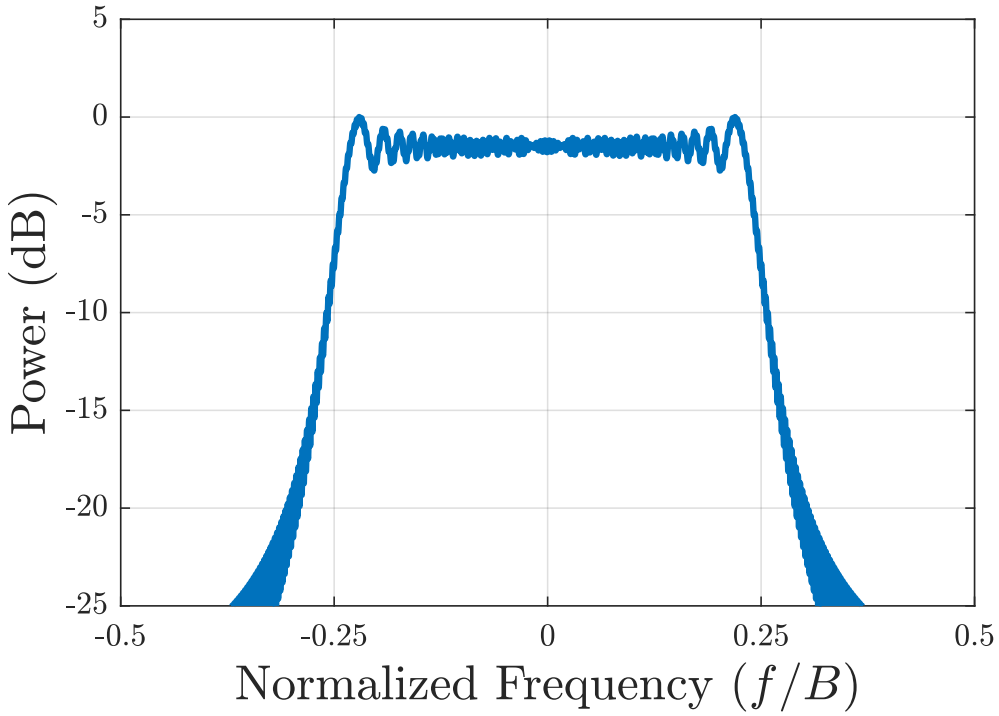

Figure 2.4: Normalized frequency spectrum of an LFM with a BT of 200.

The autocorrelation of an LFM waveform, calculated using (2.8), is shown in Figure 2.5. The autocorrelation function can be thought of as a type of compression by compressing a majority of the signal energy into the mainlobe structure. The remaining energy is distributed within the sidelobes shown in Figure 2.4. A LFM waveform possesses a peak sidelobe level (PSL) of -13 dB. While a -13 dB PSL may seem acceptable at face value, a functional radar system should possess a dynamic range in excess of $25-40$ dB to ensure that small target returns offset in time delay (or range) are not masked by the sidelobes. Complex transmit and receive processing can be used to reduce sidelobe levels.

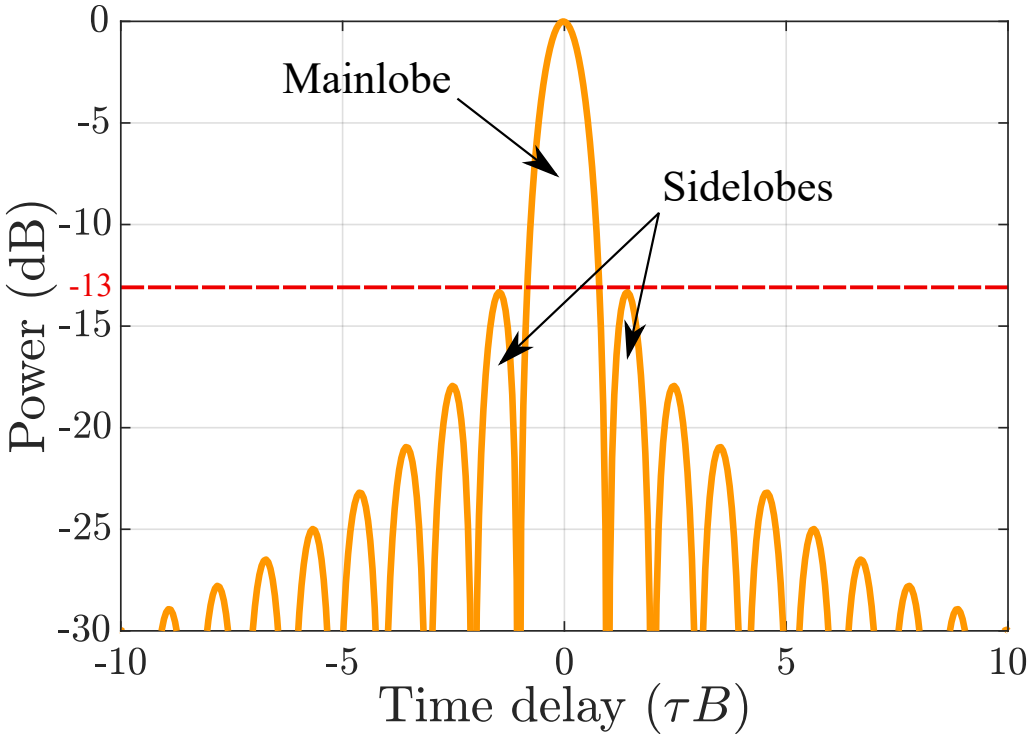

Figure 2.5: Normalized autocorrelation of an LFM with a BT of 200.

2.5 Bandwidth and Range Resolution

Up to this point the bandwidth of a radar waveform has not been clearly defined. Since radar systems transmit time-limited pulses, the complete bandwidth of a waveform would extend across all frequencies, though severe attenuation will be present when observing frequencies located far from f_c. To better describe the frequency range spanned by the signal of interest one must be able to describe the bandwidth as a discrete quantity. Though there are many different ways to describe the bandwidth of a waveform, the 3-dB bandwidth will be considered from this point forward unless otherwise noted. The 3-dB bandwidth is used ubiquitously in radar literature to describe the functional bandwidth of a system/emission and is defined as

$$B_{3\text{dB}} = f_{\text{HI}} - f_{\text{LO}} \tag{2.12}$$

where f_{HI} and f_{LO} correspond to the upper and lower half-power points of the waveform spectrum. Describing the bandwidth of a waveform with respect to the point in the spectrum where the power is halved provides a good method to gauge spectral containment based on emitted power.

To better describe the 3-dB bandwidth, consider Figure 2.6. Depicted is the frequency spectrum of a simple, unmodulated square pulse. The resulting frequency spectrum is a sinc-pattern with 3-dB bandwidth delimited by f_{LO} and f_{HI}. While this bandwidth may not seem very wide when observing the rest of the spectrum, it is important to note the steepness of the roll-off and associated attenuation of frequencies beyond the 3-dB points, meaning that an insignificant amount of power is observed at frequencies past the 3-dB upper/lower bounds. Note that the ordinate axis is expressed in terms of dB and that the spectrum is peak normalized to describe sidelobe levels. Using dB is the preferred method to view a multitude of radar characteristics because it represents a ratio of two numbers, in this case powers.

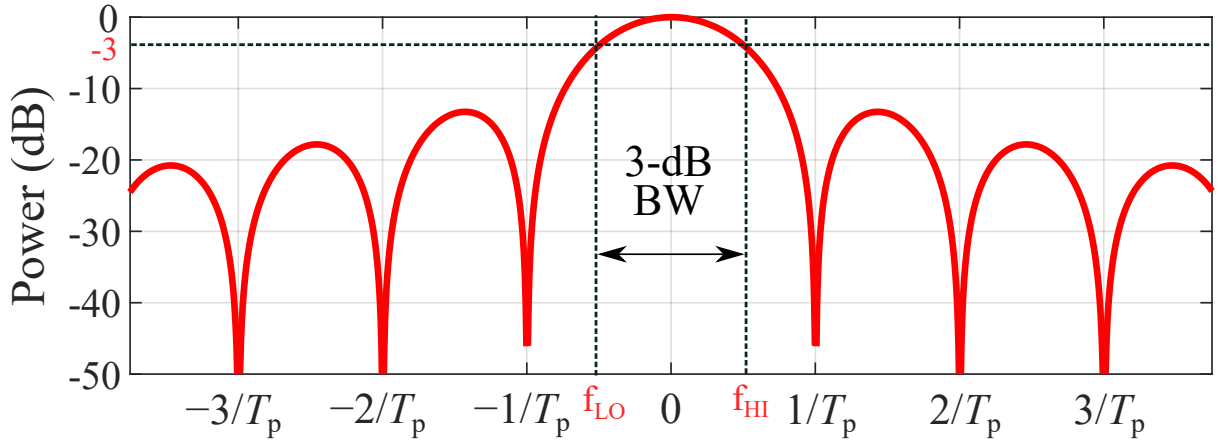

Figure 2.6: The 3-dB bandwidth of a simple rectangular pulse shown in amplitude and dB.

The range resolution, ρ_r, of a radar system determines how finely the range dimension of the received echoes can be sampled in the sense of differentiating closely spaced targets, not increasing the discrete sample rate of the system. A system with very course range resolution could mistake two or more targets for a single target if the scatterers are spaced too closely. The range resolution for radar system is derived from the Rayleigh resolution. The Rayleigh resolution is determined by the null-to-null width (or duration) of the autocorrelation mainlobe, defined as $\Delta\tau$ [50]. Refer back

to Figure 2.5 for an example of the autocorrelation of a LFM. Extending the definition of Rayleigh resolution to radar, the range resolution for an unmodulated radar pulse, assuming τ is two-way delay, is

$$\rho_{\mathrm{r}} = \frac{c\tau}{2} \tag{2.13}$$

where c is the speed of light. This autocorrelation mainlobe width can be approximated to the inverse of the 3 dB bandwidth as

$$\rho_{\mathrm{r}} \approx \frac{c}{2B_{3\mathrm{dB}}} \tag{2.14}$$

Note that it is important for the transmitted signal bandwidth to match the bandwidth of the receiver. A bandwidth mismatch can cause additional noise to leak into the receiver if the receiver bandwidth is larger than the transmitter bandwidth or the reduction in range resolution if the receiver bandwidth is lower. One of the many benefits of pulse compression is the increase in effective bandwidth, thus increasing the range resolution.

2.6 Polarimetric Radar

Up to this point frequency, phase, amplitude, and time have been discussed as characteristics that can be set and sensed by a radar system. Since a radar system transmits and receives electromagnetic waves, polarization of these emissions can be exploited to increase the amount of information collected. The typical radar system operates using an antenna that supports a single polarization mode for transmission and reception. While effective, this system will only collect target information with respect to that single mode, horizontal for example. To completely recover all information from the illuminated scatterer a system must utilize two orthogonal polarization modes [11]. A system must be capable of transmitting and receiving polarization diverse signals to construct the target scattering matrix and garner all information from the illuminated scene.

2.6.1 The Polarimetric Scattering Matrix

Referring back to section 2.2 and the definition of radar cross section, it is apparent that polarization is implied in its calculation by E_{TX} and E_{RX}. The arbitrarily polarized, time-varying, incident wave can be decomposed into the sum of two orthogonally polarized plane waves as

$$\vec{E}_{\mathrm{T}} = \vec{E}_{\mathrm{T1}} + \vec{E}_{\mathrm{T2}} \tag{2.15}$$

where $T1$ and $T2$ represent any pair of orthogonal polarization modes. Defining the received electric fields in terms of the associated transmit E-field components and reflection coefficients yields

$$\vec{E}_{\mathrm{R1}} = a_{11}E_{\mathrm{T1}} + a_{12}E_{\mathrm{T2}} \tag{2.16a}$$

$$\vec{E}_{\mathrm{R2}} = a_{21}E_{\mathrm{T1}} + a_{22}E_{\mathrm{T2}} \tag{2.16b}$$

where $\vec{E}_{\mathrm{R1}}$ and $\vec{E}_{\mathrm{R2}}$ represent a superposition of the corresponding components. The reflection coefficients, shown as a_{ij}, represent the amount of the incident wave that is reflected from the surface of the scatterer. The two number subscript designates the polarization of the received wave first and the polarization of the transmitted wave second. For example, a_{12} (shown in (2.16a)) represents the reflection coefficient with respect to receiving polarization 1 based on an incident wave of polarization 2. It is useful to describe the polarization state in terms of reflection coefficient because it provides an intuitive understanding into the interaction of the incident wave with the scattering surface and the resulting reflected power. Expanding (2.16a) and (2.16b) into matrix form yields

$$\begin{bmatrix} E_{\mathrm{R1}} \\ E_{\mathrm{R2}} \end{bmatrix} = \begin{bmatrix} a_{11} & a_{12} \\ a_{21} & a_{22} \end{bmatrix} \begin{bmatrix} E_{\mathrm{T1}} \\ E_{\mathrm{T2}} \end{bmatrix}, \tag{2.17}$$

where the matrix

$$[S] = \begin{bmatrix} a_{11} & a_{12} \\ a_{21} & a_{22} \end{bmatrix} \tag{2.18}$$

is defined as the polarization scattering matrix [62]. There are other methods to describe the scattering imposed on the incident E-field such as the Jones vector for describing polarized light [63–65], Stokes parameters for characterizing electromagnetic waves possessing partial polarizations by detectable power levels [66], the Wolf's coherency matrix [67], among others. The scattering matrix is desirable due to it describing co/cross-polarization states in terms of amplitude and phase, two fundamental radar parameters, by

$$[S] = \begin{bmatrix} |a_{11}|e^{j\phi_{11}} & |a_{12}|e^{j\phi_{12}} \\ |a_{21}|e^{j\phi_{21}} & |a_{22}|e^{j\phi_{22}} \end{bmatrix} \tag{2.19}$$

where $|a_{\mathrm{ij}}|$ and ϕ_{ij} represent the amplitude and phase of the a_{ij}th polarized response. The scattering matrix can thus be related back to the RCS of a coherent scatterer by solving (2.3) in terms of the scattering parameters for the received and incident E-fields using equations (2.15), (2.16a), (2.16b) and (2.17) to (2.19) as

$$[S] = \frac{1}{\sqrt{4\pi}\,R} \begin{bmatrix} \sqrt{\sigma_{11}}e^{j\phi_{11}} & \sqrt{\sigma_{12}}e^{j\phi_{12}} \\ \sqrt{\sigma_{21}}e^{j\phi_{21}} & \sqrt{\sigma_{22}}e^{j\phi_{22}} \end{bmatrix}. \tag{2.20}$$

Note that there is a power (or squared) relationship between target RCS and the scattering matrix. From (2.19) all of the scattering characteristics of a target can be recovered. It is imprecise to assume an ordinary linear transformation of the complex electric components of the propagating electromagnetic wave when reflecting off of a real object. This assumption presents problems because it implies that the scattering matrix of the object is the identity matrix, meaning the polarization state remains unchanged. All physical scatterers impose some form of change in the polarization state, in terms of amplitude and phase, of the reflected electromagnetic wave [68]. For example, a flat planar surface oriented normal to the direction of propagation would change a right-hand circularly polarized wave to left-hand, and vice-versa.

2.6.2 Polarimetric Radar Implementations and Processing

An addition of a second, orthogonal, polarization state to a radar system greatly increases the complexity of both the hardware and processing needed to handle transmission and interpret returns. This complexity is especially apparent in the antenna and RF sections of the hardware (waveform generation and data recording just require an additional channel to handle the additional polarization mode). A single antenna capable of transmitting and receiving on two orthogonal polarization modes is required unless two separately polarized antennas are used. A common antenna type is constructed from a pair of crossed dipoles aligned with the vertical and horizontal axes to permit a dual-pol mode. The antenna will also need two feed ports (one for each polarization) with good isolation to ensure the cleanest (with regard to polarization) possible signal is delivered and transmitted. This isolation is determined by the antenna cross-polarization rejection, also called polarization purity. Should the antenna cross-polarization rejection be insufficient then the orthogonality of the two signals will degrade [69]. Any degradation to the signals can lead to losses by raising the cross-correlation between the orthogonal channels. When operating in a simultaneous dual-pol mode it is desirable to create waveforms that possess low cross-correlation to facilitate the separation of co-pol and cross-pol scattering characteristics on receive [36].

The computational complexity of the receive signal processing required for a dual-pol radar system increases when compared to a traditional single channel system. However, since more information is gleaned from the illuminated scene the increase in complexity is negated by the increase in collected scattering characteristics. Receive processing for systems employing a polarization diverse emission is matched filtered similar to standard receive processing on a single polarization mode. The differences stem from the addition of co- and cross-pol terms. Consider the scattering matrix for a single point target located at some time-delay τ as

$$X(\tau) = \begin{bmatrix} x_{11}(\tau) & x_{12}(\tau) \\ x_{21}(\tau) & x_{22}(\tau) \end{bmatrix} \tag{2.21}$$

where x_{ij} are the scattering parameters for co- and cross-pol modes. The received signals can be expressed as

$$y_1(t) = x_{11}(\tau) * s_1(t) + x_{12}(\tau) * s_2(t) + n_1(t) \tag{2.22a}$$

$$y_2(t) = x_{21}(\tau) * s_1(t) + x_{22}(\tau) * s_2(t) + n_2(t) \tag{2.22b}$$

where $*$ denotes conjugation, $s_1(t)$ and $s_2(t)$ are the transmitted signals on orthogonal polarizations 1 and 2, and $n_1(t)$ and $n_2(t)$ are noise independently added to each channel. The goal is to estimate the scattering characteristics of $X(\tau)$ after being distorted by clutter, noise, and cross-correlation between orthogonal channels. It has been shown that a form of adaptive pulse compression (APC) that incorporates orthogonal polarizations called polarimetric adaptive pulse compression (PAPC) effectively reduces the co- and cross-polarized range sidelobes [70]. This adaptive processing technique also improves the estimation of receive scattering matrices of polarization diverse emissions. It has also been shown that APC can be applied to FM waveforms with good effect [71] as well as multistatic radar processing [72].

2.7 Doppler Processing

Along with utilizing radar systems for ranging, measuring the Doppler shift produced by a moving target is one of the oldest and most widely used applications. Modern radar signal processors often implement some form of Doppler processing on the received echoes from scatterers as well as clutter to improve the separability of the desired target from noise or interfering signals. One example would be the implementation of a ground moving target indicator (GMTI) system mounted on an airborne moving platform which attempts to tease apart two different Doppler returns: the largest return being the Doppler produced by the platform motion above the ground (ground moving relative to radar system) and the much smaller target Doppler characteristics [73]. Air traffic control (ATC) radar systems use range and Doppler data collected over time to estimate the ground-speed and heading of nearby aircraft [74, 75].

The received Doppler frequency shift, f_{D}, for a target located in direct line of sight (LOS) of

the radar system, for the monostatic case, is

$$f_{\mathrm{D}} = \frac{2v}{c} f = \frac{2v}{\lambda} \tag{2.23}$$

where v is the radial velocity component of the target and f is the transmitter center frequency. Note that (2.23) is defined for a target approaching the radar, hence the positive frequency shift. A target moving away from the radar system would in turn have a negative Doppler frequency. A target offset in elevation and moving towards the monostatic radar would have a Doppler shift of

$$f_{\mathrm{D}} = \frac{2v}{\lambda} \cos\left(\theta_{\mathrm{targ}}\right). \tag{2.24}$$

The angle θ_{targ} is defined as the angle between the radar line of sight (LOS) and the velocity vector of the target. This equation is valid for both approaching and receding targets due to the cosine function becoming negative once the target breaks the 90° (or $\pi/2$) plane. Note that a target moving orthogonally to the radar will have a Doppler shift of zero since the radial velocity component would be zero.

Similar to the relationship between PRF and unambiguous range, the maximum unambiguous Doppler is determined by the selected PRF too. The proper PRF is typically determined on an application specific basis using

$$PRF_{\mathrm{min}} = 2 f_{\mathrm{D,max}} \tag{2.25}$$

to determine the theoretical lower bound for the PRF. From (2.25) the bounds of the Doppler frequency spectrum can be found as $\pm PRF/2$. Thus the Doppler spectrum spans a frequency range the size of the selected PRF. A moving target possessing a Doppler shift outside of this bound will repeat at frequencies $f_{\mathrm{D}} - nPRF$ for some integer n [50]. This presents problems if the proper PRF is not selected. For example, if an object is moving at a velocity corresponding to a Doppler shift of $0.7PRF$ and is illuminated by a radar system, the measured Doppler shift will alias every PRF Hz with the nearest aliased signals residing at $-0.3PRF$ and $1.7PRF$. Since the object

possesses a Doppler shift greater than $0.5PRF$ the measured velocity will be calculated incorrectly and even in the opposite direction. Thus it is wise to select a PRF based on the maximum expected velocity one might expect to see for the chosen application.

The Doppler resolution, defined as

$$\Delta f_{\mathrm{D}} = \frac{f_{\mathrm{D,max}}}{\#\text{ of pulses}} = \frac{PRF}{2}\,\frac{PRI}{CPI}, \tag{2.26}$$

of a radar system determines how finely the system can sample Doppler frequency shifts (or velocities). This resolution is related directly to the number of pulses that are placed on target, as can be seen in (2.26). Doppler resolution can be converted to velocity resolution by multiplying (2.26) by λ, giving the resultant resolution in meters per second (which can then be converted to the final desired unit).

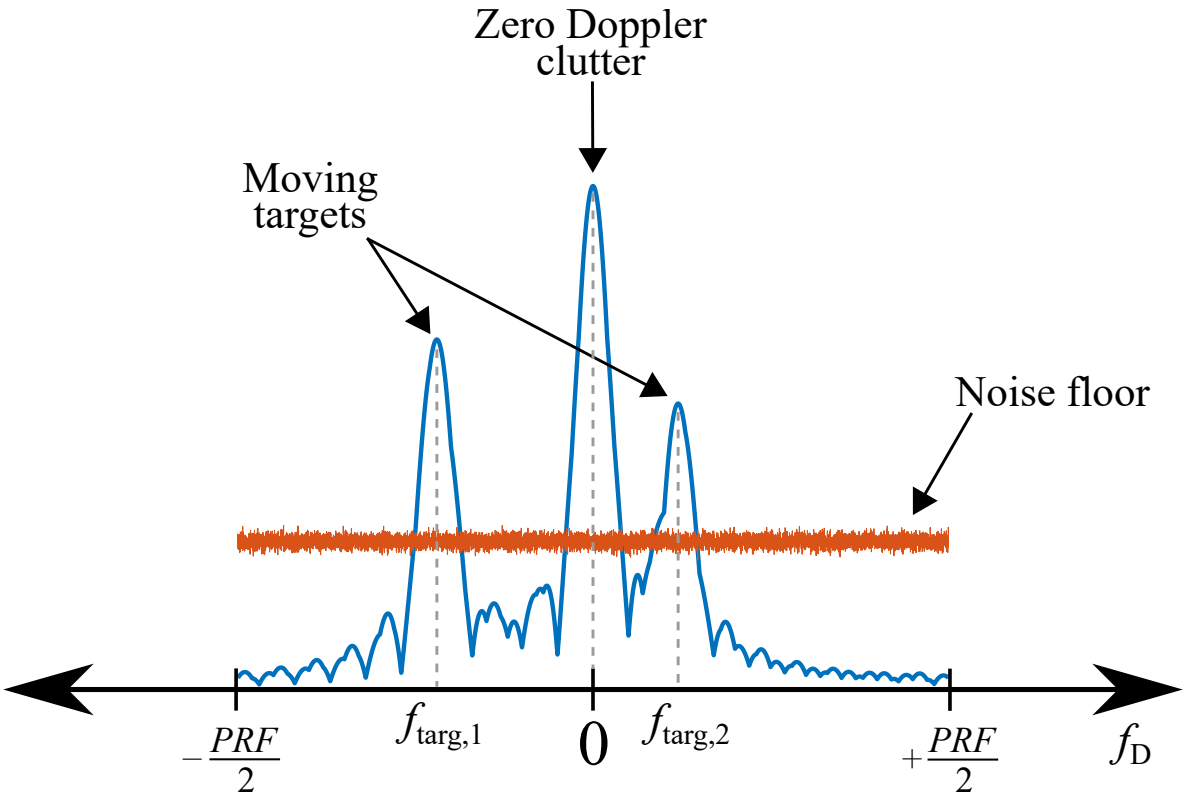

Figure 2.7: Simple Doppler spectrum for a stationary monostatic radar system.

The Doppler frequency spectrum is created for each range bin by taking the Fourier Transform

in the slow-time dimension. To aid in the explanation of the Doppler frequency spectrum, consider Figure 2.7. This figure offers a simplistic look at a rudimentary Doppler frequency spectrum for a single range sample. Located at digital baseband is the the response with no frequency shift (zero Doppler) for an arbitrary scene and will typically be much higher than the target returns. The main contributor to the strength of the peak of the zero Doppler mainlobe is the clutter contained within the illuminated scene. Examples could be trees, buildings, etc. Though not explicitly described in Figure 2.7, the width of the mainlobe is determined by the inverse of the coherent processing interval (*CPI*), as $1/CPI$ or the number of pulses divided by the *PRF*. As described above, the width of the unaliased Doppler spectrum is determined by the system's *PRF*. Similar to Nyquist zones in a sampled signal's frequency spectrum repeating as a function of the sampling frequency, the Doppler spectrum repeats every *PRF* Hz, extending from $[-PRF/2, PRF/2]$. This bound is created from the repeating nature of the sampled receive spectra outside of that area. For this reason, the *PRF* must be chosen on an application specific basis to avoid processing ambiguous Doppler returns. For a target to be detected the magnitude of the response must be higher than the noise floor in the Doppler spectrum (this is not always true, coherent integration over many pulses can tease out small returns through the decoherence of noise). Here there are two targets, one located on either side of the zero Doppler clutter. The Doppler shift associated with each target is the difference between $f = 0$ and f_{targ}, with $f_{\text{targ,1}}$ possessing a negative Doppler shift and $f_{\text{targ,2}}$ possessing a positive Doppler shift.

From the *PRF* constraints described in (2.25) and the definition of *PRF* from (2.1) the following relationship can be derived

$$v_{\max} R_{\max} = \frac{c\lambda}{4} = \frac{c^2}{4f_c}, \tag{2.27}$$

describing the trade-space between maximum unambiguous range and unambiguous Doppler frequency. Here, $v_{\max}$ is the maximum unambiguous radial velocity and relates to the largest Doppler frequency shift that does not alias within the Doppler frequency spectrum. Since maximum detectable Doppler frequency and maximum unambiguous range are coupled, trade-offs between the two must be made depending on the purpose of the system being designed. The only way to in-

crease both $v_{\max}$ and $R_{\max}$ is by lowering the transmit center frequency f_c. However, doing this is often not applicable.

When using an LFM (discussed in section 2.4.2) a phenomenon called range-Doppler coupling occurs. This coupling transpires due to the time-frequency relationship intrinsic to the LFM waveform. A LFM can be described as a sinusoid whose frequency linearly increases (or decreases) as a function of time, called the chirp rate. A frequency shift imposed on the received signal caused by a moving scatterer will equate a time-shift when processing the received signal, assuming that a time-shifted and amplitude-scaled version of the transmit waveform was received. The size of this shift is $(f_D/B)T_p$. The Doppler tolerance, or how well a received waveform performs with an uncompensated Doppler frequency shift, is determined by the range-Doppler ambiguity function [50, 76]. The size of the relative frequency shift must be large to elicit detrimental effects in the receive processing chain.

The practical implementation of Doppler processing is quite simple. For a single phase center monostatic radar, Doppler processing is implemented by chopping up the receive *CPI* into individual *PRI*s and taking the discrete time Fourier transform (DTFT) across the pulses (or in the slow-time dimension). Doing so determines the frequency shift relative to the other coherent pulses. To implement this the adjacent pulses must be coherent, otherwise frequency shifts relative to target-radar motion cannot be isolated.

When processing experimental data, the receive echoes are first range compressed using the matched filter as described in section 2.4. This process ensures (at the most basic level, without "fancy" receive processing) that the received data will bear the best SNR. The process of receive sampling introduces ambiguities within the filters in the radar receiver leading to ringing and expansion in the Doppler frequency dimension [50]. This ringing causes Doppler sidelobes to appear. Like sidelobes in other dimensions, Doppler sidelobes can mask weaker returns. Windowing in the frequency dimension prior to Doppler compression is required to suppress these sidelobes and remove (or reduce) Doppler ambiguities. While there are a plethora of window functions being used in systems today, common ones include the Hamming, Hanning, Tukey, and Blackman-Harris. A

good resource for in-depth discussion and analysis of many common window types can be found in [77]. Most window functions conform to a shape that resembles a raised cosine, with each possessing a different α value. The definition of a raised cosine spectrum can be found in most communications textbooks like [78]. Each of the window functions possess the same basic shape with the maximum value at the center of the spectrum and a smooth taper at the edges, examples can be seen in Figure 2.8. However, note that the tails, or edges, of each window function do not necessarily always go to zero like the raised cosine.

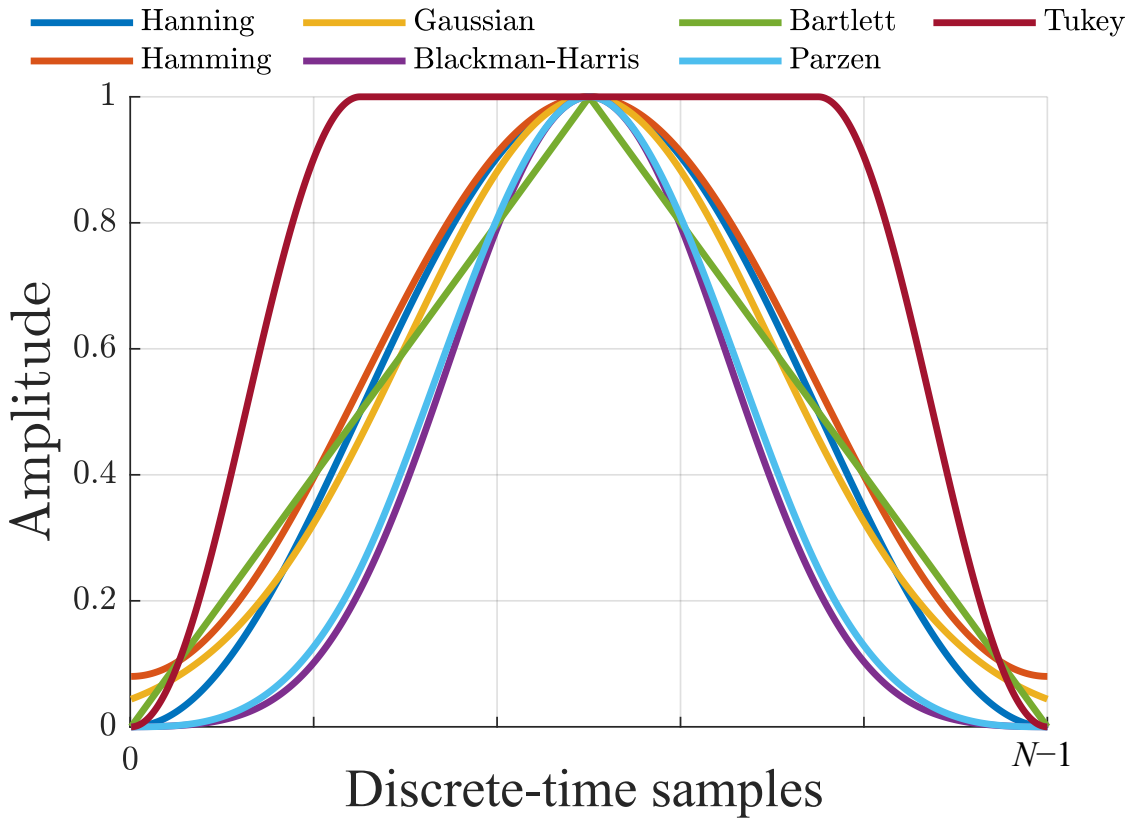

Figure 2.8: Various window functions in the discrete-time sample domain.

2.7.1 Clutter Cancellation

When processing radar returns recovering Doppler information from target signatures is used to help determine speed relative to the radar, trajectories, and discriminate between multiple possible targets. As described above, this information is recovered by taking the discrete Fourier transform in the slow-time domain, compressing the returned energy of multiple pulses into a single

range bin. This process separates returns with Doppler from returns without, called zero-Doppler clutter. Depending on the application the zero-Doppler clutter will possess returns significantly stronger than the echoes from moving targets. This is particularly apparent in applications like space-time adaptive processing (STAP) which is used as a method for ground moving-target indication (GMTI), and other ground-facing radar systems [79]. Refer back to Figure 2.7 for a visual representation of the large returns from clutter and smaller returns from two targets containing Doppler. The sidelobes from the clutter returns can severely impact the functional dynamic range of the receiver and mask targets with low RCS and small Doppler offsets. To combat the detriment to performance caused by large clutter returns radar receivers often implement some form of zero-Doppler notching to remove the clutter ridge and sidelobes from the range-Doppler processed returns. This notching can be implemented using several different methods and is completed prior to Doppler compression.

The width of the frequencies being notched can either be static but some applications require the Doppler notching filter to be adaptable due to changing environmental conditions and discrete clutter returns, among various others. Theoretically the clutter contained within the zero Doppler mainlobe is one frequency sample but due to internal clutter motion this clutter region is widened. Since the response from the mainlobe clutter is much larger than the target responses a washing out or covering of the received target echoes can occur. To prevent this from occurring a method to cancel or "throw away" the zero Doppler return information is needed. The approach used in this work is called a zero Doppler projection and projects the energy contained within the clutter ridge data out of the Doppler spectrum. The first step in creation of this projection is determining the width of the desired frequencies to be notched as

$$\mathbf{A}_{\text{zero-Dopp}} = \exp\left(j2\pi\ell\overline{f}\right), \tag{2.28}$$

where ℓ is the ℓth pulse in the *CPI* and $\overline{f}$ is the width of digital frequencies being notched. Next a singular value decomposition (SVD) is performed as

$$\mathbf{U}\Delta\mathbf{V}^{\mathrm{H}} = \mathbf{A}_{\text{zero-Dopp}} \tag{2.29}$$

where the columns of $\mathbf{U}$ and $\mathbf{V}$ contain the left- and right-singular vectors and Δ is a diagonal matrix containing the singular values of the matrix $\mathbf{A}$. Next the number of principal values is determined by plotting the diagonal values of matrix Δ and observing the number of values that are much larger than zero. The number of significant singular values, P_{s}, determines the rank of the filter. Next the first P_{s} columns of the left-singular vector matrix $\mathbf{U}$ are stored as $\mathbf{U}_{\mathrm{s}}$. The zero-Doppler projection is then constructed by

$$\mathbf{W}_{\text{notch}} = \mathbf{I} - \mathbf{U}_{\mathrm{s}} \left(\mathbf{U}_{\mathrm{s}}^{\mathrm{H}} \mathbf{U}_{\mathrm{s}}\right)^{-1} \mathbf{U}_{\mathrm{s}}^{\mathrm{H}} \tag{2.30}$$

where $\mathbf{I}$ is the identity matrix and $(\bullet)^{-1}$ is the matrix inverse operation. The matrix $\mathbf{W}_{\text{notch}}$ is used to project the energy contained within the zero-Doppler clutter out of the received data. Note that this particular projection implements a static width but could be extrapolated to an adaptive implementation by inserting some form of feedback into the algorithm. The frequency width being determined in (2.28) by selecting a $\overline{f}$ that spans the desired width. This notching technique is used for all Doppler processed returns, whether simulated or experimental, within this work.

As an example consider a short simulation demonstrating the performance gained when using this zero-Doppler projection. Consider a ground-based monostatic radar illuminating a static scene containing random stationary clutter and five targets possessing random range and Doppler information. For this simulation a LFM up-chirp will be transmitted for $L = 100$ pulses on a single polarization, each possessing a BT of 200. White Gaussian noise with power proportional to the BT of the waveforms will be added to the signals on receive for added realism. First consider the range-Doppler map created when no notching is conducted in Figure 2.9(a). Notice the large strip of returns populating every range bin at zero-Doppler and with very high sidelobe levels swamping the entirety of the Doppler dimension. These are the returns from zero-Doppler clutter. Next consider the effects of the zero-Doppler projection described above. Notice the removal of the energy from the zero-Doppler clutter in Figure 2.9(b). After the clutter ridge has been projected

out of the data a target located close to zero-Doppler around range bin 120 is uncovered and more easily detected. The zero-Doppler clutter shown in this scene is simulated and widened using a small and random phase dithering that changes with each pulse. This simulates internal clutter motion. The clutter observed during experimental measurements shows a much greater variance in received power and will be wider due to real internal clutter motion and slight phase incoherence within test equipment.

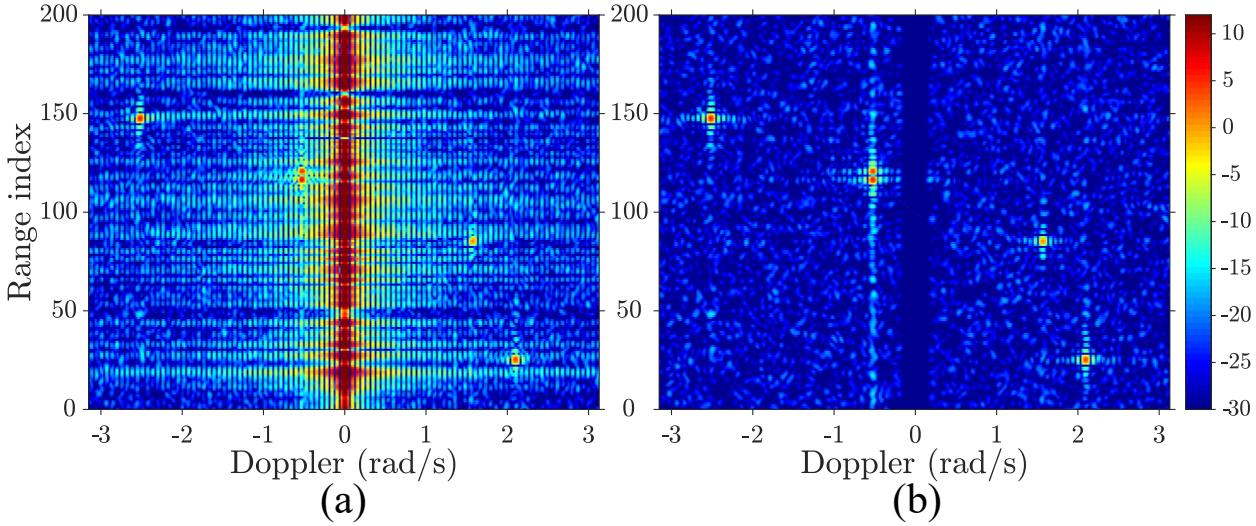

Figure 2.9: Range-Doppler plots of simulated target data a) without zero-Doppler notching and b) with zero-Doppler notching.

2.8 Array Processing

The concept of an arrayed antenna has been studied since the early 1900s but was did not see wide usage until around World War II. The first countries to widely use phased arrays were the United States, Britain, and Germany for applications including aerial search, fire control, height finding, among others [58]. Phased arrays are desirable in that the emission can be steered without physical movement of the antennas. This is completed by applying a phase shift to each element corresponding to the desired look direction. The arrays used in WWII were large antennas that were constructed in fixed positions and steered using mechanical phase shifters. Today, fully digital arrays are most often steered electronically via digital phase shifters, providing the ability

to steer along two orthogonal axes. These arrays are called electronically scanned arrays (ESA) or more recently digital array radar (DAR) and provide many benefits over antennas possessing only a single phase center (like horn antennas). These many benefits include the ability to produce multiple beams from a single array for a multifunction mode [18], simultaneous emission of radar and communications from the same aperture [80, 81], and many other functions unique to digital arrays [82, 83].

A radar system that utilizes arbitrary waveform generation (AWG) capabilities to transmit independent waveforms on an element-wise basis falls under the moniker of MIMO (or multiple input multiple output). This unique type of system provides unmatched flexibility in terms of multifunction array capabilities on transmit and receive. As will be shown in section 4, the use of a particular form of MIMO will facilitate a spatially-diverse emission providing flexible emission structures and enhanced spatial resolution [1, 40, 42, 43]. Note that traditional research on MIMO waveforms focuses on the design of the aggregate far-field emission using orthogonal waveforms or similar but that no orthogonal waveform design is present within this work.

Though there are many different array configurations, the uniform linear array (ULA) and uniform planar array (UPA) provide the most straight-forward understanding of array characteristics. The ULA is comprised of equally spaced identical array elements placed in a straight line. An example of this geometry is shown in Figure 2.10. For this introductory section on array processing all phenomenology will be described relative to the ULA for the sake of brevity and ease of comprehension. Extrapolation to planar arrays is discussed in detail in section 4 to support related simulations. The individual elements are also assumed to be ideal isotropic radiators for sake of simplicity, although in reality perfect isotropic radiators do not exist. Consider the ULA geometry depicted in Figure 2.10.

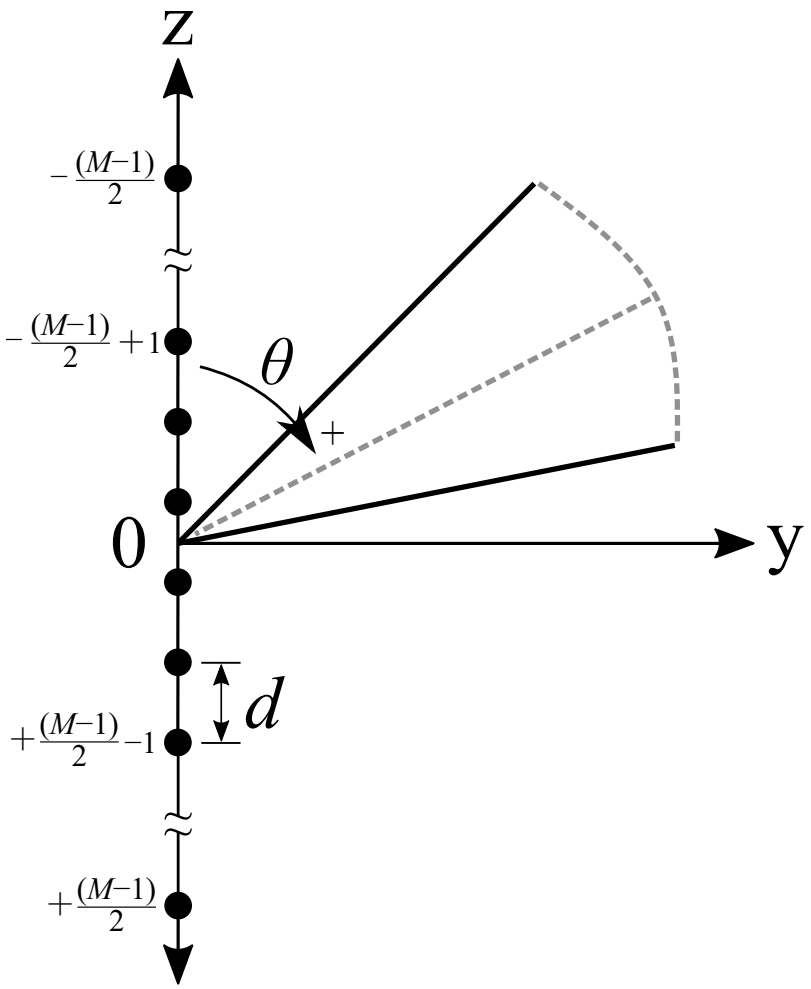

Figure 2.10: Uniform linear array geometry with M equally spaced elements located on the x-axis.

The M array elements depicted in Figure 2.10 are indexed as

$$m \in \left\{ -\frac{(M-1)}{2}, -\frac{(M-1)}{2}+1, \ldots, +\frac{(M-1)}{2} \right\}, \tag{2.31}$$

and reside on the z-axis, which ensures the array is centered at the origin. Note that orienting the elements along the z-axis provides convenient simplifications when using the spherical coordinate system. Array boresight (or broadside) in this configuration is located along the y-axis with the positive x-axis protruding out of the document. Because the elements are assumed to be ideal isotropic radiators aligned with the z-axis, the spherical coordinate ϕ has been omitted since the radiation patterns for this array does not vary with ϕ. Spherical variable θ is used to parameterize

beam steering and is defined relative to the positive z-axis with range $[0^\circ, 180^\circ]$.

There are two important assumptions that are typically made when simulating arrays that greatly simplify processing. The first is the *narrowband array* assumption which presumes that the propagation time, Δt, between the end-most array elements is negligible when compared to the inverse of the signal bandwidth [84]. This relationship is described as

$$\Delta t_{\max} << \frac{1}{B_{\text{signal}}} \rightarrow \Delta t_{\max} B_{\text{signal}} << 1 \tag{2.32}$$

where $\Delta t_{\max}$ is the maximum delay between the first and last element in the above ULA geometry. The total propagation delay for M array elements is thus

$$\Delta t_{\max} = \frac{(M-1)d}{c} \tag{2.33}$$

where d is the inter-element spacing of the ULA and c is the propagation speed (assumed to be the speed of light). Next, the array is assumed to be sufficiently large under the *large array* approximation. This assumption addresses edge distortion effects exhibited by small arrays.

2.8.1 Beam Steering and Receive Processing

For an infinitely long ULA, each of the M_∞ elements will exhibit identical responses with respect to each other, leading to an identical transmit pattern for each element [85]. Under the *large array* assumption the emission pattern is measured for a single element and is used to approximate the total pattern for the array. Typically the most central or next-to-center element pattern is used in this approximation. An array of finite length will exhibit element patterns that vary as a function of m, with the elements near the edge displaying the most distortion. An array of sufficiently large size produces an aggregate emission pattern that "drowns out" the distortions imposed by edge effects [86, 87]. The typically accepted minimum array size should have total length of 5λ with λ stemming from the center frequency of the emission [88].

For an array to steer to a desired direction in space a phase offset between the elements cor-

responding to that center look direction must be applied. This offset is enforced upon the array emission via the array manifold vector (or steering vector) as

$$v_{\mathrm{k}}(k_{\mathrm{z}}) = e^{jmk_z d} \tag{2.34}$$

where m is the indexed array elements from (2.31) and with wavenumber

$$k_{\mathrm{z}} = \frac{2\pi}{\lambda}\sin(\theta) \tag{2.35}$$

under the narrowband array assumption. The application of the steering vector to the baseband waveform $s_m(t)$ yields the array factor

$$g(t,\theta) = \frac{1}{M}\sum_m s_m(t) e^{jm\frac{2\pi}{\lambda}d\sin(\theta)} \tag{2.36}$$

which describes directivity of the array pattern under the narrowband assumption. Simplification of the array factor is often made for the sake of brevity and ease of comprehension. By substituting

$$\phi(f_c,\theta) = \frac{2\pi}{\lambda}d\sin(\theta) \tag{2.37}$$

into equation 2.36 the array factor equation can be condensed to

$$g(t,\theta) = \frac{1}{M}\sum_m s_m(t) e^{jm\phi(f_c,\theta)} \tag{2.38}$$

where ϕ is referred to as the electrical angle. Transforming from spatial angle θ to electrical angle ϕ describes the array pattern as a function of the successive phase differences between the M antenna elements. The space spanned by $\phi(f_c,\theta)$ is defined from $[-\pi,\pi]$ and is used throughout this work interchangeably with θ when describing emission patterns.

Transforming the array factor to the frequency domain yields

$$G(f,\theta) = \frac{1}{M}\sum_{m} S_m(f) e^{jm\phi(f_c,\theta)} \tag{2.39}$$

which represents the mth complex-baseband waveform in the frequency domain. Since this work employs fast-time beam steering, dubbed spatial modulation, the emitted beam pattern of the array changes as a function of fast-time [1]. Traditional definitions of array patterns assume the center-look direction for the array remains constant throughout the pulse (or CW segment) and will not provide insight into how the spatially modulated mainbeam is moving throughout the pulse. Because of this, a method to investigate the beam pattern at each fast-time interval is required and was derived and used in [1, 40–42]. Under the large array approximation and narrowband array assumption the complex-baseband time-varying beam pattern (TVBP) can be defined as

$$\widetilde{g}(t,\theta,\phi) = \frac{1}{M} F_a(\theta,\phi)\sum_{m} s_m(t) e^{jm\phi(f_c,\theta)} \tag{2.40}$$

and

$$\widetilde{G}(f,\theta,\phi) = \frac{1}{M} F_a(\theta,\phi)\sum_{m} S_m(f) e^{jm\phi(f_c,\theta)} \tag{2.41}$$

where $F_a(\theta,\phi)$ is the approximate element pattern for the center-most element. The aggregate response of the spatially modulated emission from the array throughout the pulse length, T_p, is called the aggregate beam pattern (ABP) and is the integration of the TVBP over the interval T_p. The ABP is defined as

$$B_\mathrm{ABP}(\theta) = \frac{1}{T_\mathrm{p}}\int_0^{T_\mathrm{p}} |\widetilde{g}(t,\theta)|^2 dt. \tag{2.42}$$

It is sometimes useful to change the angle-dependent variable $\sin(\theta)$ to its own variable, converting to $\bar{\mathrm{u}}$-space [84]. This new variable is defined as

$$\bar{\mathrm{u}}(\theta) = sin(\theta). \tag{2.43}$$

From this definition the electrical angle definition from equation 2.37 can be rewritten as

$$\phi(f_c, \theta) = \frac{2\pi}{\lambda} d \, \bar{\mathrm{u}}(\theta) \tag{2.44}$$

which is defined over $[-1, 1]$, the range of the $\sin(\bullet)$ function. This change of variables provides a more succinct definition of electrical angle and a normalization of the spatial beampattern of an array. These three coordinate spaces: spatial angle, electrical angle, and $\bar{\mathrm{u}}$-space are used throughout this work to describe various characteristics and results when simulating array emissions.

A plane wave impinging upon a ULA will exhibit the same delay between elements as a transmission from the same ULA pointed in the direction of arrival of the receive signal. From this characteristic receive beamforming can be defined. Note that receive beamforming is very similar to transmit beamforming. Assuming that the individual elements of the array have independent receive chains (including digitizers and filters) the stored signals must be phase-compensated during processing to compensate for the inter-element time delay. When operating in receive mode an array can steer the receive gain pattern by exploiting the same array characteristics that provide steering of the transmit beam. This can be beneficial during passive operating modes and for ensuring the signal/target of interest remains within the mainlobe of the receive gain pattern. Similar to how the center-look direction for an array is defined relative to angle θ, the direction of maximum gain on receive will be defined with respect to θ_{Rx}. The received signal is defined as

$$y(t, \theta_{\mathrm{Rx}}) = \frac{1}{M} \sum_m y_m(t) e^{-jm\phi(f_c, \theta_{\mathrm{Rx}})} \tag{2.45}$$

and shares the same form as the baseband emission pattern. The receive signal is thus the sum of the M signals collected by the individual elements, normalized by the number of elements/signals, and phase-compensated for the direction of arrival. For the purpose of match filtering in a MIMO mode the individual receive signals collected by mth element will be match filtered with the corresponding transmit signal sent by the mth element. However, this greatly increases the amount of processing required.

The aggregate beam pattern for a $M = 20$ element ULA in θ-, ϕ-, and $\bar{u}$-space is shown in Figure 2.11. The mainlobe for this emission is located at array broadside, meaning no beam steering is occurring. Notice the distortion in the sidelobes of the beam pattern in Figure 2.11(a) when compared to Figures 2.11(b) and (c) when moving away from broadside. This distortion occurs due to the nonlinear nature of the $\sin(\bullet)$ function. The sidelobes depicted in electrical angle (ϕ and $\bar{u}$) exhibit uniform spacing compared to the sidelobes plotted in spatial angle which increase in width when moving away form boresight.

An array of antenna elements that are offset in space can be thought of as a spatial filter that couples the space and time dimensions. An array exploits this relationship by spatially sampling signals, assumed to be plane waves in the far-field. The spatial dimension can be more finely or coarsely sampled by changing the distance between the elements. Increasing the number of elements broadens the effective aperture in the corresponding dimension. This subsequently improves directivity and narrows the width of the mainbeam of the antenna pattern. A common inter-element spacing, given by

$$d = \frac{\lambda}{2}, \tag{2.46}$$

is a function of the wavelength, λ, of the radar system's transmit center frequency. Maintaining $\lambda/2$ spacing ensures that the beam pattern does not contain grating lobes within the visible region for all angles of θ. The minimum size of an array using this element spacing is 10 under the *large array* assumption [84]. Other element spacings are possible but careful consideration must be exercised with respect to maximum steering angles and the appearance of grating lobes in the beam pattern. For example, if an array with the beam pattern shown in Figure 2.12 were to steering to $\pm 90^{\circ}$ (or $\pm pi$ in electrical angle) the nearest grating lobes would not appear within the visible region. Should the inter-element spacing be increased to λ for example, then the distance between the grating lobes would be halved and result in grating lobes appearing in the antenna pattern. For the sake of simplicity, all simulations and discussions in regard to arrays will assume $\lambda/2$ spacing between elements.

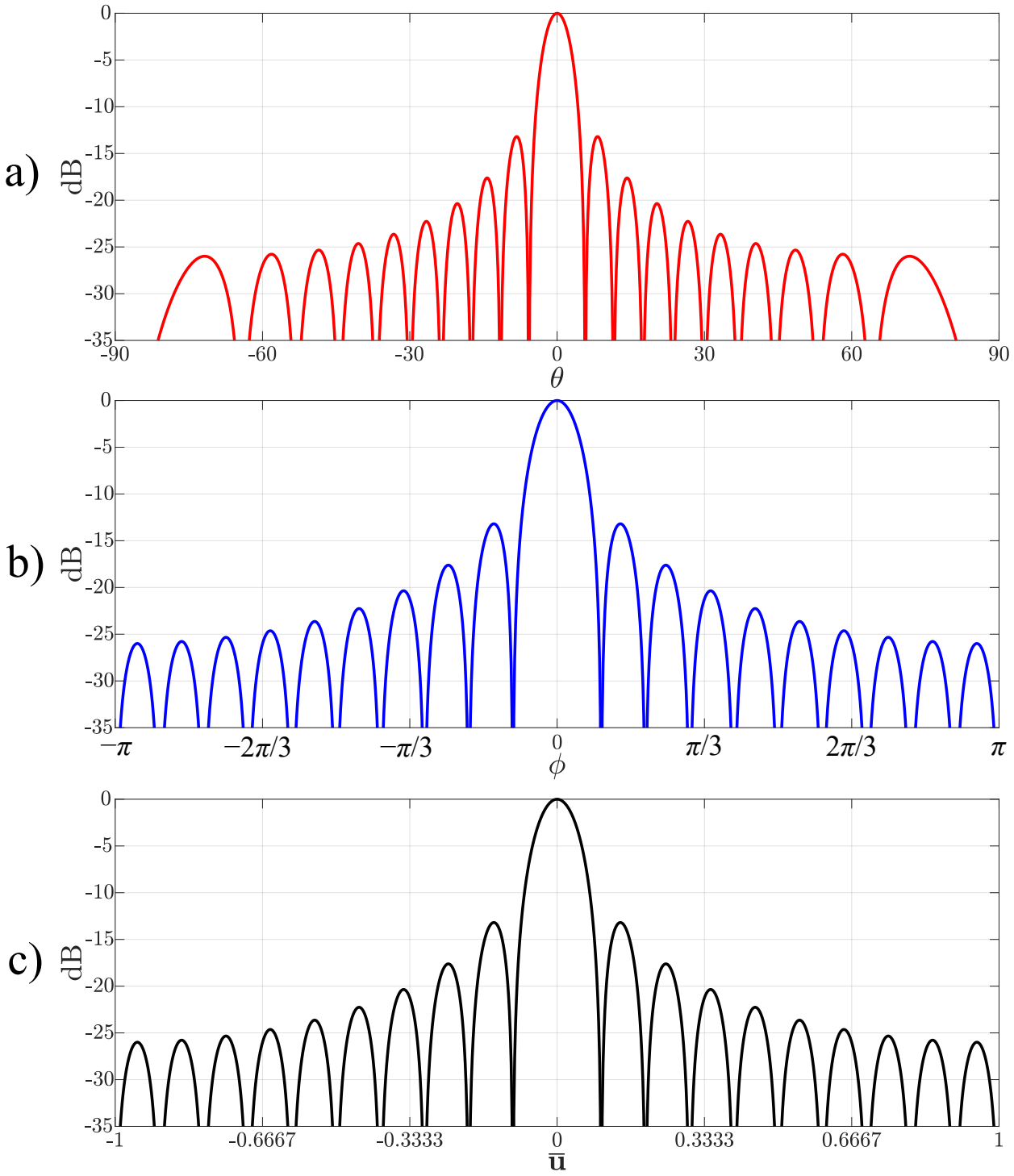

Figure 2.11: Far field aggregate beam patterns for a $M = 20$ ULA with $d = \lambda/2$ in a) θ-space (spatial angles), b) ϕ-space (electrical angles), and c) $\bar{\mathbf{u}}$-space (normalized electrical angles).

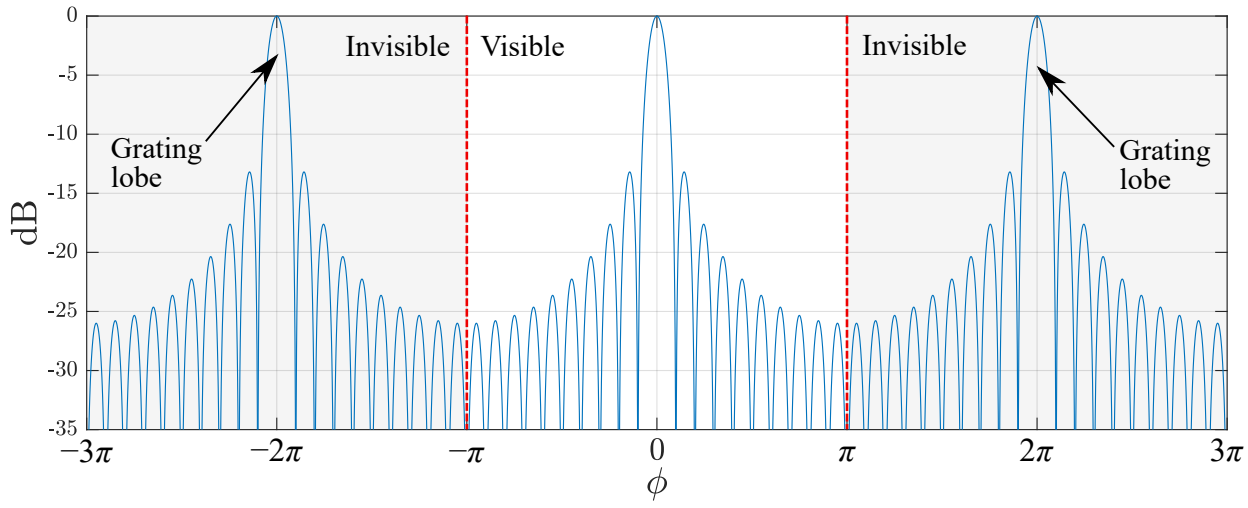

Figure 2.12: Beam pattern in ϕ-space for a $M = 20$ ULA with inter-element spacing of $\lambda/2$ extended beyond visible region.

Increasing the number of elements in an array dimension, while maintaining the same spacing, effectively increases the resolution in that dimension without any different forms of processing. Doing so also narrows the null-to-null beamwidth of the mainbeam as proportional to the number of the array elements for each dimension as

$$\begin{aligned} BW_{\text{NN}} &= \frac{2\lambda}{dM} \quad (u\text{-space}) \\ &= \frac{4\pi}{M} \quad (\phi\text{-space}) \\ &= \frac{4\pi}{dM} \quad (k\text{-space}) \end{aligned} \tag{2.47}$$

in three popular coordinate spaces [84]. The directivity of the array pattern will also increase as the beamwidth decreases. Note that the beamwidths from (2.47) are for arbitrary element spacing and simplify if $\lambda/2$ spacing is maintained throughout. However arbitrarily increasing the number of elements without increasing the size of the array (meaning increased element density) or increasing transmit frequency f_c will widen the main beam and decrease directivity.

For certain applications it is sometimes beneficial to broaden the beamwidth wider than what can be provided by the constraints of the system using typical array processing. For example, a widened beamwidth will spread the emission out over a larger area during each *CPI*, allowing

the system to scan a sector of the sky or ground using less *CPI*s, thus decreasing the amount of time required. Then, once a target or interesting portion of the scanned sector is located the broadened beam can be switched back to the normal beamwidth to provide greater directivity and place more power on target. This technique is referred to as spoiling the main beam of the emission pattern [89]. The beam spoiling employed within this work is completed by injecting small random phase-dithers across the standard beam pattern. This will broaden the mainlobe as a function of the mean size of the random phase jumps that are inserted into the standard beamforming equation.

2.9 Polyphase-Coded Frequency Modulated (PCFM) Waveforms

The need for the polyphase-coded frequency modulated (PCFM) waveform generation structure arose from a sudden and large interest in waveform diversity. While not a new concept, the use of phase codes in radar waveforms has been around for many years, Barker codes for example [90]. Practically speaking, many phase codes cannot be implemented on hardware due to poor spectral containment (extended sidelobes) and nonlinear transmitter effects [53]. One of the main drawbacks limiting the implementation of phase codes to radar transmitters is the nonlinearity and subsequent bandwidth growth that occurs between adjacent code chips [10]. Stemming from continuous phase modulation (CPM) in the communication world [91–93], PCFM waveforms convert an arbitrary phase code into a non-linear FM waveform in a piece-wise manner [94–96].

PCFM addresses the problems listed above by enforcing a constant time envelope and ensuring that the resulting waveform is continuous, and thus differentiable. These characteristics make PCFM waveforms highly desirable for applications requiring the use of high power transmitters, like radar for instance. For the purpose of a radar waveform implementation, the information carrying requirements of CPM can be eliminated. This greatly simplifies the generation of the waveform as well. A polyphase radar code is constructed from a sequence of N impulses offset in time by T_{p}. The PCFM algorithm is first initialized with a length $N+1$ arbitrary phase code designated $[\theta_1\ \theta_2\ \ldots\ \theta_{N+1}]^{\mathrm{T}}$. This creates an impulse train of length NT_{p} in time. The weighting applied to the nth impulse is represented by α_n and is the phase difference between adjacent chips

within the code sequence. The weights are determined by

$$\alpha_n = \Psi(\widetilde{\alpha}_n) = \begin{cases} \widetilde{\alpha}_n, & \text{if } |\widetilde{\alpha}_n| \leq \pi \\ \widetilde{\alpha}_n - 2\pi \operatorname{sgn}(\widetilde{\alpha}_n), & \text{if} |\widetilde{\alpha}_n| \geq \pi \end{cases} \tag{2.48}$$

where

$$\widetilde{\alpha}_n = \theta_n - \theta_{\text{n-1}} \quad \text{for} \quad n = 1, \ldots, N. \tag{2.49}$$

In (2.48) $\operatorname{sgn}(\bullet)$ is the signum operator and θ_n is the phase of the nth code interval. The length $N+1$ phase difference code is then stored in vector $\mathbf{x}$, which parameterizes the complex baseband PCFM waveform

$$s(t;\mathbf{x}) = \exp\left\{ j \left(\int_0^t g(\tau) * \left[\sum_{n=1}^{N} \alpha_n \delta\left(\tau - (n-1)T_{\text{p}}\right) \right] d\tau + \theta_0 \right) \right\}. \tag{2.50}$$

The shaping filter $g(t)$ can take any form as long as it integrates to unity with full time support over the length of the pulse, T_{p}. This requirement is unique to the radar implementation of polyphase codes so as to avoid any overlap in time.

A step-by-step graphical representation of the PCFM waveform generation scheme from (2.50) is shown in Figure 2.13. In this figure the polyphase code $\mathbf{x}$ is fed into a block that creates a uniformly spaced sequence of impulses indexed by n. Next the shaping filter $g(t)$ (typically a rectangular shaping filter) is applied to the impulse train.

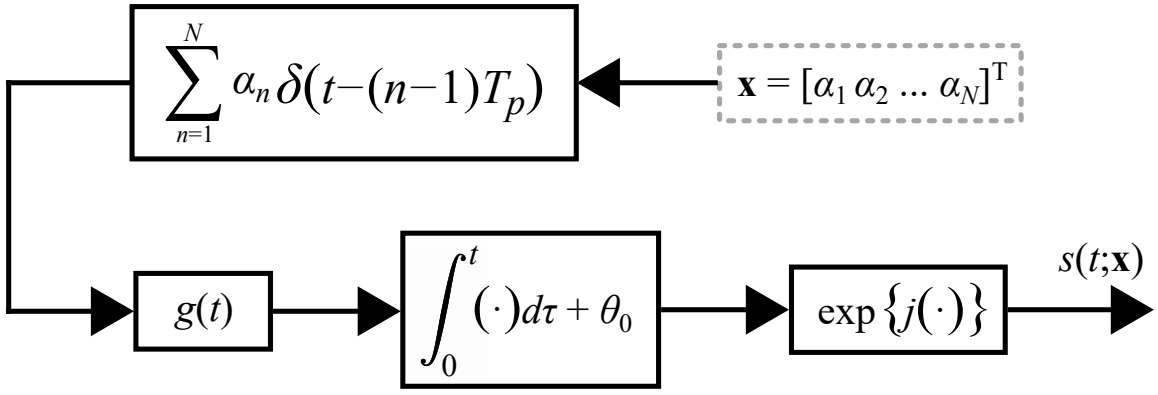

Figure 2.13: CPM implementation for generation of polyphase-coded FM waveforms.

Note that one of the requirements for PCFM to function as intended is ensuring the use of proper over-sampling to approximate a continuous emission when creating physically realizable waveforms. The flexibility that PCFM provides allows for optimization of the polyphase code based on design requirements and system parameters [96–104]. Though this is not a focus of this work current research efforts utilizing optimized PCFM are ongoing [21, 105]. Instead, this work uses PCFM to initialize the the waveform generation scheme described in section 2.10 and to create spatial offset sequences for the purpose of fast-time beam steering in Chapter 4. Though it is not required for its function, initializing with a waveform that is already constant modulus and exhibits a Gaussian-like spectrum facilitates a slightly faster spectral optimization time.

Even though there is extensive literature on the use and implementation of PCFM waveforms, a solid background was provided here due to its ubiquitous use throughout this work. As will be explained in later sections, the application of PCFM will be expanded to facilitate the implementation of continuous spatial signals, as well as continuous radar waveforms loaded onto test equipment for experimental testing.

2.10 Pseudo-Random Optimized Frequency Modulation (PRO-FM)

True noise waveforms possess random amplitude and frequency modulation to imitate white noise as best as possible. Transmitting these noise waveforms causes several implementation problems inherent to their design including range limitations and target returns possessing varying magnitudes, all stemming from AM effects. Noise is difficult to transmit at high power due to the need for an amplifier to quickly adjust the output power levels as a function of fast-time. High power RF transmitters prefer to operate in saturation to deliver consistent power to targets and to avoid signal distortion. By throwing out the AM portion of noise waveforms only random FM remains. The pseudo-random optimized FM or PRO-FM waveform generation scheme creates constant modulus FM-noise waveforms with an optimized spectrum. The spectral optimization ensures good containment compared to the flat spectrum of an unoptimized FM-noise waveform. This implementation scheme leverages the large number of waveform degrees of freedom associated with

FM noise waveforms and avoids the use of traditional computationally expensive receive processing. The high dimensionality afforded by FM-noise radar waveforms provides subsequent high levels of separability such that, with sufficient coherent processing, return signal echoes will be separable. The coherent processing gain is proportional to the total number of waveforms in the CPI. Each waveform segment is independently initialized with a random FM waveform to create a non-recurrent and non-repeating waveform generation scheme.

The same spectral optimization developed in [20, 106] is used for each waveform segment, denoted $s_{0,\ell}(t)$ for $\ell = 1,\ldots,L$. A Gaussian was chosen for power spectral density template $G(f)$ to ensure good spectral containment. Due to the Fourier transform properties of the Gaussian, the autocorrelation of a waveform with a Gaussian PSD theoretically will have no range sidelobes since the autocorrelation would, likewise, be a Gaussian. The Gaussian shape will provide theoretically infinite roll-off from the autocorrelation mainlobe, inherently providing low sidelobes. For $u(t)$, a rectangular window function is desirable when enforcing the constant modulus condition on each waveform segment.

Each PRO-FM waveform segment (or pulse) is generated from a length N random phase code distributed uniformly within $[-\pi,\pi]$. Each sample, n, of the waveform segments represents an instantaneous frequency value that is then passed through the PCFM architecture, described in section 2.9, to create a constant amplitude nonlinear FM-noise waveform. Thus, the waveform generation procedure is: 1) an independent random FM waveform segment is created, 2) a prescribed power spectral density shape is imposed on this random FM waveform, and 3) a window function $u(t)$ is applied in the time domain to ensure the pulse duration requirements are met. This alternating projection framework described by

$$r_{k+1,\ell}(t) = \mathbb{F}^{-1}\Big\{|G(f)|\exp\Big(j\angle\mathbb{F}\big\{s_{k,\ell}(t)\big\}\Big)\Big\} \tag{2.51}$$

and

$$s_{k+1,\ell}(t) = u(t)\exp\big(j\angle r_{k+1,\ell}(t)\big) \tag{2.52}$$

is repeated for K iterations until the signal possesses a power spectral density that sufficiently resembles a Gaussian. Refer to Figure 2.14 for a step-by-step look at the PRO-FM algorithm. Here, $\mathbb{F}$ and $\mathbb{F}^{-1}$ represents the Fourier and inverse Fourier transforms, respectively, and $\angle(\bullet)$ extracts the phase from the argument of the complex exponential in (2.51) and (2.52).

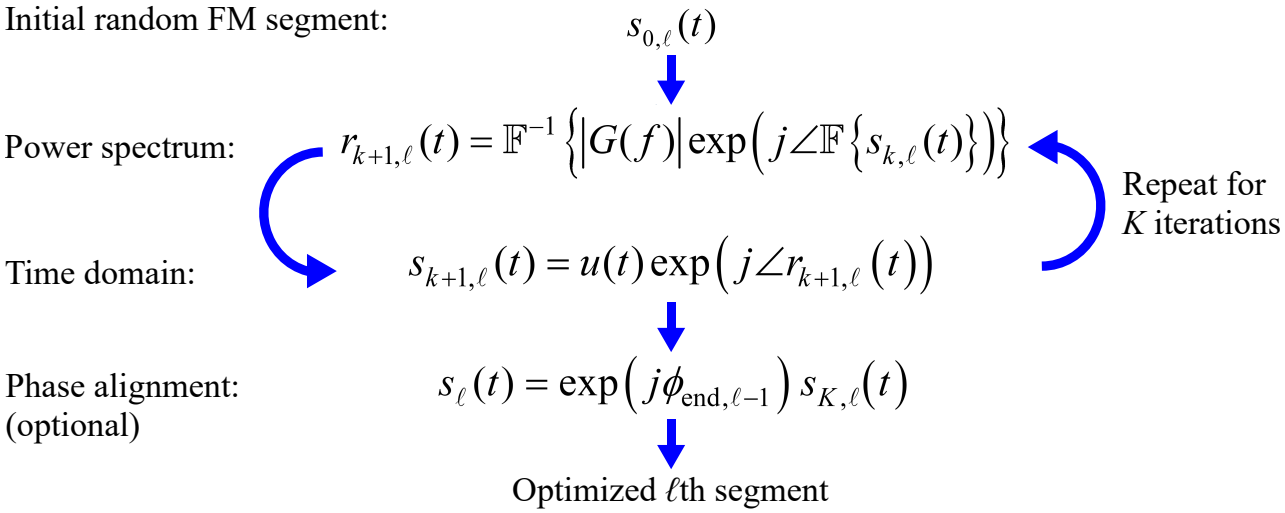

Figure 2.14: Flow diagram describing each step of the PRO-FM algorithm.

Notice that there is a fourth step shown in Figure 2.14. This step involves a phase rotation of the ℓth optimized PRO-FM segment to avoid phase discontinuities between adjacent segments. The ℓth segment is rotated such that the first sample of the waveform possesses the same phase as the last sample of the $(\ell-1)$th segment. This step is only necessary when operating in a continuous wave (CW) mode, like in [20]. The PRO-FMCW implementation offers several benefits over pulsed PRO-FM. One such benefit is that the BT (which determines the dimensionality of the waveform) is extended to 10^6 or greater. Continuously emitting a non-recurrent FM-noise waveform also provides inherent robustness to the emission from interference.

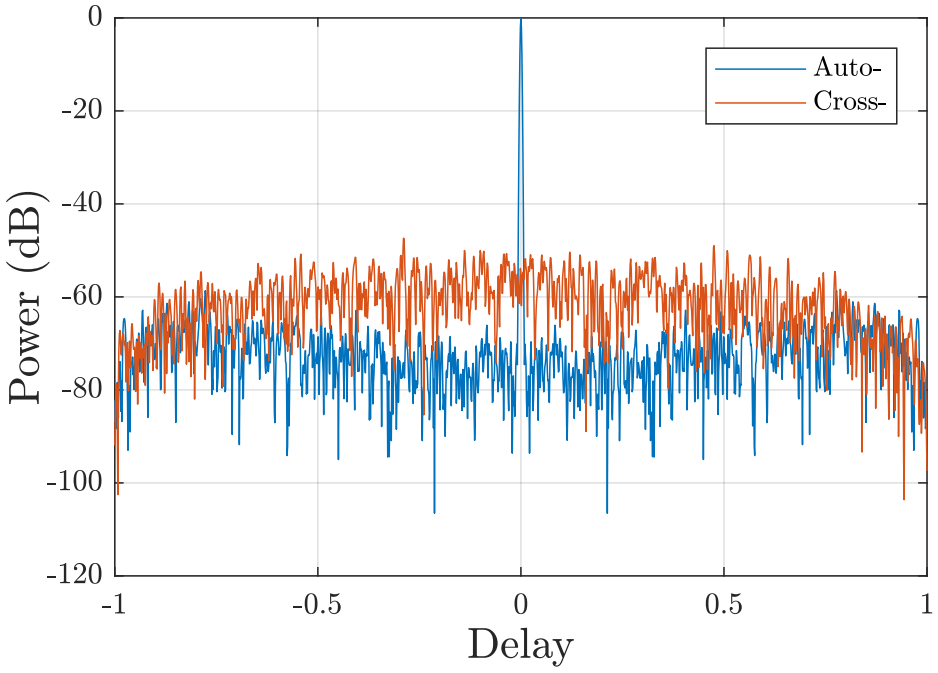

Figure 2.15: Auto- and cross-correlations of L=1000 coherently integrated PRO-FM waveform segments.

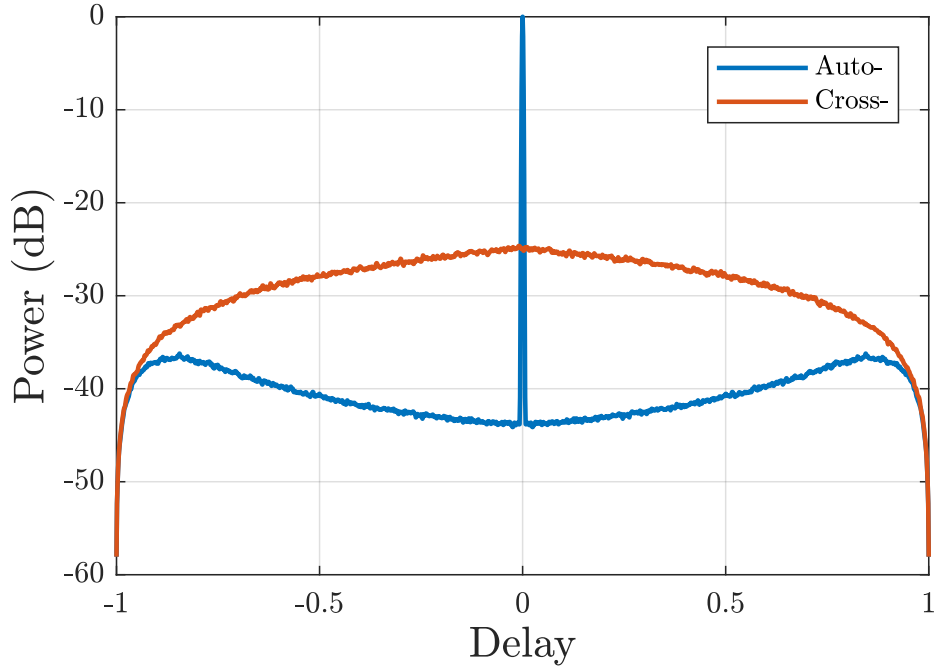

Figure 2.16: RMS auto- and cross-correlations of L=1000 coherently integrated PRO-FM waveform segments.

As an example of the benefits of high dimensional FM noise radar waveforms, consider the following example. Using the method described above and (2.51) and (2.52) a set of L=1000 waveforms with BT of 200 was generated. Shown in Figure 2.15 is the auto/cross-correlation of L coherently integrated PRO-FM waveforms. The benefits of the random nature of these FM noise waveforms is easily observable here as the random autocorrelation sidelobes combine in a destructive nature, effectively lowering them as a function of L. In Figure 2.16 is the root-mean-square (RMS) auto/cross-correlation which shows the average of what one could expect to see on a pulse-by-pulse basis. Comparing the average levels of auto/cross-correlation reveals that the benefits of coherent integration follow the dB scale, with an approximate improvement of 30 dB corresponding to the 1000 averaged pulses/segments.

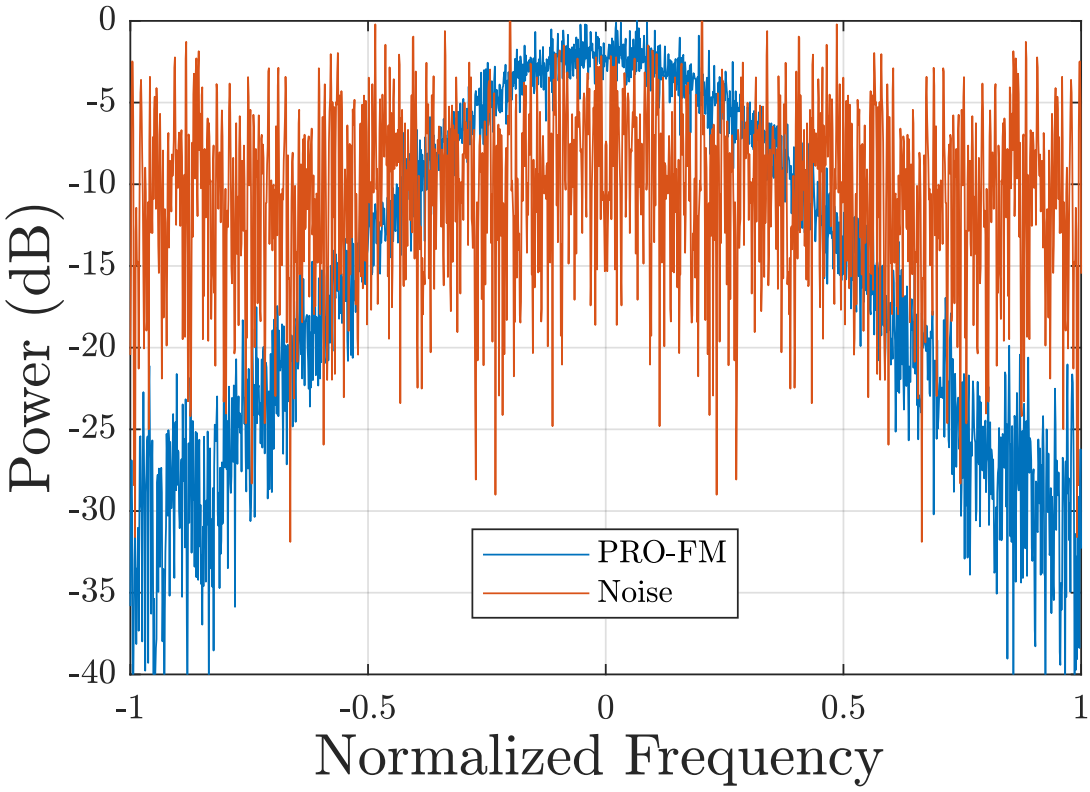

Figure 2.17: Spectra of a single PRO-FM waveform (blue) and noise waveform (red).

To illustrate the good spectral containment associated with the PRO-FM FM-noise waveform, consider Figure 2.17. This figure displays a comparison between the peak normalized power spec-

tra of a random noise waveform (containing AM and FM) and the PRO-FM waveform. As expected, the pure noise waveform exhibits a flat frequency response across all frequencies and the PRO-FM resembles a Gaussian. Note that the two spectra are formed from a single waveform of each case.

Chapter 3

A Simultaneous Dual-Polarized PRO-FM Emission

The main motivation driving research on full polarimetric radar is the ability to recover the complete scattering matrix for any arbitrarily shaped object. As described in section 2.6, transmitting and receiving orthogonally polarized waveforms that possess good separability (also called polarization purity) over a CPI allows for the copolarized (i.e. HH and VV) and cross-polarized (i.e. HV and VH) responses to be separated. The ability to do this is desirable in many applications, ranging from target classification and identification to use in remote sensing. The weather sensing and prediction community has driven a lot of the research behind dual-polarization radar modes. Having this functionality allows weather radar technicians to better estimate the size and type of precipitation, including determining precipitation mixes [107].

Many radar systems transmit and receive emissions with a single polarization (often times horizontal) or utilize a transmission scheme which interleaves orthogonally polarized waveforms (such has horizontal/vertical or left-/right-hand circular) when utilizing a dual-polarization mode [11]. Alternating adjacent pulses with different polarizations, following the sequence described in Figure 3.1, is required to provide proper separability between received responses when the same underlying waveform is emitted on both polarizations. If, for example, an LFM was to be emitted simultaneously in horizontal (H) and vertical (V) polarizations the received echoes would provide poor separation between the two polarization modes (refer to section 3.2 for an example using this configuration). Another disadvantage when alternating between orthogonal polarizations between adjacent pulses is a doubling of the *PRI* if both polarizations utilize the same *PRI* and avoid *PRI* staggering. While this would increase the maximum unambiguous range of the system, it would also decrease the maximum unambiguous velocity or Doppler (relationship shown in sections 2.1

and 2.7). Careful consideration must be exercised when selecting the maximum unambiguous range due to the possibility of multipath or multiple time around pulses being received during the listening time of the incorrect polarization. An occurrence similar to what is described in Figure 2.2 but when the echoes from a transmitted H pulse are received during the V observation period, or vice-versa. This issue would equate a degradation in the purity of co- and cross-polarized responses of the current received pulse by mixing in ambiguous target data.

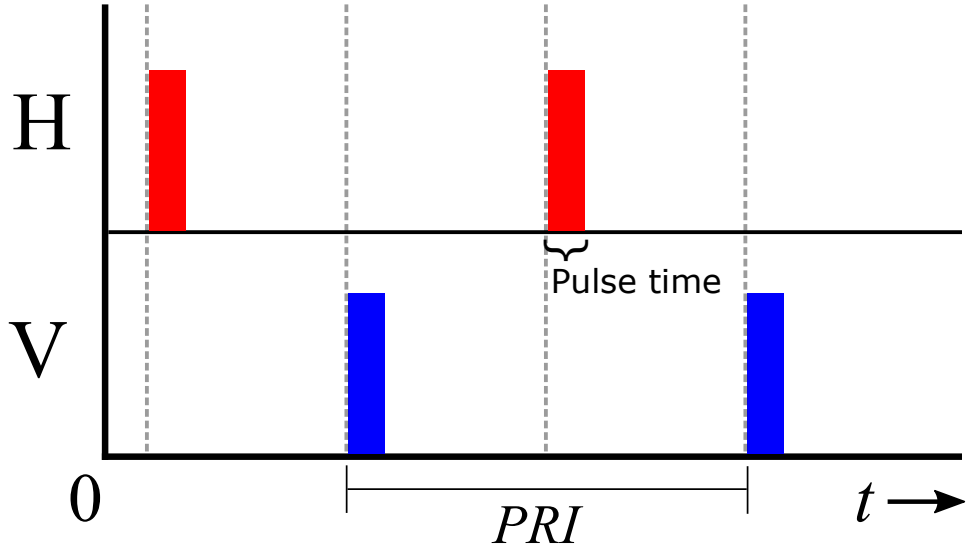

Figure 3.1: Example pulse scheduling for interleaved orthogonal polarization modes h(orizontal and vertical) when both polarization modes emit the same underlying waveform.

There has been some work completed on polarimetric noise radar, such as [108–111], but have been mostly restricted to short range and low power implementations. Through recent research efforts [70], a form of adaptive pulse compression (APC) has been applied on receive to aid in the separation of the co-polarized and cross-polarized responses, though computationally expensive. This has been applied to arbitrarily shaped FM waveforms. The emission scheme proposed here, developed in [112], will utilize two independent, but co-located, transmitters to simultaneously emit orthogonally polarized and independently generated FM-noise waveforms. An example of the simultaneous pulse schedule is shown in Figure 3.2. Figure 3.3 describes the emission of orthogonally polarized sinusoids in the Cartesian coordinate system. This emission scheme will illuminate two dimensions of any scatterer (and the surrounding environment) to provide complete

estimation of the RCS of the targets as opposed to estimation of a single dimension.

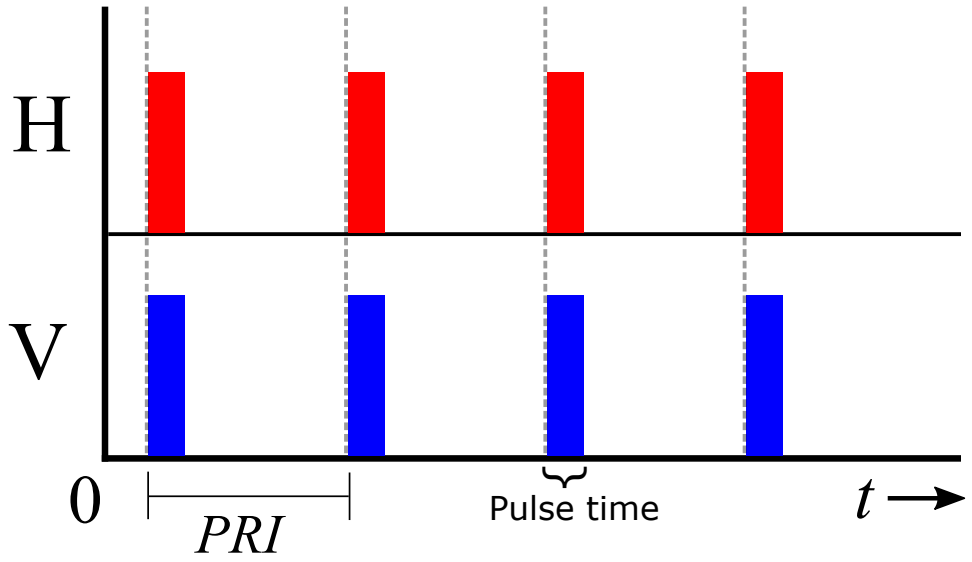

Figure 3.2: Example pulse scheduling for simultaneous emission of orthogonal polarization modes (horizontal and vertical) using the PRO-FM waveform.

Due to the high dimensionality of the PRO-FM waveform, described in detail in section 2.10, and the random nature of the received range sidelobes, coherent integration over multiple pulses provides good separability between orthogonally polarized emissions. This separability stems from the low cross-correlation of the FM-noise waveforms due to their non-repeating structure when coherently integrated over a CPI.

Collecting target data described by two polarizations improves chances of detection as well as effectively doubles the amount of information gathered by interrogating the target in orthogonally polarized dimensions. This leads to a doubling in collected data as well, but with modern data recording and storage systems data handling is no longer an issue. The trade-off between costly receive processing and high dimensional waveforms will be investigated briefly in later sections. The use of presumming, a common processing technique used in SAR to reduce data handling requirements, will be investigated as well as the benefits it provides when using FM-noise waveforms. The main takey-away is that by using two high dimensional waveforms to process over enough pulses (or CW segments) will yield a lower computational cost when compared to adaptive algorithms. The trade-off here (because nothing is free) is that this method requires many

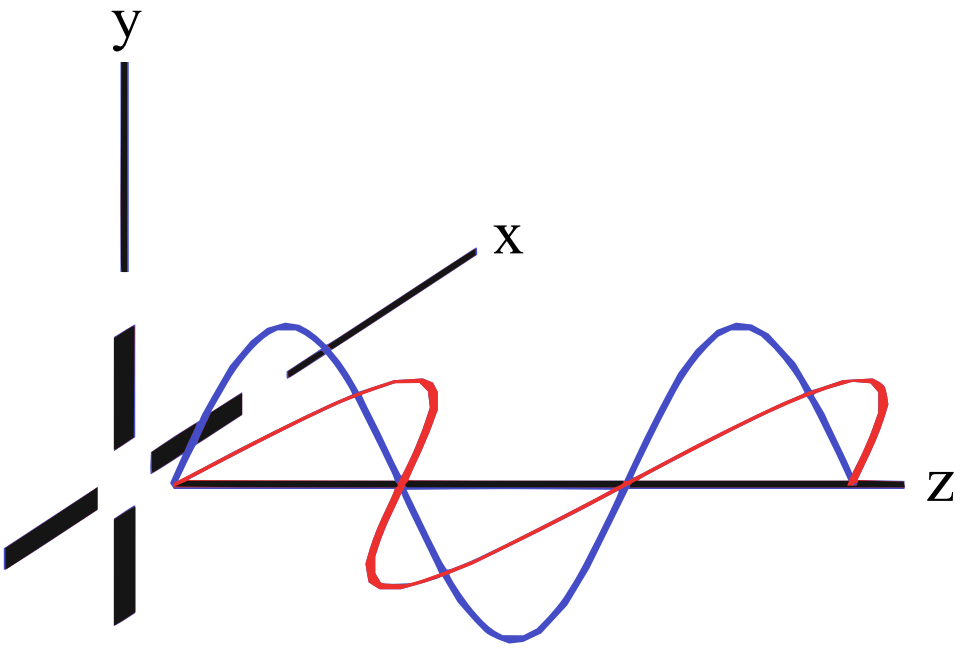

Figure 3.3: Simultaneous emission of orthogonally polarized sinusoids.

pulses on target compared to potentially less pulses but higher computational cost.

Experimental open-air testing and computer simulations will be used to compare three main test cases. The first being an implementation of LFM waveforms in a "ping-pong" (or polarization interleaved) transmission mode similar to what is described in Figure 3.1. This will be used as the baseline to compare with the results when using simultaneous LFMs and simultaneous PRO-FM waveforms. The main metric used to compare the results will be the separability between the co- and cross-polarized terms. This separability is described by how well simple radar processing techniques can tease apart the different returns for the two orthogonal receive polarizations. The cross-correlations of the waveform pairs for each test case will be used to determine polarization separability. The ability to create range-Doppler plots from receive data will also be evaluated.

3.1 Recipe for Simultaneous Emissions

By exploiting the high dimensionality of FM noise waveforms, a simultaneous dual-polarized radar emission scheme can be formulated such that, over a CPI, orthogonally polarized returns are sufficiently separable. Here, the chosen polarizations are horizontal (H) and vertical (V) but

this method could potentially be applied to other orthogonal polarization modes. Utilizing the alternating projections spectral optimization scheme described in section 2.10, two independent PRO-FM waveforms are generated with prescribed pulse-length T_{p}, proportional to the waveform time-bandwidth product (BT) for the approximate 3-dB bandwidth. Doing so sets the average cross-correlation of a single waveform as proportional to BT. Each waveform is then spectrally optimized independently, which decreases B and increases the level of cross-correlation between the two waveforms. The spectral optimization involves imposing a desired power spectral density shape onto the waveforms. For this case a Gaussian is desirable for two main reasons: 1) the Gaussian shape affords good spectral containment while 2) exploiting the Fourier relationship between PSD and autocorrelation to create an autocorrelation function that theoretically has no range sidelobes. The PRO-FM waveform generation and optimization is completed independently for the H and V waveforms by alternating between

$$r_{k+1,\ell}^{[\mathrm{H}]}(t) = \mathbb{F}^{-1}\left\{ |G(f)| \exp\left(j\angle \mathbb{F}\left\{ s_{k,\ell}^{[\mathrm{H}]}(t) \right\} \right) \right\} \tag{3.1a}$$

$$r_{k+1,\ell}^{[\mathrm{V}]}(t) = \mathbb{F}^{-1}\left\{ |G(f)| \exp\left(j\angle \mathbb{F}\left\{ s_{k,\ell}^{[\mathrm{V}]}(t) \right\} \right) \right\} \tag{3.1b}$$

and

$$s_{k+1,\ell}^{[\mathrm{H}]}(t) = u(t) \exp\left(j\angle r_{k+1,\ell}^{[\mathrm{H}]}(t) \right) \tag{3.2a}$$

$$s_{k+1,\ell}^{[\mathrm{V}]}(t) = u(t) \exp\left(j\angle r_{k+1,\ell}^{[\mathrm{V}]}(t) \right) \tag{3.2b}$$

to impose the desired PSD template and enforce the time-domain envelope requirements with a rectangular window function, $u(t)$. After the Kth iteration of the PRO-FM optimization, the two independent waveforms possess a PSD that sufficiently resembles a Gaussian, two new independent random FM-noise waveforms are then optimized. This process is repeated for the two sets of L total waveforms. The optimization iteration variable k will be dropped off when referring to the

optimized waveforms from here on for the sake of brevity, leaving $s_{\mathrm{H,L}}(t)$ and $s_{\mathrm{V,L}}(t)$ representing each set of optimized waveforms.

While the separability of each set of waveforms may not be sufficient on a pulse-to-pulse basis, the coherent combination of enough pulses provides excellent separability, as shown in the figure below. The separability of the two sets of waveforms is described by the cross-correlation between the H and V sets of waveforms, barring all hardware restrictions. As shown in Figure 3.4, a coherent combination over a CPI containing $L = 1000$ waveforms yields about 55 dB of separation between the H and V channels in simulation. Simply put, the cross-correlation determines the ability to tease apart co- and cross-polarized returns. Notice that the results mirror what is observed in section 2.10.

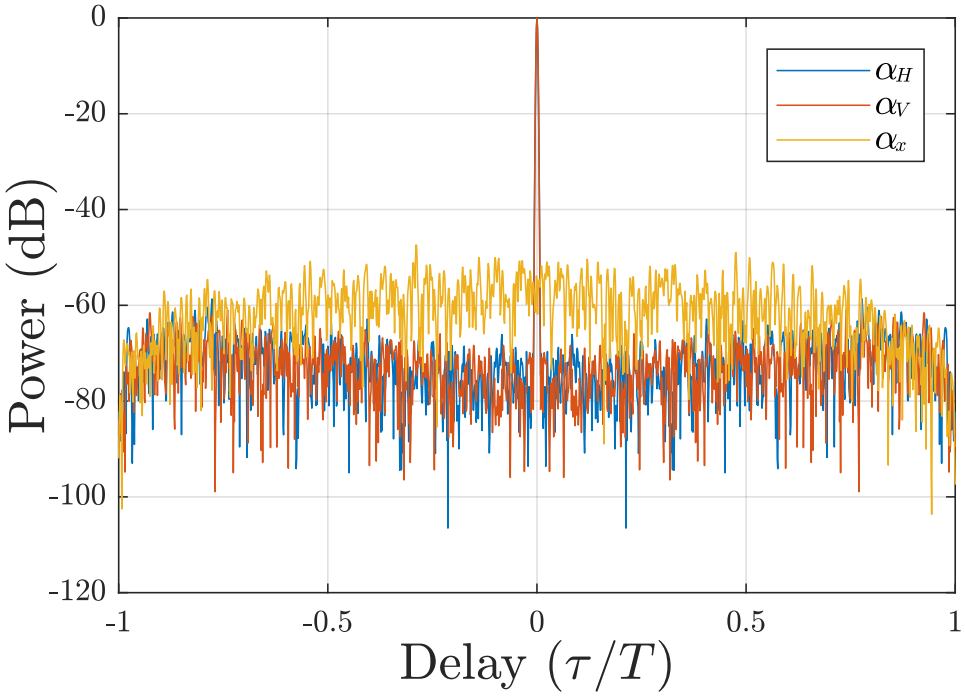

Figure 3.4: Comparison of auto- and cross-correlations of two independently generated and coherently integrated PRO-FM waveforms of size L=1000 segments.

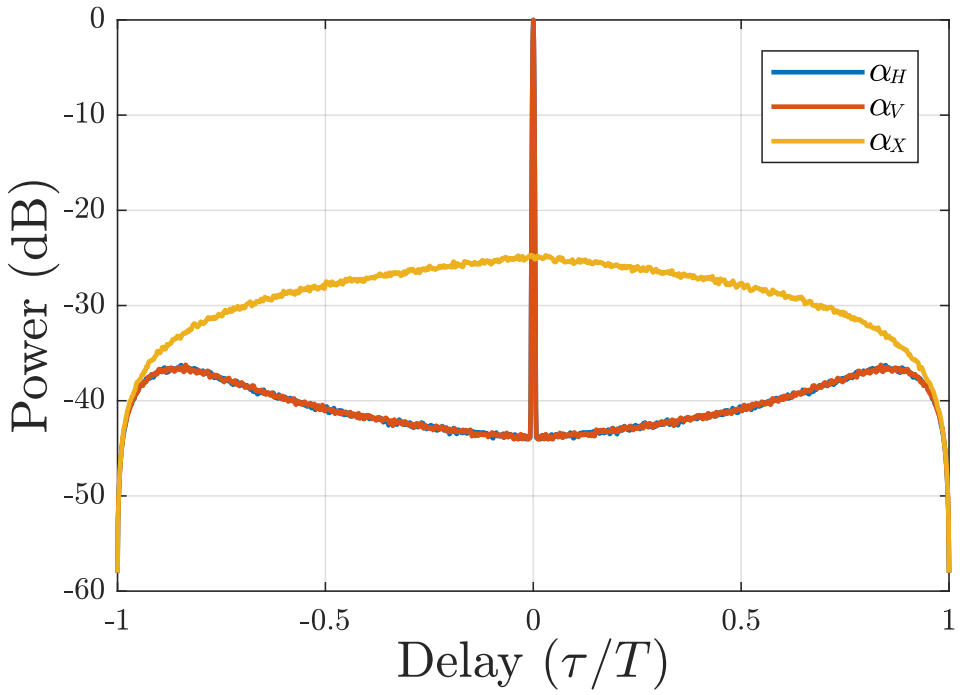

Figure 3.5: Comparison of RMS auto- and cross-correlations of two independently generated and coherently integrated PRO-FM waveforms of size L=1000 segments.

In Figures 3.4 and 3.5 two sets of coherently integrated waveforms are compared via their normalized auto and cross-correlations. The two sets of FM-noise waveforms, representing the H and V transmit channels, exhibit an auto/cross-correlation response that improves relative to the number of L independent waveforms. Cross-correlation between the two polarization channels maintains the same benefits as shown in previous work on PRO-FM when comparing a single set of waveforms to itself. The separability with respect to polarization is then represented as the cross-correlation between the H and V channels. Figure 3.5 depicts what one might expect the auto/cross-correlation of a single waveform pair to be on a pulse-to-pulse basis. Despite lacking any coherent integration, the RMS correlations display good separability with about 25 dB separation between the H and V channels during each pulse (note that the variation of the pulse-to-pulse response would vary much more than Figure 3.5 implies).

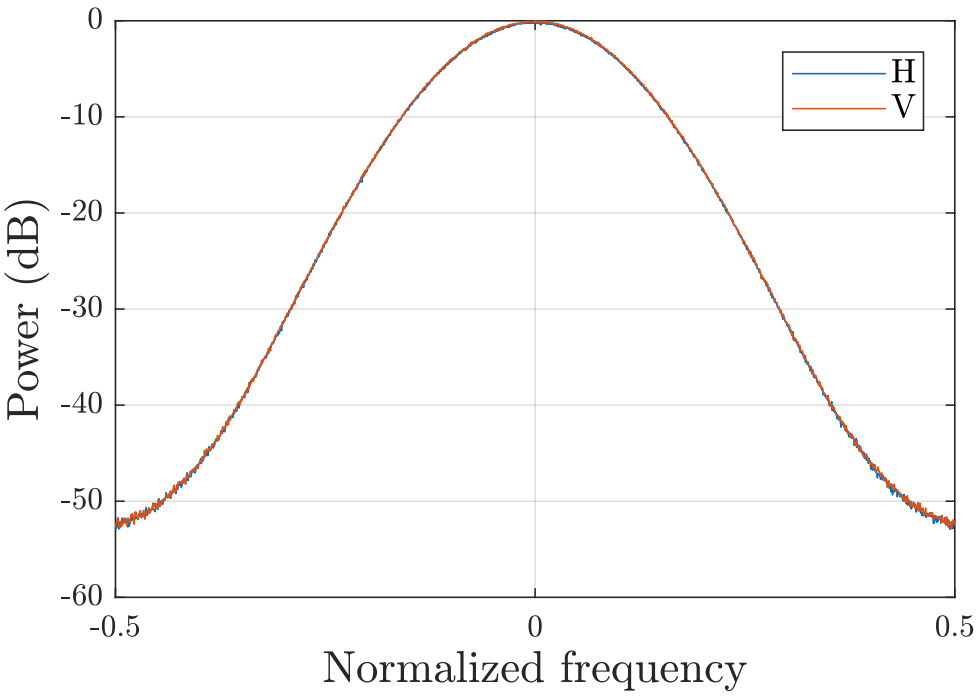

Figure 3.6: Spectrum of horizontal and vertical waveforms of size L=1000 segments after coherent integration.

Figure 3.6 depicts the peak normalized spectra of the H and V channels after coherent integration of 1000 unique waveform pairs. It is important to note that the waveform pairs occupy the same portion of the spectrum, as shown in Figure 3.6, and thus rely solely on the non-repeating structure of the PRO-FM formulation to reduce autocorrelation sidelobes through coherent integration over the CPI. The simulated spectrum of each polarization mode sufficiently resembles that of the Gaussian spectral template and exhibits good spectral containment too. The steep roll-off of the Gaussian provides good attenuation at frequencies outside of the 3-dB bandwidth as well.

In the next section the characteristics of dual-polarized PRO-FM will be investigated via simulations of various target responses offset in range and Doppler. Each point target will possess different polarized responses as well.

3.2 Dual-pol Simulations

Simulating the dual-polarized PRO-FM emission scheme provides a baseline for performance expectations and analysis before moving to open-air testing. While these simulations do incorporate a good level of realism, like clutter and noise, experimental testing is required to validate the results shown in this section. The simultaneous dual-polarized PRO-FM emission scheme will be compared to two baseline cases. The first being the simultaneous emission of LFMs in a dual-pol mode to illustrate the poor cross-correlation and separability that they provide. One channel will transmit an up-chirped LFM while the orthogonal channel will transmit a down-chirped LFM. The next test case involves the transmission of LFMs in an interleaved or "ping-pong" dual-pol mode, similar to the pulse schedule described in Figure 3.1. Operating in a pulse interleaved mode has several drawbacks like lengthening the *PRI* to accommodate the H and V channel pulses, lack of coherency between H and V received data, and degradation of signals caused by multiple time around pulses degrading cross-pol isolation. The final test case will be the simultaneous transmission of independently generated PRO-FM waveforms on orthogonal polarizaitons H and V. The benefits of utilizing a high-dimensional non-recurrent FM-noise waveform for simultaneous transmission of orthogonal polarization modes H and V will be investigated.

The scattering matrix for each simulated target will be formulated as described in section 2.6. Each target will be assigned a unique scattering matrix containing the different scattering characteristics (magnitude and phase) for the associated co- and cross-pol terms. Note that since these simulations are for a monostatic radar scenario, the cross-pol (VH and HV) terms are identical. For the sake of clarity the cross-pol terms will still be referred to as separate for the purpose of identification (but keep in mind that they are equal). The scattering matrix used to describe each target will be formulated as

$$\left[S_{\text{targ}}\right] = \begin{bmatrix} |a_{\text{HH}}|e^{j\phi_{\text{HH}}} & |a_{\text{HV}}|e^{j\phi_{\text{HV}}} \\ |a_{\text{VH}}|e^{j\phi_{\text{VH}}} & |a_{\text{VV}}|e^{j\phi_{\text{VV}}} \end{bmatrix} \tag{3.3}$$

where the cross-pol terms $|a_{HV}|e^{j\phi_{HV}}$ and $|a_{VH}|e^{j\phi_{VH}}$ are identical. Due to each target now possessing four individual responses with respect to polarization, four range profiles can be created and processed. Each simulated emission scheme will illuminate the same range profiles (barring noise and clutter) for each target and the received signals will be used to reconstruct each respective scattering matrix. Compared to the initial scattering matrices the received (albeit simulated) returns should possess distorted versions of the originals. These distortions occur due to the noise and clutter contained within the range profiles as well as receive processing losses due to windowing, etc. The goal is to investigate the changes imposed by transmission, noise and clutter on the reconstructed scattering matrix for each target.

The two simulated receive channels for the ℓth transmit pulse pair are determined by their respective co- and cross-pol terms as

$$y_{\mathrm{H},\ell}(t) = x_{\mathrm{HH}}(\tau) * s_{\mathrm{H},\ell}(t) + x_{\mathrm{HV}}(\tau) * s_{\mathrm{V},\ell}(t) + n_{\mathrm{H},\ell}(t) \tag{3.4a}$$

$$y_{\mathrm{V},\ell}(t) = x_{\mathrm{VH}}(\tau) * s_{\mathrm{H},\ell}(t) + x_{\mathrm{VV}}(\tau) * s_{\mathrm{V},\ell}(t) + n_{\mathrm{V},\ell}(t) \tag{3.4b}$$

where $x(\tau)$ represents the range profiles for each polarization as a function of time delay, $n(t)$ is additive white Gaussian noise, and $s(t)$ is the optimized PRO-FM waveforms. These receive signals contain an additional term compared to traditional transmission simulations that contains cross-polarized scattering information. Notice how each received channel is a function of the corresponding transmit polarization mode as well as the orthogonally polarized mode. Note that the noise power is proportional to the length of the transmitted waveforms and that the noise added to the ranged profiles is generated independently for H and V.

The generation of a fully polarimetric range profile must contain co- and cross-pol information just like the scattering matrix for each target, equating four total profiles (one for each polarization mode HH, HV, VH, VV). The range profiles are formulated such that the response is a function of range, or delay τ, with target characteristics injected at predetermined ranges. Randomly generated zero-Doppler clutter is added independently to each of the range profiles to simulate stationary

clutter. A small, random pulse-to-pulse phase progression is imposed on the zero-Doppler clutter to simulate internal clutter motion.

The processing used for these simulations is simple and avoids the use of any adaptive filters or estimators. The receive signals $y_{\mathrm{H},\ell}$ and $y_{\mathrm{V},\ell}$ are match filtered using the ℓth waveform from the corresponding transmit channel (H or V) and then Gaussian white noise is added to the receive signals possessing noise power proportional to BT. The pulses are then pre-summed by factor P_{pre}. The waveforms are windowed in the pulse domain to reduce Doppler sidelobes and tidy up the responses from each target. A zero-Doppler clutter projection is then implemented as described in section 2.7.1 to remove the large received power from stationary clutter. Doppler compression is then performed.

Simulating the three emission structures in this manner provides good insight into expected performance as well as an effective upper performance bound. Knowing target ground-truth information allows for characterization of the effects caused by different emission styles and the corresponding waveforms. The results of these simulations will be compared to the experimental results in the next section with discussion on differences due to the ideal nature of simulation vs the reality of experimentation.

3.2.1 Generation of Waveforms and Target Scenes

Consider table 3.1 where scattering, location, and Doppler information for five targets is displayed. The target scattering matrices are assembled based on (3.3) such that the magnitude and phase vary for each polarization mode of each target. These values were generated at random and rounded to the nearest integer or fractional multiplicative of π for the sake of simplicity and ease of comprehension. The phase for each target is distributed on $(-\pi, \pi)$ and Doppler is distributed in a similar fashion on $(-\pi, \pi)$ radians per second. The target Doppler characteristics were chosen at random except for targets 2 and 5 that were assigned the same Doppler shift and only four range bins of separation. This configuration will allow for the investigation into the ability for each illumination scheme to resolve closely spaced targets in range. Note that the cross-pol scattering information

for each target is the same due to the monostatic configuration of the simulated radar system. Zero-Doppler clutter is generated at random and injected into the range profiles with a clutter-to-noise (CNR) of 50 dB, providing a more realistic scene for Doppler processing.

Table 3.1: Simulated target scattering, location, and Doppler characteristics.

Target Index	**Initial Scattering Matrices**	**Location** (Range)	**Doppler** (rad/s)
Target 1	$\begin{bmatrix} 12e^{-j\pi/2} & \frac{1}{4}e^{j2\pi/3} \\ \frac{1}{4}e^{j2\pi/3} & 8e^{j\pi/3} \end{bmatrix}$	147	$-\frac{4\pi}{5}$
Target 2	$\begin{bmatrix} 8e^{j\pi/4} & 2e^{-j\pi/6} \\ 2e^{-j\pi/6} & 4e^{j5\pi/8} \end{bmatrix}$	120	$-\frac{\pi}{6}$
Target 3	$\begin{bmatrix} 7e^{j\pi} & \frac{1}{4}e^{-j\pi/2} \\ \frac{1}{4}e^{-j\pi/2} & 2e^{j4\pi/9} \end{bmatrix}$	85	$\frac{\pi}{3}$
Target 4	$\begin{bmatrix} 8e^{-j\pi/2} & 1e^{-j\pi} \\ 1e^{-j\pi} & 6e^{j\pi/4} \end{bmatrix}$	25	$\frac{2\pi}{3}$
Target 5	$\begin{bmatrix} 7e^{j3\pi/4} & 1e^{j\pi/4} \\ 1e^{j\pi/4} & 5e^{-j\pi/3} \end{bmatrix}$	116	$-\frac{\pi}{6}$

For each simulation $L = 1800$ waveform pairs will be transmitted and received. The simultaneous and interleaved LFM emission scenario will transmit the same up/down-chirp on the H and V channels respectively, for each of the 1800 pulses (or 900 for interleaved LFM). The simultaneous dual-pol PRO-FM simulation will use 1800 independent and randomly generated PRO-FM waveforms for H and V. Each waveform was generated to possess a BT of 200 and oversampled by 3. Note that highly oversampled versions of these same waveforms will be used in section 3.3 for open-air experimental testing. The received signals are match filtered and then pre-summed by a factor of 18 for the simultaneous schemes and a factor of 9 for the interleaved LFM scheme (since the same CPI is maintained). Next the estimated range profiles are windowed using a Hanning window (example shown in Figure 2.8) to suppress Doppler sidelobes. The zero-Doppler clutter is then notched via a zero-Doppler projection. The data is then Doppler compressed and plotted.

3.2.2 Simultaneous LFM

The first simulation involves simultaneous transmission of up- and down-chirped lfm waveform pairs on polarized channels H and V respectively. Each waveform was generated to possess a BT of 200 and is oversampled by a factor of 3 relative to the 3 dB bandwidth of the signal. The transmission of these waveforms will be simulated as described above in section 3.2 and illuminate the scene described in section 3.2.1. A total of $L = 1800$ pulse pairs will be transmitted and processed to recover estimated scattering matrices and Doppler information for the five targets described in table 3.1.

First consider figures 3.7 to 3.9 which provide basic analysis of the LFM waveform pairs. This analysis will aid in the understanding of performance with respect to Doppler tolerance and recovery of co- and cross-polarized scattering information for each simulated target. The auto and cross-correlations after coherent integration for the $L = 1800$ waveforms is shown in Figure 3.7. As expected for an LFM, the H and V polarized waveforms exhibit an autocorrelation resembling a sinc^2 function shape. Note that the peak-to-sidelobe level (PSL) for both waveforms is 13 dB. The autocorrelation depicts the ideal response to a single point target at zero delay in the absence of noise. The autocorrelation for an LFM provides a good "thumbtack-like" mainlobe but relatively high sidelobes. The sidelobe structure shown in Figure 3.7 will be present for each target and will potentially mask returns from targets with lower reflected power. The cross-correlation for two LFM waveforms is mostly flat across the extent of delay τ_{max} with separability between the two waveforms of about 25 dB.

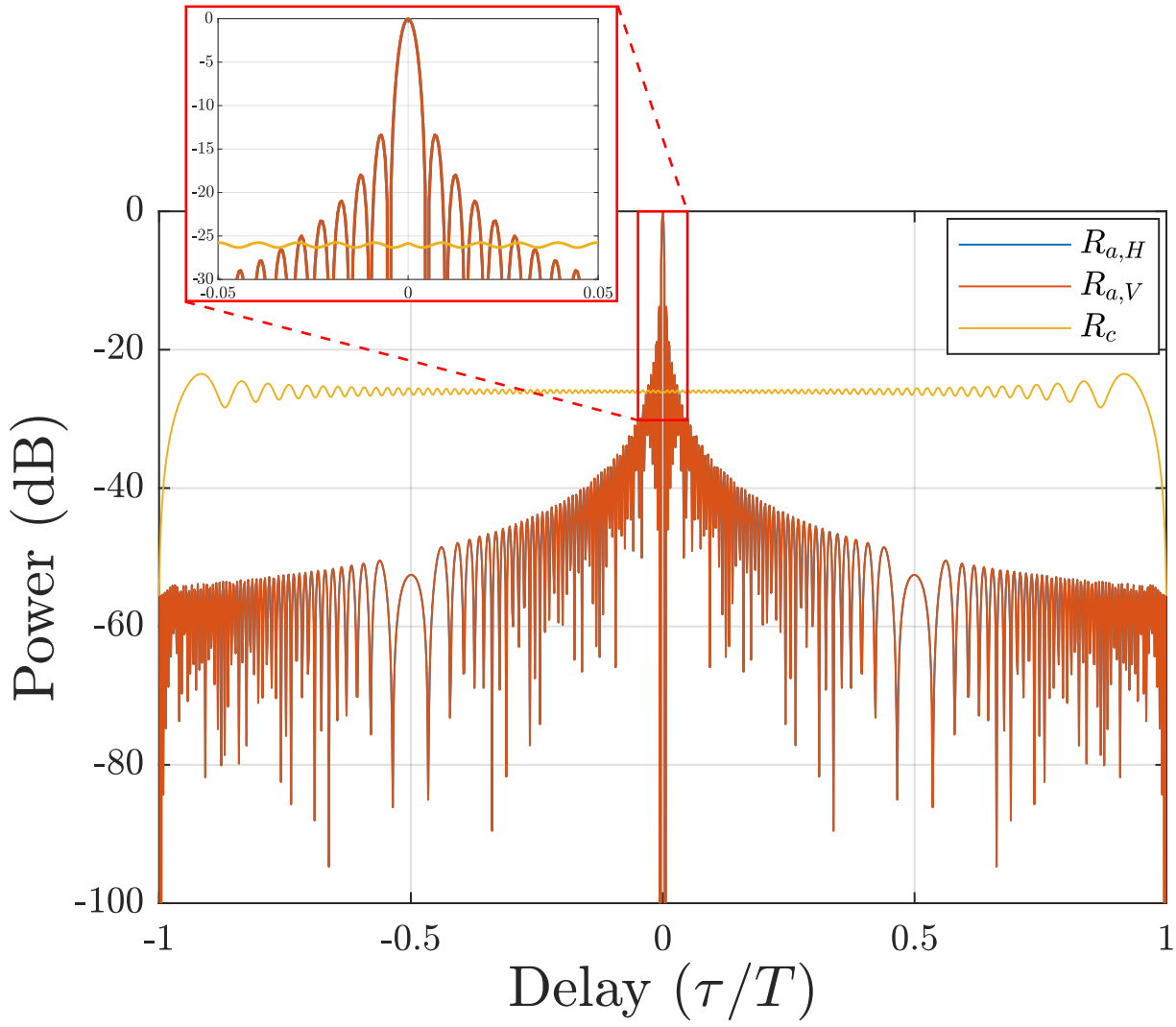

Figure 3.7: Simulated auto and cross-correlations for $L = 1800$ coherently integrated up-chirped (H) and down-chirped (V) LFM waveform pairs with $BT = 200$.

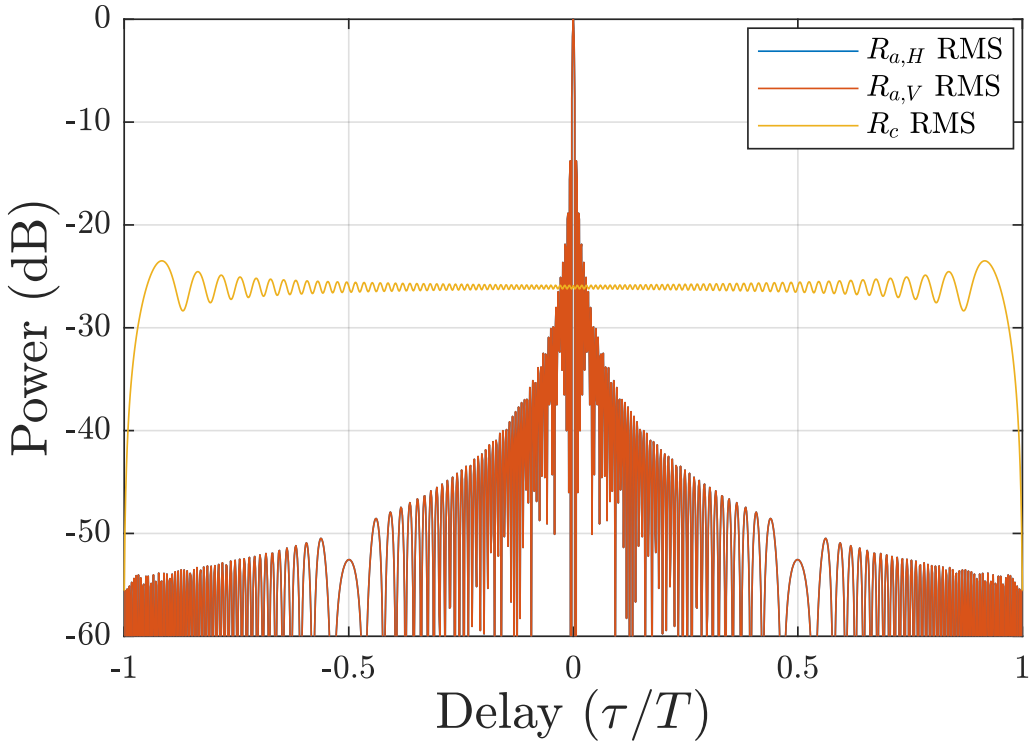

Figure 3.8: Simulated RMS auto and cross-correlations for $L = 1800$ coherently integrated up-chirped (H) and down-chirped (V) LFM waveform pairs with $BT = 200$.

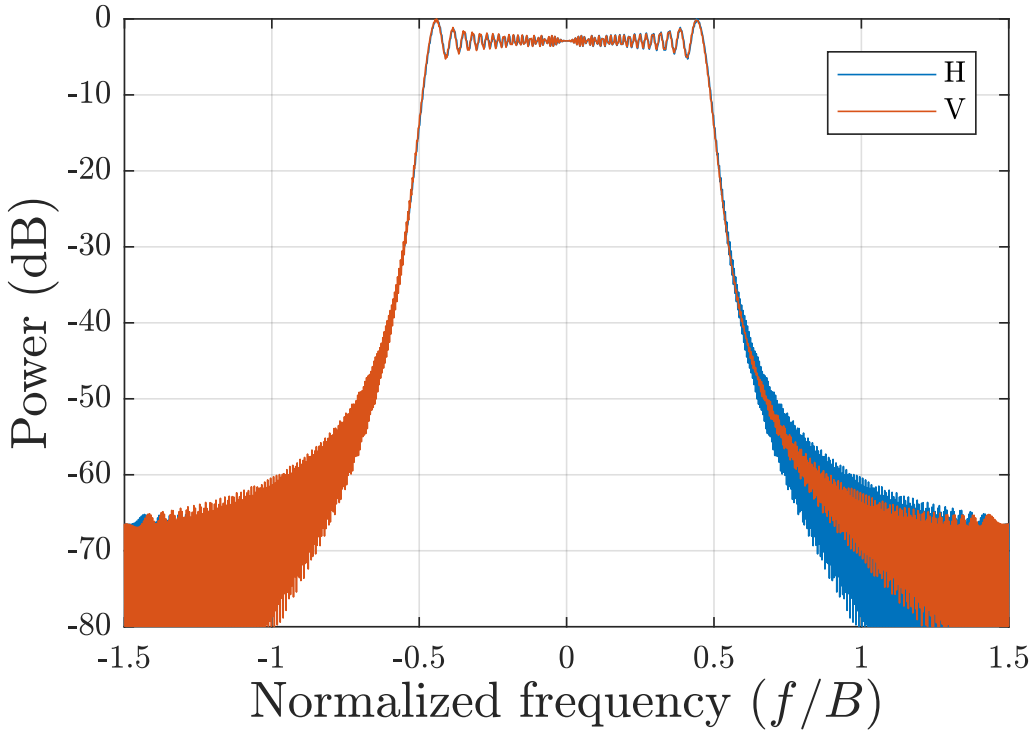

Figure 3.9: Simulated spectra of up-chirped (H) and down-chirped (V) LFM waveform pairs with $BT = 200$.

The cross-correlation of the H and V channels determines how separable the H and V polarized returns are with respect to the opposite. From Figure 3.7, the cross-polarized returns (HV and VH) should possess about 25 dB of separability but with flat sidelobe structures extending across all range. This will cause potential range ambiguities of cross-polarized returns. The RMS auto- and cross-correlations shown in Figure 3.8 describe the waveform performance on a per-pulse basis. By comparing figures 3.7 and 3.8 it is apparent that the RMS correlations and coherently integrated correlations are the same. This means that the auto- and cross-correlation performance of the LFM waveform does not benefit from coherent integration. The spectra for channels H and V is depicted in Figure 3.9. As expected both LFM waveforms occupy the same portion of the spectrum with nearly identical shapes. Note that the power is normalized to zero to better observe spectral roll-off.

Next, consider the co- and cross-polarized range-Doppler plots generated from this emission scheme. Contained in Figure 3.10 are the co- and cross-polarized responses generated from the simulated transmission, reception, and processing of simultaneous LFMs illuminating the scene described in sections sections 3.2 and 3.2.1. These plots are generated after range compression and Doppler processing. Following range compression 18 pulses were pre-summed to match the simulations in section 3.2.4 and experimental analysis in section 3.3.3. Pre-summing by this factor reduces the effective number of pulses to $L_{\text{pre-sum}} = 100$ which reduces data handling requirements and decreases the number of Doppler bins. The pulses were then windowed in the slow-time domain by a length 100 Hanning window. The windowing process is completed to reduce Doppler sidelobes at cost of slightly reduced SNR. Next a zero-Doppler projection (as described in section 2.7.1) is applied. The width of this projection was determined by the 7 principle values determined to be much greater than zero. Next the pules are Doppler compressed and plotted.

The co-pol and cross-pol range-Doppler maps display all five targets at the correct locations and Doppler shifts described in table 3.2. All responses provide good separability between targets 2 and 5 which are separated by only 4 range bins. Upon close inspection of the target returns in the co-pol plots, very faint sidelobe structure corresponding to the sidelobes observed in the autocorrelation plots from figures 3.7 and 3.8 are present. The small (-13 dB responses) repeating

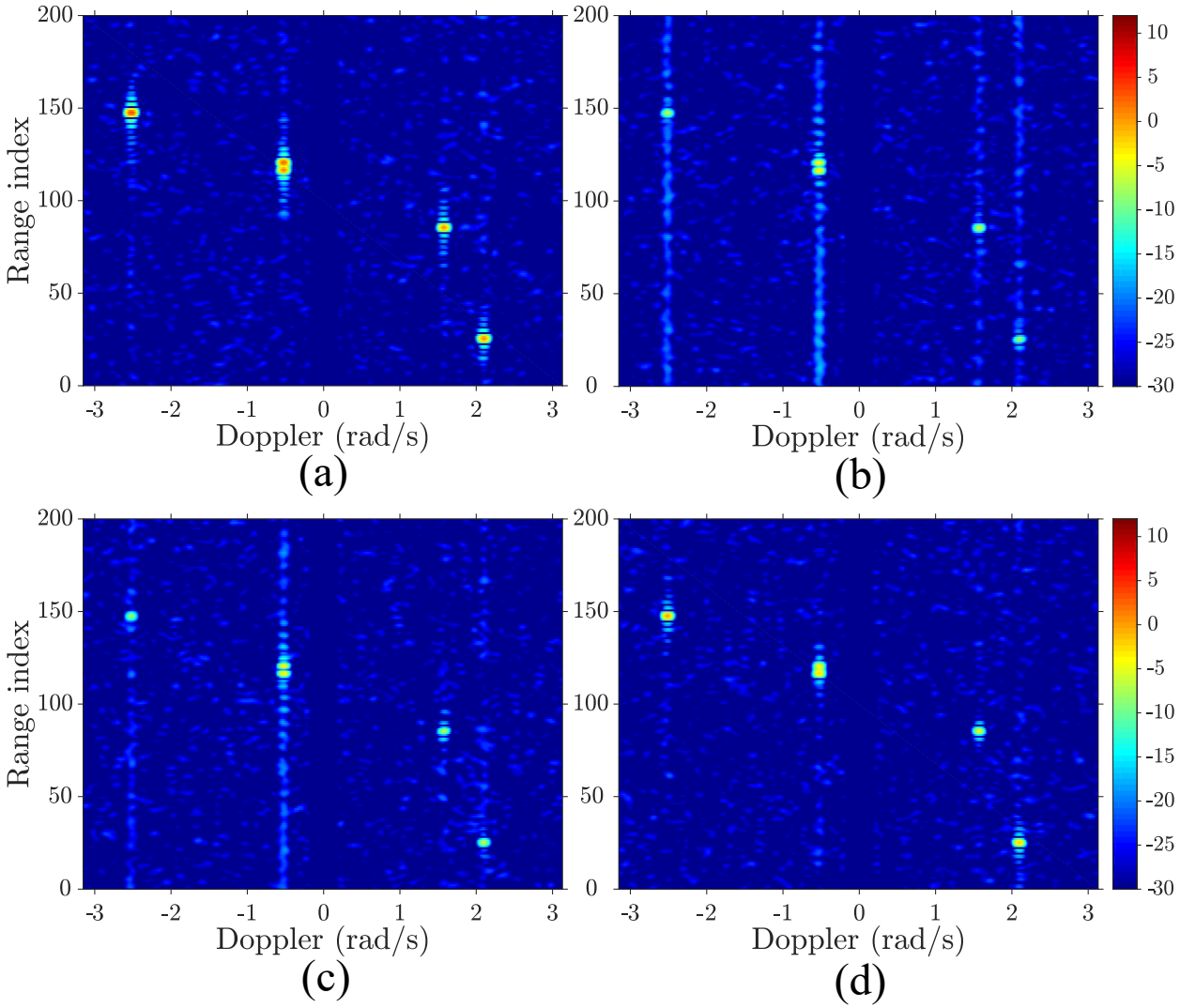

Figure 3.10: Simulated (a) HH, (b) HV, (c) VH, and (d) VV range-Doppler maps when transmitting simultaneous dual-pol LFM up/down-chirps with $BT = 200$.

sidelobe structure can be seen when observing ranges close to target 1 in Figure 3.10(a). Consider the cross-pol returns in Figure 3.10(b) and (c). Notice the striations extending from the target location across all range. These striations are the cross-correlation sidelobes depicted in Figure 3.7. This flat sidelobe structure introduces range ambiguities and possible false targets spread throughout almost all delay τ.

Table 3.2: Estimated scattering matrices, location, and Doppler information for the five simulated targets from table 3.1 when using simultaneous dual-pol LFM up/down-chirps.

Target Index	**Estimated Scattering Matrices**	**Location** (Range)	**Doppler** (rad/s)
Target 1	$\begin{bmatrix} 3.42e^{-j2.92} & -8.21e^{j0.99} \\ -7.22e^{j0.70} & -0.49e^{-j0.32} \end{bmatrix}$	147	$-\frac{4\pi}{5}$
Target 2	$\begin{bmatrix} 2.49e^{j0.33} & -4.17e^{-j0.83} \\ -4.41e^{-j1.04} & -0.74e^{j1.67} \end{bmatrix}$	120	$-\frac{\pi}{6}$
Target 3	$\begin{bmatrix} -0.11e^{-j2.28} & -7.27e^{-j0.80} \\ -6.96e^{-j0.74} & -4.79e^{-j1.63} \end{bmatrix}$	85	$\frac{\pi}{3}$
Target 4	$\begin{bmatrix} -0.01e^{j2.69} & -7.77e^{-j2.18} \\ -7.20e^{-j2.17} & -1.54e^{j1.92} \end{bmatrix}$	25	$\frac{2\pi}{3}$
Target 5	$\begin{bmatrix} 0.98e^{j2.27} & -4.18e^{j0.72} \\ -5.11e^{j0.67} & 0.79e^{-j1.31} \end{bmatrix}$	116	$-\frac{\pi}{6}$

Table 3.2 quantifies the estimated characteristics for each received target. The losses induced by this simulated emission scheme are found by comparing Table 3.2 to Table 3.1. The average losses associated with co-pol transmission/reception are between 6 and 7 dB and the average cross-pol losses are around 7 dB for each target. Note that there are slight differences between the HV and VH polarized estimated scattering characteristics. This distortion is induced by mostly noise and zero-Doppler clutter sidelobes altering the otherwise pristine reflected signal. The largest contributor to the reduction of received SNR is the Hanning Doppler window, introducing a loss of about 6.5 dB to the co-pol responses and 5.5 dB to the cross-pol responses. The trade-space to consider when choosing the appropriate window function is SNR loss vs. sidelobe reduction.

3.2.3 Interleaved LFM

The next test case involves interleaving the LFM waveforms used for test case 1. This method is commonly employed with dual-pol radar systems, however, there are some drawbacks to interleaving the pulses. The most detrimental is likely to be the reduced number of pulses-per-polarization mode placed on target within the same *CPI*. This limitation is caused by each polarization mode requiring an independent *PRI* per pulse, thus halving the number of pulses in a *CPI* for each polarization compared to a simultaneous emission mode. For this simulation $L = 900$ H and V polarized pulses will illuminate the target scene described in sections 3.2 and 3.2.1. Each waveform maintains the same BT of 200 and oversampling factor of 3. Each simulated receive pulse will have independently generated Gaussian white noise added to the signal with noise power proportional to BT.

Since the same LFM (up-chirped on H channel and down-chirped on V channel) waveforms were transmitted with this interleaved emission scheme the autocorrelations and spectra will likewise be the same as the simultaneous emission scheme. Noting, of course, that the up-chirped and down-chirped LFMs are not transmitted simultaneously and thus do not simultaneously occupy the same bandwidth. This should aid in estimation of co-pol and cross-pol target scattering characteristics at the cost of coherence between the H and V channels. Refer to figures 3.8 and 3.9 for the RMS autocorrelations as well as the spectra of the two waveforms. Unlike the test case in section 3.2.2 the cross-correlation of the two waveforms does not provide any meaningful information. The autocorrelation after coherent integration for the interleaved LFM test case is shown in Figure 3.11 for the reader's reference (even though it matches the autocorrelation for the simultaneous LFM test case).

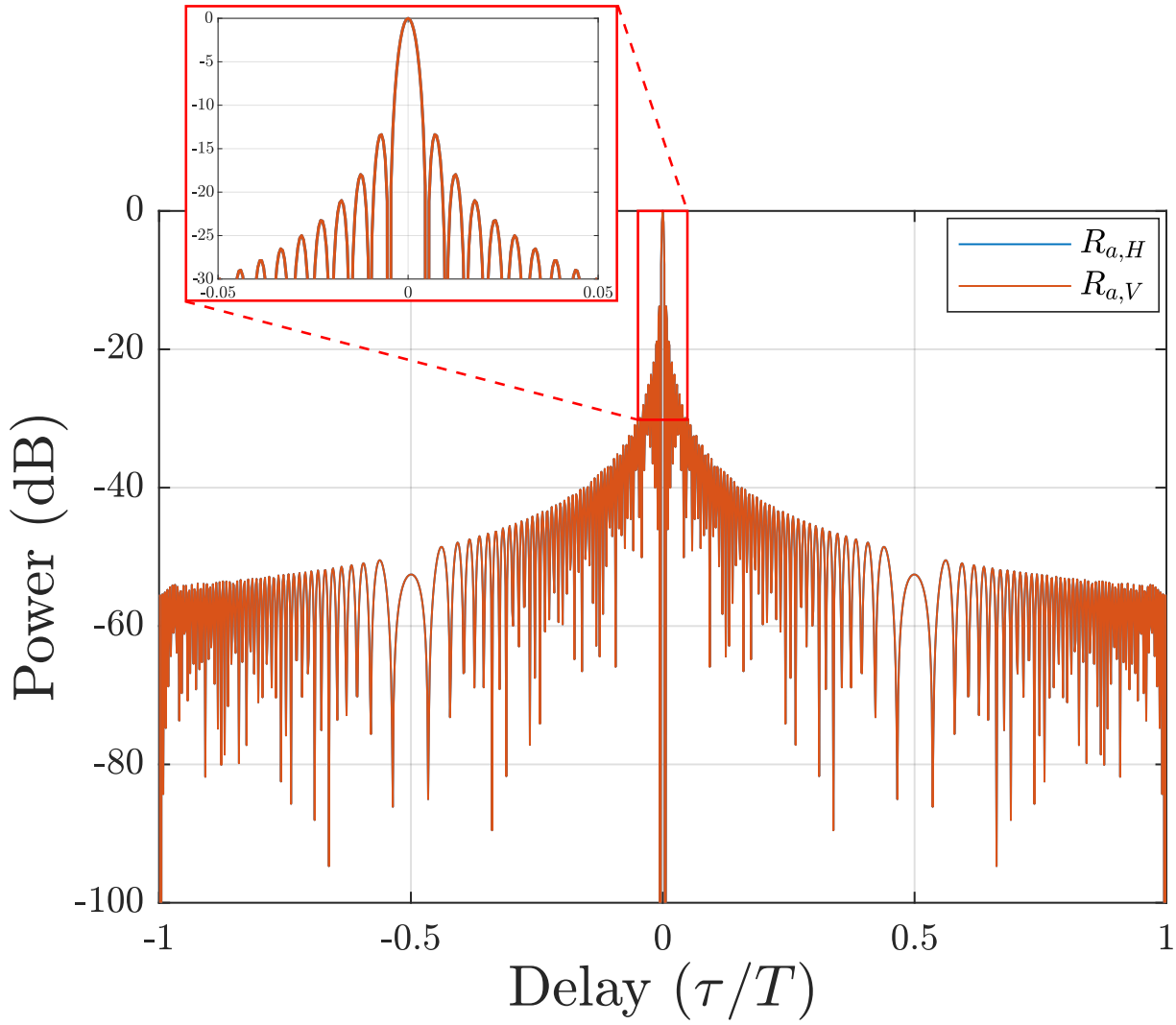

Figure 3.11: Simulated autocorrelations for $L = 900$ coherently integrated up-chirped (H) and down-chirped (V) LFM waveforms with $BT = 200$.

Next, consider the co- and cross-polarized range-Doppler plots generated from the simulated emission of 900 interleaved H and 900 interleaved V polarized pulses. Perhaps the first observation that can be made is that the noise floor is slightly higher for both the co-pol and cross-pol responses. This is due to the coherent integration of only 900 pulses per polarized channel instead of 1800. The difference is minuscule but noticeable. The next observation is that the cross-pol responses in Figures (b) and (c) lack the large smeared range sidelobes that occur during simultaneous LFM transmission. The polarization interleaved pulse schedule does not rely on cross-correlation performance when receiving cross-pol returns, hence the lack of range sidelobes. The responses from

all targets are significantly lower with respect to all four polarization modes.

Another thing to note is that all four range-Doppler plots are not entirely coherent with respect to returns shown in the HH-VV and HV-VH plots. Since the transmitter/receiver are switching between H and V polarizations in adjacent *PRI*s the exact same clutter and target characteristics are not illuminated/collected from pulse-to-pulse. This can cause slight inconsistencies when estimating the phase of each target return. The SNR under this configuration is much lower than the simultaneous dual-pol LFM emission scheme.

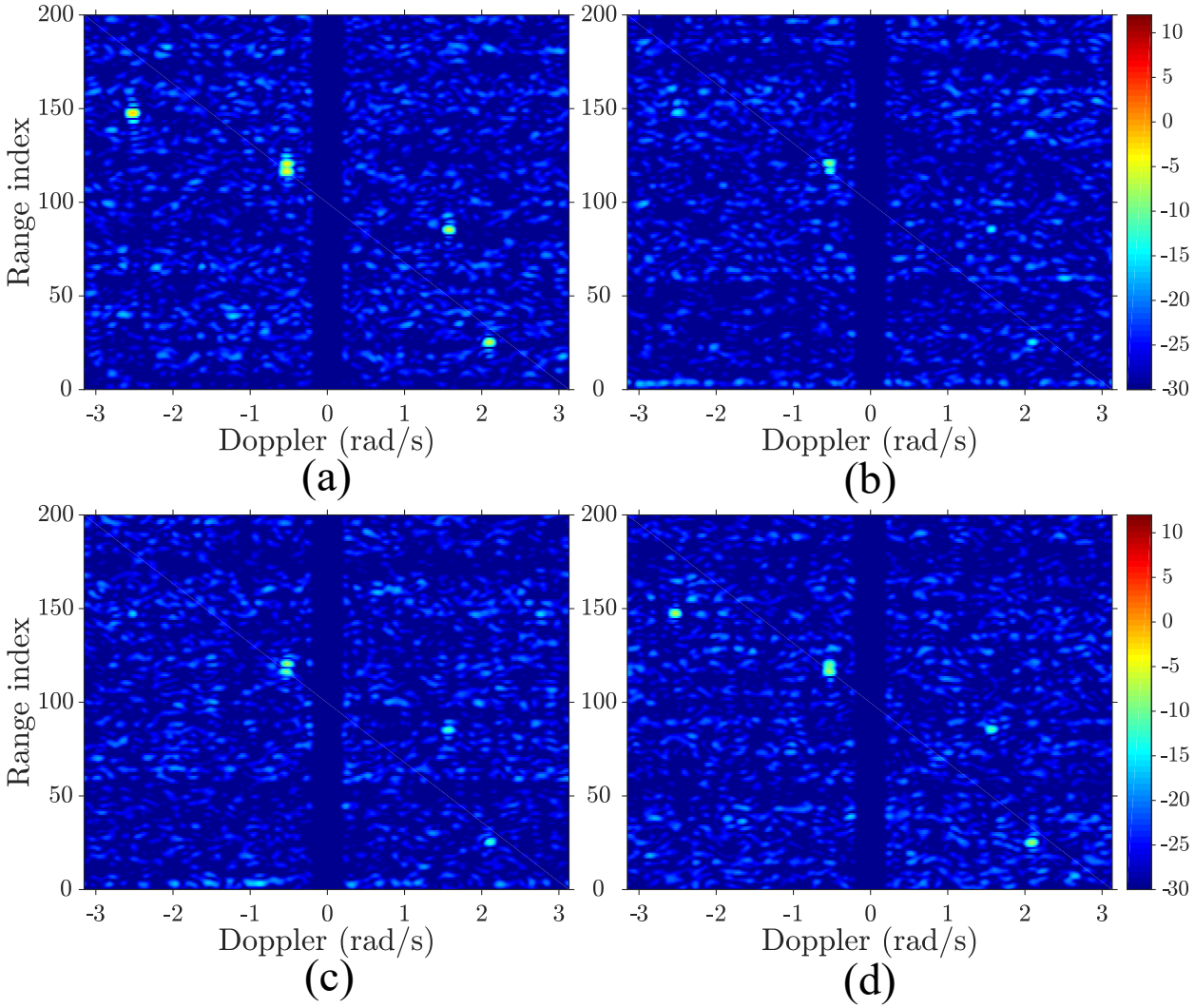

Figure 3.12: Simulated (a) HH, (b) HV, (c) VH, and (d) VV range-Doppler maps when transmitting interleaved dual-pol LFM up/down-chirps with $BT = 200$.

The reconstructed scattering matrices from this emission scheme are listed in table 3.3 with

associated range and Doppler data for each target. The average losses for the co-pol and cross-pol target responses is between 11 and 13 dB. Dual-polarized LFMs operating in an interleaved manner provides significantly worse SNR (about 5-7 dB worse performance on co-/cross-pol component estimation) when compared to simultaneous LFM.

Table 3.3: Estimated scattering matrices, location, and Doppler information for the five simulated targets from Table 3.1 when using interleaved dual-pol LFM up/down-chirps.

Target Index	**Estimated Scattering Matrices**	**Location** (Range)	**Doppler** (rad/s)
Target 1	$\begin{bmatrix} -2.28e^{-j2.81} & -13.16e^{j0.68} \\ -14.98e^{j0.78} & -6.98e^{-j0.30} \end{bmatrix}$	147	$-\frac{4\pi}{5}$
Target 2	$\begin{bmatrix} -3.79e^{j0.40} & -11.07e^{-j0.99} \\ -9.38e^{-j1.00} & -6.51e^{j1.69} \end{bmatrix}$	120	$-\frac{\pi}{6}$
Target 3	$\begin{bmatrix} -6.42e^{-j2.31} & -12.65e^{-j0.67} \\ -12.17e^{-j0.71} & -10.74e^{-j1.69} \end{bmatrix}$	85	$\frac{\pi}{3}$
Target 4	$\begin{bmatrix} -5.60e^{j2.66} & -12.03e^{-j2.05} \\ -12.83e^{-j1.98} & -8.40e^{j1.88} \end{bmatrix}$	25	$\frac{2\pi}{3}$
Target 5	$\begin{bmatrix} -4.68e^{j2.35} & -13.65e^{j0.75} \\ -11.20e^{j0.68} & -4.95e^{-j1.31} \end{bmatrix}$	116	$-\frac{\pi}{6}$

3.2.4 Simultaneous PRO-FM

The final test case involves the simultaneous emission of 1800 independent PRO-FM pulse pairs on orthogonal polarizations H and V. Two sets of $L = 1800$ PRO-FM waveforms were generated with $BT = 200$ for each waveform. Each waveform is oversampled by a factor of 3 as well, similar to the previous two test cases. The simulated transmission and reception of these waveforms is handled as described in sections 3.2 and 3.2.1. Each pulse pair will be convolved with a range profile containing zero-Doppler clutter, the five targets and associated scattering, location, and Doppler information from Table 3.1. Independently generated Gaussian noise will be added to each receive channel with a noise power proportional to BT.

First consider the auto- and cross-correlations for 1800 coherently integrated PRO-FM waveform pairs. The analysis of these characteristics, just like in previous sections 3.2.2 and 3.2.3, will aid in the understanding of proceeding analysis. As shown in Figure 3.13 the autocorrelation

sidelobes for both H and V channel waveforms exhibit suppression to nearly -65 dB down from the peak of the ACF. This performance provides a thumbtack-like appearance to the autocorrelation and delay-Doppler ambiguity function (not shown). A major difference between the PRO-FM and LFM correlation performance is the improvement from coherent integration (improved as a funciton of L) seen in the PRO-FM auto- and cross-correlations.

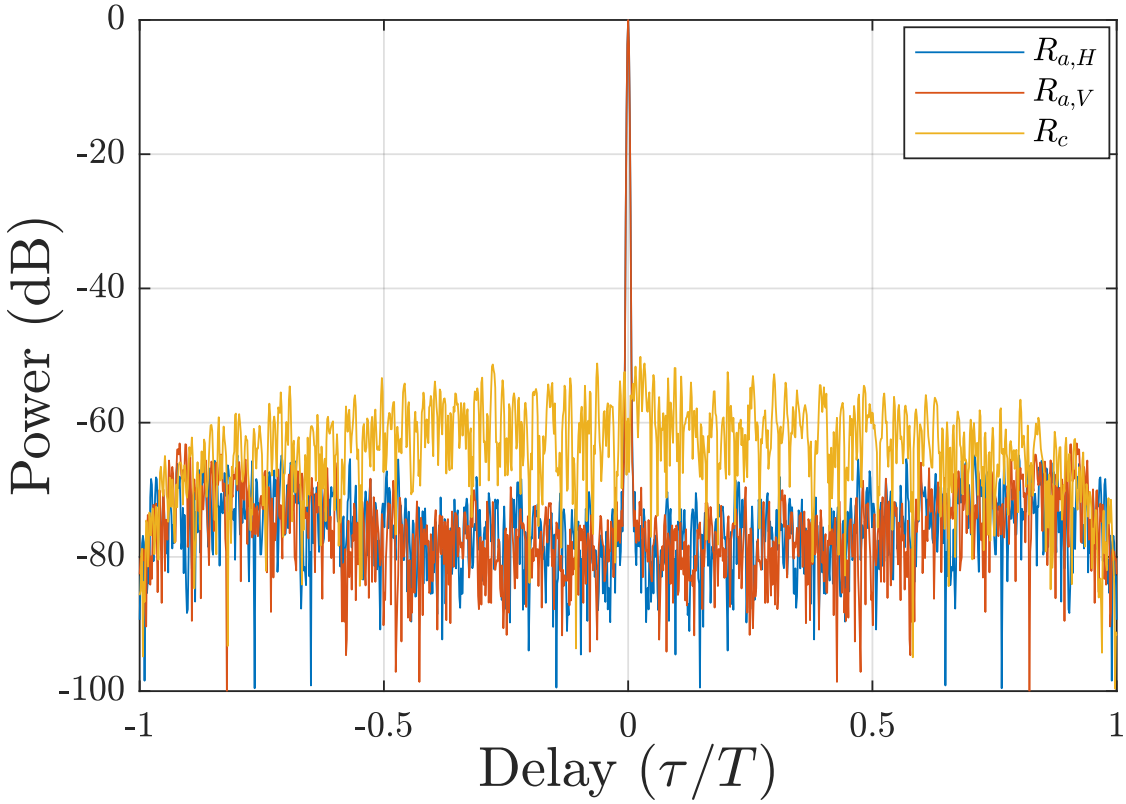

Figure 3.13: Simulated auto and cross-correlations for $L = 1800$ coherently integrated PRO-FM waveform pairs with $BT = 200$.

The RMS auto- and cross-correlations represent the average responses one might expect from a single received pulse. The PRO-FM RMS correlations display significantly better performance than the simultaneous LFM RMS correlations. The narrow peaks of the PRO-FM RMS autocorrelations for channels H and V are shown in Figure 3.14 with much better delay (range) sidelobe suppression than the RMS correlations for LFM. Compared to the -13 dB down sidelobes of the simultaneous LFM emission scheme, the approximately -37 dB sidelobe suppression on a per-pulse basis is far superior. The cross-correlation performance of the PRO-FM waveform is also better

than the LFMs presented in earlier sections. Note, however, that the cross-correlation between two independent PRO-FM waveforms offers the same performance relatively close to $\tau = 0$ (or zero delay) on a per-pulse basis but improves with increasing τ. The cross-correlation continues to improve as a function of L given sufficient coherent integration unlike the LFM cross-correlation which does not change. These performance increases (described in more detail in section 2.10) arise due to the random nature of the PRO-FM auto/cross-correlation sidelobes which promotes destructive combining when coherently averaged across many pulses.

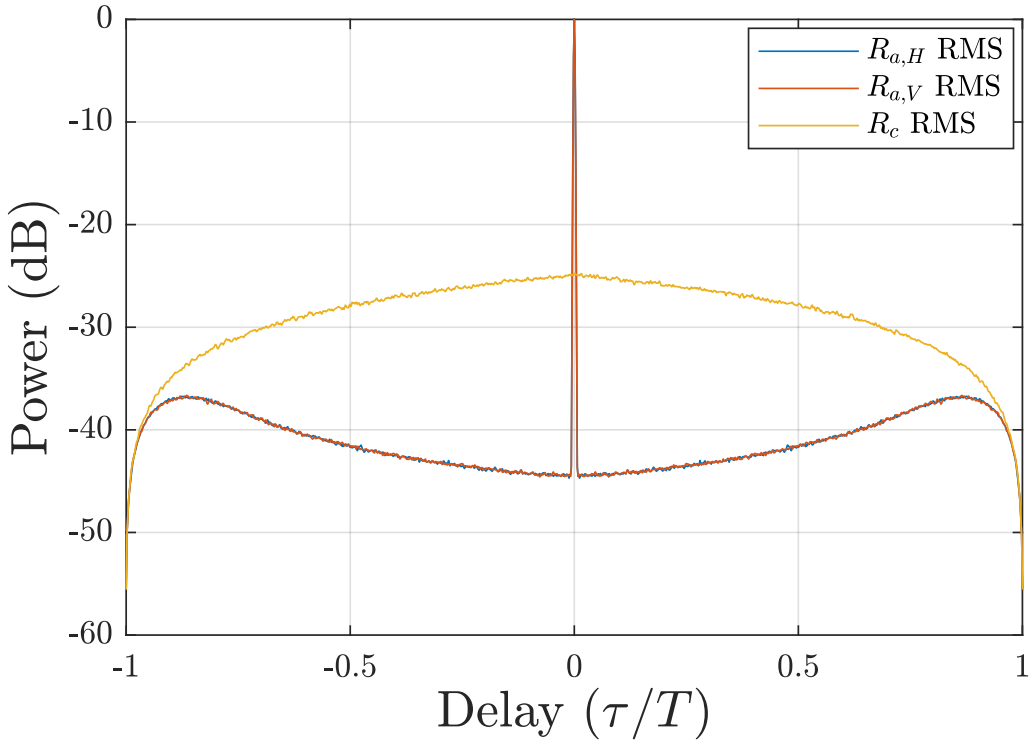

Figure 3.14: Simulated RMS auto and cross-correlations for $L = 1800$ coherently integrated PRO-FM waveform pairs with $BT = 200$.

Next, consider Figure 3.15 which depicts the spectra of the H and V channel PRO-FM waveforms. The approximated Gaussian shape imposed during the spectrum optimization performed when generating these waveforms is apparent. Note that both waveforms occupy the same bandwidth and portion of the spectrum when simulated. While the Gaussian does provide good spectral containment the roll-off is slight and only manages about -40 dB at 1.5 times the bandwidth of the signal. The LFM spectra from Figure 3.9 offers much sharper roll-off and better containment.

The downside to the LFM, as explained earlier, is the similarity between the H and V channel waveforms being quite high and thus offering poor auto/cross-correlation performance.

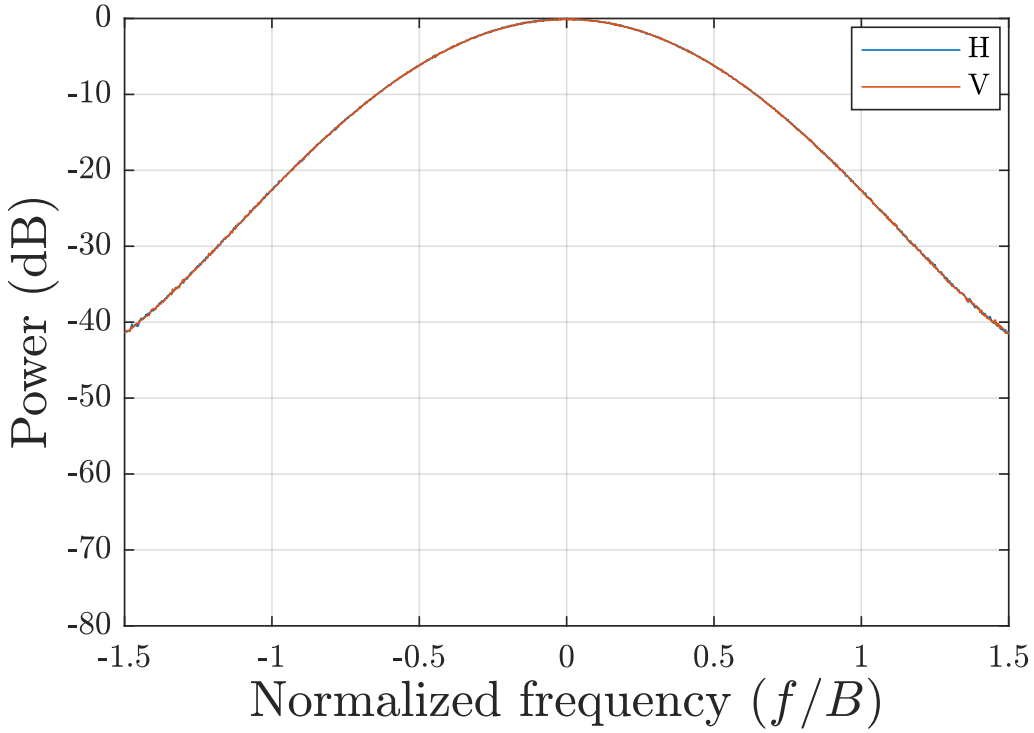

Figure 3.15: Simulated spectra of PRO-FM waveform pairs with $BT = 200$.

Next, consider the range-Doppler plots in Figure 3.16 after simulating the transmission and reception of $L = 1800$ PRO-FM pulse pairs. Notice that all five targets are displayed in each plot with good received SNR. The same zero-Doppler notch width is used in all three test cases (simultaneous LFM, interleaved LFM, and simultaneous PRO-FM) determined by the 7 significant principle values observed after performing the SVD of each test case *CPI*. Notice how there are no range sidelobe structures apparent around any of the targets. These sidelobes can be observed in previous range-Doppler plots, especially when observing target 1 in the HH plots for the two LFM test cases. This is due to the good autocorrelation performance after coherent integration of 1800 pulses (shown in Figure 3.13). Possessing lower sidelobes reduces potential range ambiguities caused by constructive/destructive combining of sidelobes of closely spaced targets when compared to LFM.

Simultaneous PRO-FM emissions provide a much better estimate of the cross-pol scattering

characteristics for each target compared to the previous two test cases. This is especially evident during comparisons to the simultaneous LFM test case. The suppressed cross-correlation response provides a good "clean" estimation of the cross-pol target scattering characteristics and lacks the seemingly infinite range sidelobes of the simultaneous LFM emission.

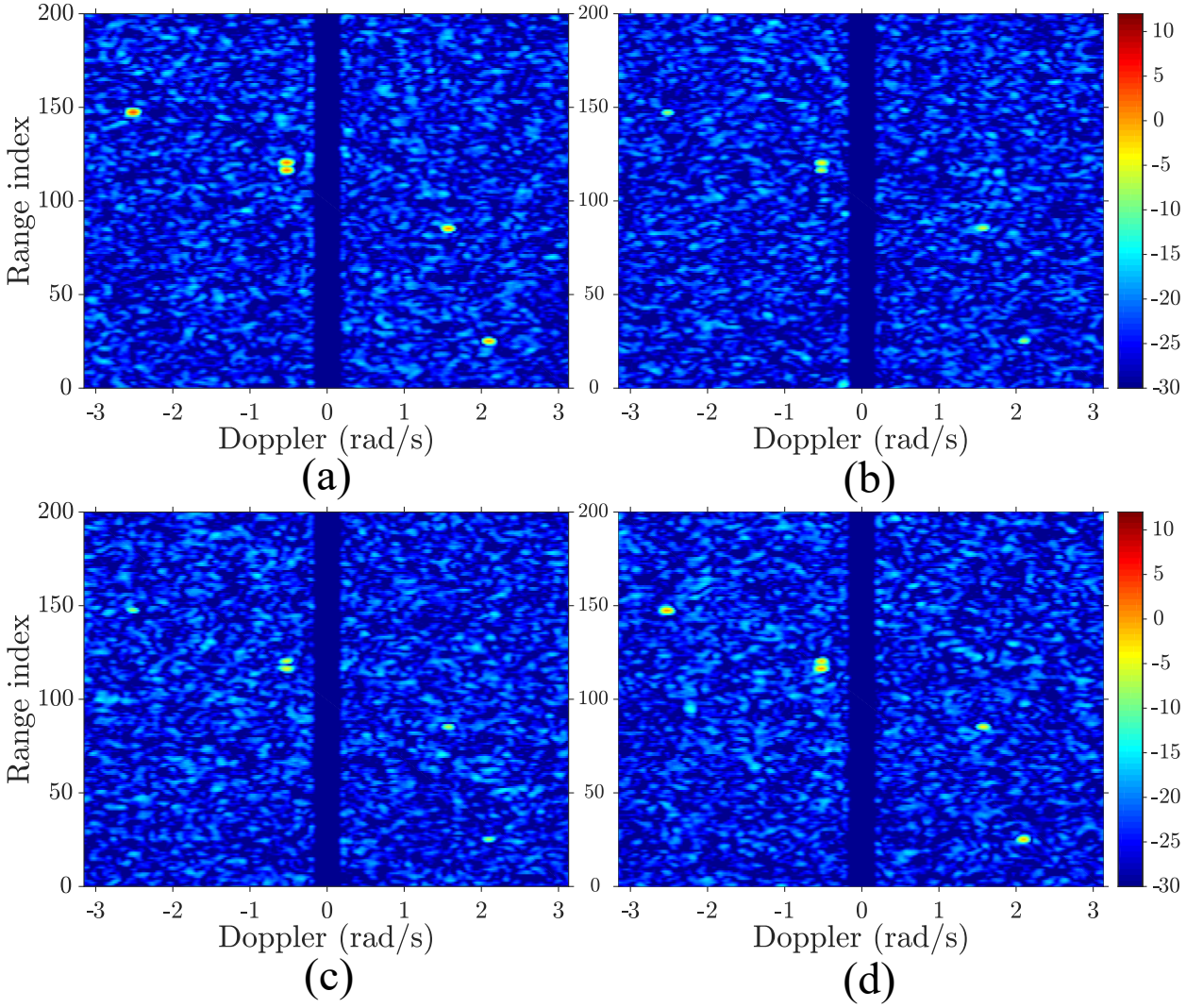

Figure 3.16: Simulated (a) HH, (b) HV, (c) VH, and (d) VV range-Doppler maps when transmitting simultaneous dual-pol PRO-FM waveform pairs with $BT = 200$.

Like in the previous sections, table 3.4 provides the estimated target characteristics after being distorted by the simulated transmission and receive processing. The average losses for the co-pol and cross-pol returns was about 7 dB. Notice that the phase of the cross-pol terms has less variance for this emisison scheme than the previous two test cases. The average losses for each channel are

slightly worse than the simultaneous LFM but markedly better than the interleaved LFM test cases.

Table 3.4: Estimated scattering matrices, location, and Doppler information for the five simulated targets from table 3.1 for simultaneous dual-pol PRO-FM.

Target Index	**Estimated Scattering Matrices**	**Location** (Range)	**Doppler** (rad/s)
Target 1	$\begin{bmatrix} 2.71e^{-j2.93} & -9.74e^{j0.88} \\ -8.07e^{j0.89} & -0.15e^{-j0.35} \end{bmatrix}$	147	$-\frac{4\pi}{5}$
Target 2	$\begin{bmatrix} 1.76e^{j0.47} & -3.49e^{-j0.95} \\ -4.42e^{-j0.74} & -2.49e^{j1.68} \end{bmatrix}$	120	$-\frac{\pi}{6}$
Target 3	$\begin{bmatrix} -0.05e^{-j2.35} & -6.10e^{-j0.68} \\ -6.66e^{-j0.98} & -7.05e^{-j1.69} \end{bmatrix}$	85	$\frac{\pi}{3}$
Target 4	$\begin{bmatrix} -0.01e^{j2.70} & -7.82e^{-j1.89} \\ -5.97e^{-j2.17} & -0.64e^{j2.00} \end{bmatrix}$	25	$\frac{2\pi}{3}$
Target 5	$\begin{bmatrix} 1.34^{j2.11} & -4.44e^{j0.56} \\ -4.77e^{j0.63} & -1.45e^{-j1.34} \end{bmatrix}$	116	$-\frac{\pi}{6}$

The simulated radar data shown above can only provide so much insight into how this implementation would function on real hardware. The next section presents open-air experimental results collected at the University of Kansas.

3.3 Experimental Results - Free Space Measurements

Utilizing the dual-polarized waveforms pairs discussed in previous sections, free-space measurements were collected from the roof of Nichols Hall on the University of Kansas West Campus. Shown in Figure 3.17 is the intersection at 23rd and Iowa streets at a straight-line range of approximately 1050 to 1250 meters. There are many different forms of scatterers contained within this scene including large buildings, a multitude of trees, and moving motor vehicles. The heavily cluster of buildings and trees presents a challenging environment due to many sources of multipath and clutter as well as internal clutter motion induced by branch/leaf movement caused by wind. The main focus is on the motor vehicles moving in the North- and Southbound lanes because they provide good sources of Doppler.

Figure 3.17: Aerial view generated using Google Earth depicting the roof of Nichols Hall and looking towards the 23rd and Iowa intersection.

3.3.1 Test Setup

Shown in Figure 3.18 is a block diagram depicting transmit and receive signal paths for the open air testing conducted on the roof of Nichols Hall and overlooking the 23rd St. and Iowa intersection in Lawrence, KS. Each chain (transmit and receive) utilized a separate offset horn-fed dish antenna [113], "KPPA-23-3GHZDPFHA" from KP Performance Antennas. These antennas were chosen due to the relatively high gain of 23.5 dBi and narrow 3-dB beamwidth of 12.3°. With a port-to-port isolation of at least 20 dB between the H/V ports and cross-polarization rejection of at least 25 dB these antennas will act a good front-end for the simultaneous dual-polarized emission tests. The operational frequency range for the parabolic reflectors is 3.3 to 3.8 GHz, offering up to 500 MHz of transmit bandwidth. The center frequency for each emission was chosen to be 3.55 GHz (directly in the middle of the frequency range supported by the antennas).

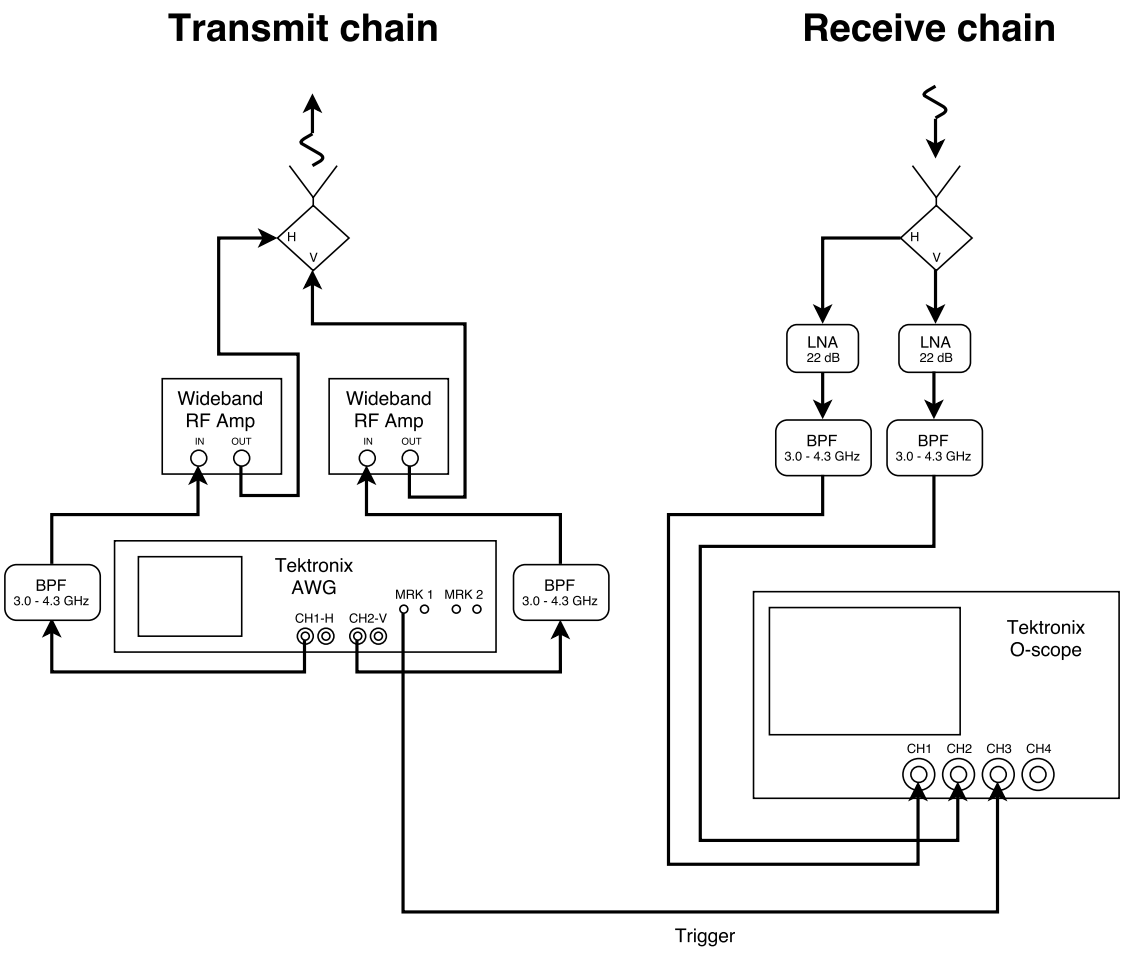

Figure 3.18: Test equipment setup for collection of free-space measurements.

The transmit chain is layed out as follows. The two independent transmit waveforms for H- and V-polarizations were generated using two channels of a Tektronix AWG70002 waveform generator [114] providing 10 bits of resolution per channel. A bandpass filter (BPF) with a passband spanning 3 to 4.3 GHz was then applied to each channel. Since the center of the intersection is located at a distance approximately 1100 m from the test setup, wideband power amplifiers were placed on both transmit signals to provide sufficient power on target for that range. The output of the amplifiers was then connected to the transmit parabolic reflector antenna. The receive path follows a similar structure. Echoes are collected with an identical parabolic reflector antenna that is offset spatially from the transmit antenna by approximately 2 meters (approximating a monostatic system for these ranges). Immediately following the receive antenna is an independent low-noise amplifier

(LNA) for each received polarization (H/V). Next a bandpass filter (the same model as applied on transmit) is added to the receive chain, one for H and one for V. The two received data channels were digitized and stored by a Tektronix DPO72304DX oscilloscope with 8 bits of resolution per channel. A picture of the hardware setup on the roof of Nichols Hall can bee seen in Figure 3.18.

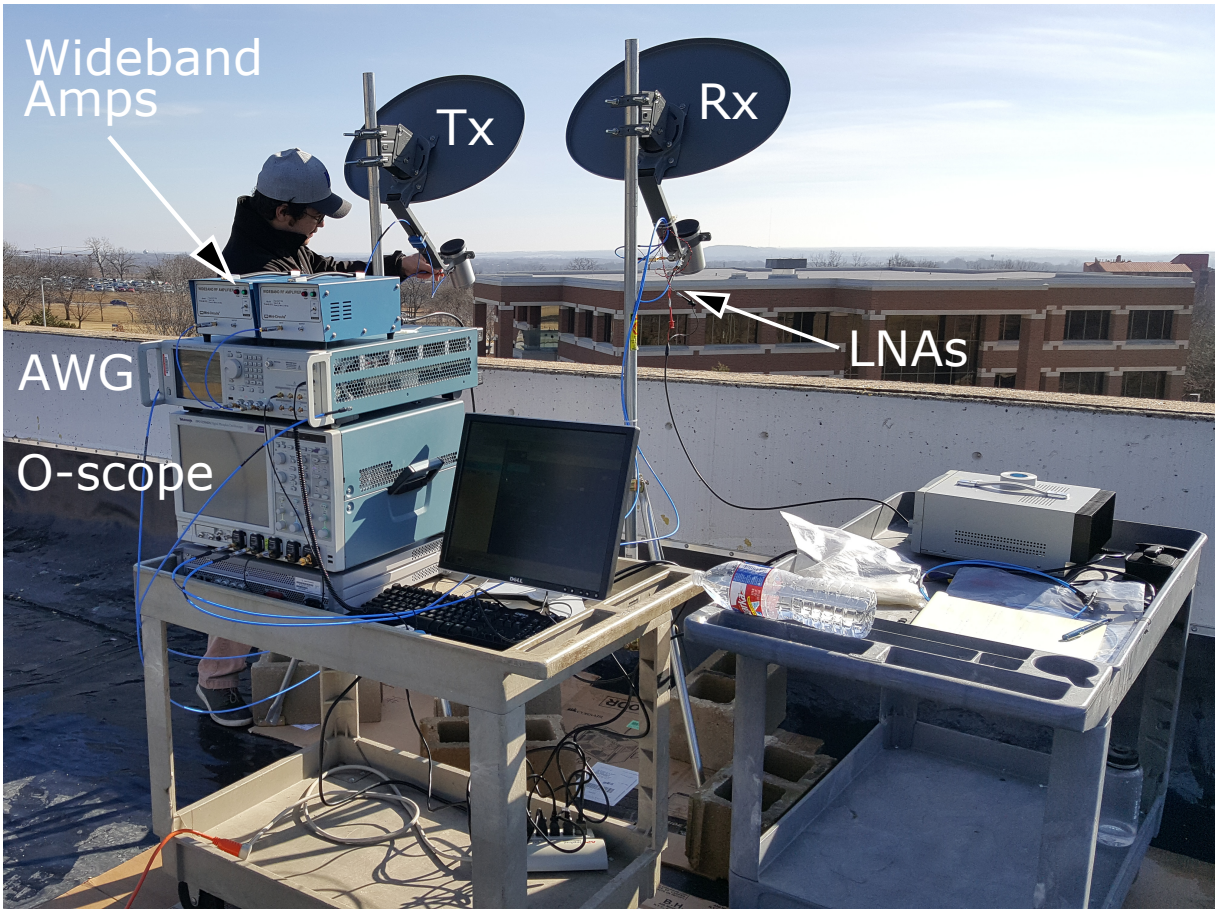

Figure 3.19: Hardware used in test location.

Similar to the simulations described in the previous section, three test cases will be evaluated. The first involving simultaneous emission of LFM waveforms from orthogonal polarizations, the second being a polarization interleaved LFM (or ping-pong LFM), and the last using two independently generated sets of PRO-FM waveforms to be emitted in a simultaneous dual-pol mode. Each test will utilize the test equipment described above to transmit waveforms and capture the receive echoes for the corresponding test case. The tests involving simultaneous emissions will

transmit $L = 1800$ waveform pairs [1] in a pulsed format with *PRF* of 50 kHz (equating a *CPI* of 20 μs), leading to a 5% duty cycle. The resulting *CPI* for the simultaneous tests is thus 36 ms. These tests will follow a transmit schedule resembling that of Figure 3.2. The interleaved LFM test requires a doubling of the *PRI* since only one polarization mode will be transmitted per *PRI*, similar to what is described in Figure 3.1. Thus, only $L_{\mathrm{H}} = L_{\mathrm{V}} = 900$ pulses for each polarization mode will be transmitted when operating in "ping-pong" mode. A comprehensive list of the system parameters used for each test case is provided in table 3.5. Note the slight differences between the simultaneous emissions and the interleaved LFM emission.

Table 3.5: Open-air test characteristics for simultaneous dual-pol LFM, interleaved dual-pol LFM, and simultaneous dual-pol PRO-FM.

Parameters	**Simultaneous LFM**	**Interleaved LFM**	**Simultaneous PRO-FM**
Center frequency (f_{c})	3.55 GHz	3.55 GHz	3.55 GHz
Bandwidth (B)	200 MHz	200 MHz	200 MHz
Pulsewidth (T_{p})	1 μs	1 μs	1 μs
PRF	50 kHz	25 kHz	50 kHz
Total pulses (L)	1800	900 (each)	1800
CPI	36 ms	36 ms	36 ms
Pre-summing	18	9	18
Unambiguous velocity (v_{max})	$\pm$58.69 m/s	$\pm$58.69 m/s	$\pm$58.69 m/s
Velocity resolution (Δ_v)	1.17 m/s	1.17 m/s	1.17 m/s
Tx sampling frequency ($f_{\mathrm{s}}^{\mathrm{Tx}}$)	10 GHz	10 GHz	10 GHz
Rx sampling frequency ($f_{\mathrm{s}}^{\mathrm{Rx}}$)	3.125 GHz	3.125 GHz	3.125 GHz
Bb proc. sampling ($f_{\mathrm{s}}^{\mathrm{bb}}$)	400 MHz	400 MHz	400 MHz

[1] Exactly 1800 waveforms may seem like a contrived number but due to data collection constraints that was the maximum number of pulses that our scope could handle. If you refer back to [112] where the original dual-pol PRO-FM work was documented, we used 5000 pulses. That data was collected using a scope with more on-board memory. The scope used in the revised tests had less memory and required the use of fast-framing to capture meaningful amounts of data.

3.3.2 Receive Processing

Both receive channels for all cases are processed using basic Doppler processing techniques that follow this progression (unless otherwise noted). The received echoes are converted from propagating EM waves to line voltages by the receive parabolic reflector antenna. These signals are then amplified independently by two identical LNAs and subsequently bandpass filtered. The filtered H and V signals are then captured by an oscilloscope via fast-framing. Fast-framing forgoes traditional receiver sampling by recording only a portion of the total *PRI* corresponding to the range of interest. This is accomplished by using a marker channel connected from the AWG to the scope. The scope then waits for the marker to arrive to initiate data capture. While fast-framing does decrease the digital footprint of the collected data and increases the number of total pulses that can be saved, it also abandons the direct path. This could be considered good or bad depending on the tests being conducted. Fast-framing also provides inherent robustness to multi-path and multiple-time-around pulse effects by rejecting signals located at time-delays outside of the sampling window.

Once the received signals are collected they are transferred to a personal computer for processing. Each test scenario transmits $L = 1800$ waveform pairs and receives/saves 1800 frames for both polarizations. Each set of 1800 frames is first down-converted to baseband by mixing each frame as

$$y_{\text{bb}}^{[\text{H}]} = y_{\text{pb}}^{[\text{H}]} \exp\left(-j2\pi \frac{f_{\text{c}}}{f_{\text{s}}^{\text{Rx}}}\right) \tag{3.5a}$$

$$y_{\text{bb}}^{[\text{V}]} = y_{\text{pb}}^{[\text{V}]} \exp\left(-j2\pi \frac{f_{\text{c}}}{f_{\text{s}}^{\text{Rx}}}\right) \tag{3.5b}$$

where y_{pb} and y_{bb} represents one frame of the set of passband and baseband receive signals. Referring back to the system parameter list provided in table 3.5, notice that the receive sample rate is lower than the transmit center frequency. This mismatch in sampling rate was chosen to further increase the amount of frames collected over by reducing the number of samples within each frame. Even though the receiver could theoretically sample as low as $2B$ to maintain Nyquist sampling,

the receive sample rate of 3.125 GHz provides the lowest center frequency that avoids overlap of aliased images in adjacent Nyquist zones [115]. The two orthogonally polarized baseband signals are then resampled to Nyquist ($2B$) at $f_s^{bb} = 400$ MHz. This reduces the length of each receive signal and makes further processing faster.

The matched filters used to range compress the receive signals were generated from loopback data collection. Loopback experimentation simulates transmission and reception of the waveform pairs without transmitting in free-space. A typical loopback setup utilizes every piece of the transmit and receive signal chain except the antennas. Instead, H and V feed channels are connected directly to the receive H and V channels, isolated by only attenuators to avoid damaging expensive test equipment. Filtering with waveforms distorted by loopback transmission incorporates hardware peculiarities, nonlinearities, and other effects into the matched filter step. This allows for a characterization of the transmission hardware (barring the antennas) to be filtered out of the open-air receive data. Since there are four total polarization responses (two co-pol and two cross-pol) to be determined, four filters are thus required.

Each filter is created by transmitting the L H and V polarized waveforms on two independent channels simultaneously and receiving first on the co-polarized channel and then on the cross-polarized channel. This process creates the four filters

$$\mathbf{w}_{HH} = \mathbf{s}_{HH} \tag{3.6a}$$

$$\mathbf{w}_{HV} = \mathbf{s}_{HV} \tag{3.6b}$$

$$\mathbf{w}_{VH} = \mathbf{s}_{VH} \tag{3.6c}$$

$$\mathbf{w}_{VV} = \mathbf{s}_{VV} \tag{3.6d}$$

where $\mathbf{s}^H$ is the conjugate transpose of the loopback waveforms for each test case and the corresponding co- and cross-polarized channels. The open-air receive data is then match filtered using

(3.6a-d) to estimate the range profiles corresponding to the ℓth pulse as

$$\mathbf{x}_{\mathrm{HH}} = \mathbf{w}_{\mathrm{HH}}^{H}\mathbf{y}_{\mathrm{H}} \tag{3.7a}$$

$$\mathbf{x}_{\mathrm{HV}} = \mathbf{w}_{\mathrm{HV}}^{H}\mathbf{y}_{\mathrm{H}} \tag{3.7b}$$

$$\mathbf{x}_{\mathrm{VH}} = \mathbf{w}_{\mathrm{VH}}^{H}\mathbf{y}_{\mathrm{V}} \tag{3.7c}$$

$$\mathbf{x}_{\mathrm{VV}} = \mathbf{w}_{\mathrm{VV}}^{H}\mathbf{y}_{\mathrm{V}} \tag{3.7d}$$

where $\mathbf{y}_{\mathrm{H}}$ and $\mathbf{y}_{\mathrm{V}}$ are the open-air receive horizontal and vertical channels respectively. Note that for PRO-FM there will be L total matched filters for H and V since each waveform is unique and does not repeat.

The moving scatterers in the illuminated scene are motor vehicles traveling at city speeds so the comparably high PRF can be reduced via pre-summing as described in [116]. Pre-summing involves summing a certain number of pulses prior to Doppler processing and after pulse compression, serving as a low-pass filter in the Doppler domain. Pre-summing is a well-known approach in synthetic aperture radar (SAR) to reduce data handling and storage requirements [116], but here it provides an additional benefit for these FM noise waveform pairs. It provides greater dimensionality for the incoherent combination of sidelobes when integrating these random FM waveforms. The the number of pulses pre-summed for each test case is listed in table 3.5.

Following pre-summing is the determination of the zero-Doppler projection and Doppler windowing of the data. The four range profiles are windowed, prior to Doppler compression, to suppress and/or ideally eliminate Doppler sidelobes. These sidelobes arise due to Doppler compression via the DFT in the slow-time domain, explained in more detail in section 2.7. The window type chosen was the Hanning window and its shape can be seen in Figure 2.8. The energy contained within the zero-Doppler clutter is often much higher than that of the scatterers for a ground-looking stationary platformed radar system. Because of this targets possessing low relative power can be missed. A zero-Doppler projection is formulated and applied to the four range profiles as described in section 2.7.1. Note the Doppler notch is applied after windowing and before Doppler compres-

sion. The four range profiles are then Doppler compressed by taking the DFT across the slow-time dimension to compress the Doppler information into a single range bin.

The results presented in this and the following sections are of open-air experimental tests conducted at the University of Kansas on the roof of Nichols Hall. The targets of opportunity are located at a mean distance of approximately 1100 meters at the intersection of 23rd and Iowa streets. Test equipment was carried to the roof and assembled similar to Figure 3.19. Unlike the simulated results presented earlier it is impossible to know ground-truth with respect to the scattering characteristics of an urban environment rich with clutter so the focus of these tests will be presenting and comparing different dual-pol LFM emission styles with a simultaneous dual-pol PRO-FM scheme. The figures of merit lie in the ability to resolve closely spaced targets, suppression of range sidelobes, recovery and separability of co-and cross-pol terms, and whether or not the emission is coherent with respect to both polarizations.

The proceeding sections detail three experimental test cases that illustrate dual-pol radar performance characteristics operating in simultaneous and pulse-interleaved modes. A comparison and more detailed observations are offered in section 3.4.

3.3.3 Simultaneous LFM

The first test case involves transmitting two LFM waveforms simultaneously on orthogonal polarizations H and V using the equipment shown and described in section 3.3.1. To provide some variation in the emissions an upchirp will be used for H and a downchirp for V. Each waveform was generated at baseband using equation 2.11 with amplitude A equal to unity, $B = 200$ MHz, and $T_\mathrm{p} = 1\ \mu$s. The H and V channel baseband waveforms are then up-converted to center frequency $f_\mathrm{c} = 3.55$ GHz by

$$s^{[\mathrm{H}]}_{\mathrm{LFM,pb}}(t) = s^{[\mathrm{H}]}_{\mathrm{LFM}}(t)\ \exp\left(j2\pi\frac{f_\mathrm{c}}{f_\mathrm{s}}\right) \tag{3.8a}$$

$$s^{[\mathrm{V}]}_{\mathrm{LFM,pb}}(t) = s^{[\mathrm{V}]}_{\mathrm{LFM}}(t)\ \exp\left(j2\pi\frac{f_\mathrm{c}}{f_\mathrm{s}}\right) \tag{3.8b}$$

where $f_s^{Tx} = 10$ GHz and is the transmit sampling frequency. The waveforms are then significantly up-sampled to emulate a continuous emission. Since the up-conversion and transmission process is the same for each test case it will only be explained in detail in this section. Refer to this description for each case. Dead-time in the form of zero-padding is added at the end of each LFM to create the appropriate *PRI* and 5% duty cycle. Next the waveforms are loaded onto two separate channels of the Tektronix AWG to prepare for transmission.

Since the same waveform pair will be used for all 1800 pulses the AWG must be programmed to repeat the emission sequence the desired number of times. A marker waveform is then created to trigger the fast-framing function of the oscilloscope acting as a receiver. Finally, all $L = 1800$ LFM pairs are transmitted simultaneously shortly after the traffic light of the north/southbound lanes turns green. The received echoes are captured by the Tektronix oscilloscope and then transferred to a computer capable of processing such returns. The processing of the dual-polarized received signals is described in detail in the preceding section. Note that the pre-summing factor for this case is 18.

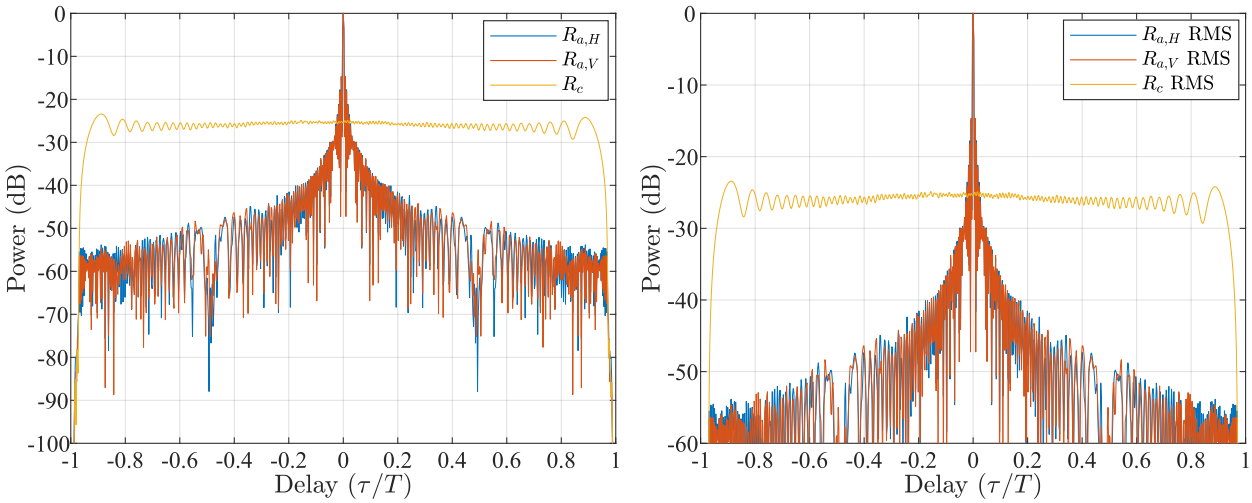

Figure 3.20: Auto and cross-correlations for 1800 simultaneously transmitted LFM pulse pairs after coherent integration (a) and RMS correlations (b).

The auto and cross-correlations for the simultaneous LFM test case are presented in Figure 3.20. These plots were generated from loopback captures of the waveforms that were used to match

filter the target returns. As expected the mainlobe of the autocorrelation is narrow for both H and V waveforms with the first (and highest) sidelobe appearing at approximately -13 dB down from the mainlobe. Note that the power is normalized to zero in both Figure 3.20(a) and (b) to better illustrate waveform characteristics. The cross-correlation between H and V appears relatively flat and at around -25 dB as expected. The RMS auto and cross-correlations appear very similar to the correlations post coherent integration just as in Figure 3.8. The waveform characteristics displayed by the loopback-collected waveforms is very similar to the waveform analysis conducted on the simulated waveforms in section 3.2.2, as expected. The distortions imposed by the hardware used to transmit and collected the waveforms is minimal.

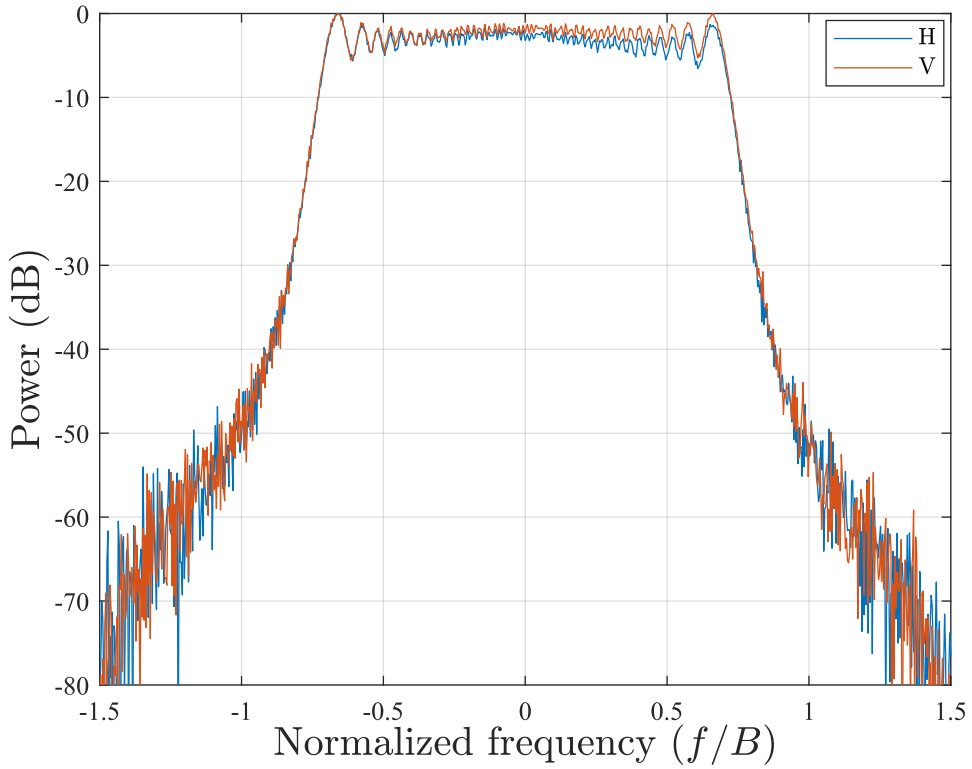

Figure 3.21: Spectra of simultaneously transmitted up/down-chirped LFMs after coherent integration and collected via loopback measurements.

Figure 3.21 depicts the spectra of the H and V channel LFM waveforms. These waveforms were collected via loopback measurements. Notice that the H and V polarized waveforms occupy the same bandwidth and maintain the same overall shape. The observable distortions caused by hardware are negligible when comparing the loopback captured waveforms with the simulated

wavefrom spectra in Figure 3.9.

Consider the range-Doppler maps presented in Figure 3.22 depicting the co-polarized (HH and VV) and cross-polarized (HV and VH) responses. First focusing on the responses with respect to co-polarized returns it is apparent that the simultaneous LFM emission sees multiple targets displaced in range and moving at different velocities. There also appears to be smearing in the range-domain. This smearing is the results of range sidelobes caused by matched filtering and coherently integrating numerous pulses possessing similar range sidelobe structures. The returns form co-polarized scatterers are readily apparent with multiple targets moving towards and away from the radar. The vertical co-pol range-Doppler map shown in Figure 3.22(d) appears to have a higher noise floor and a greater amount of range smearing. This could be caused by potentially higher vertically polarized zero-Doppler clutter returns from trees, tall buildings, etc.

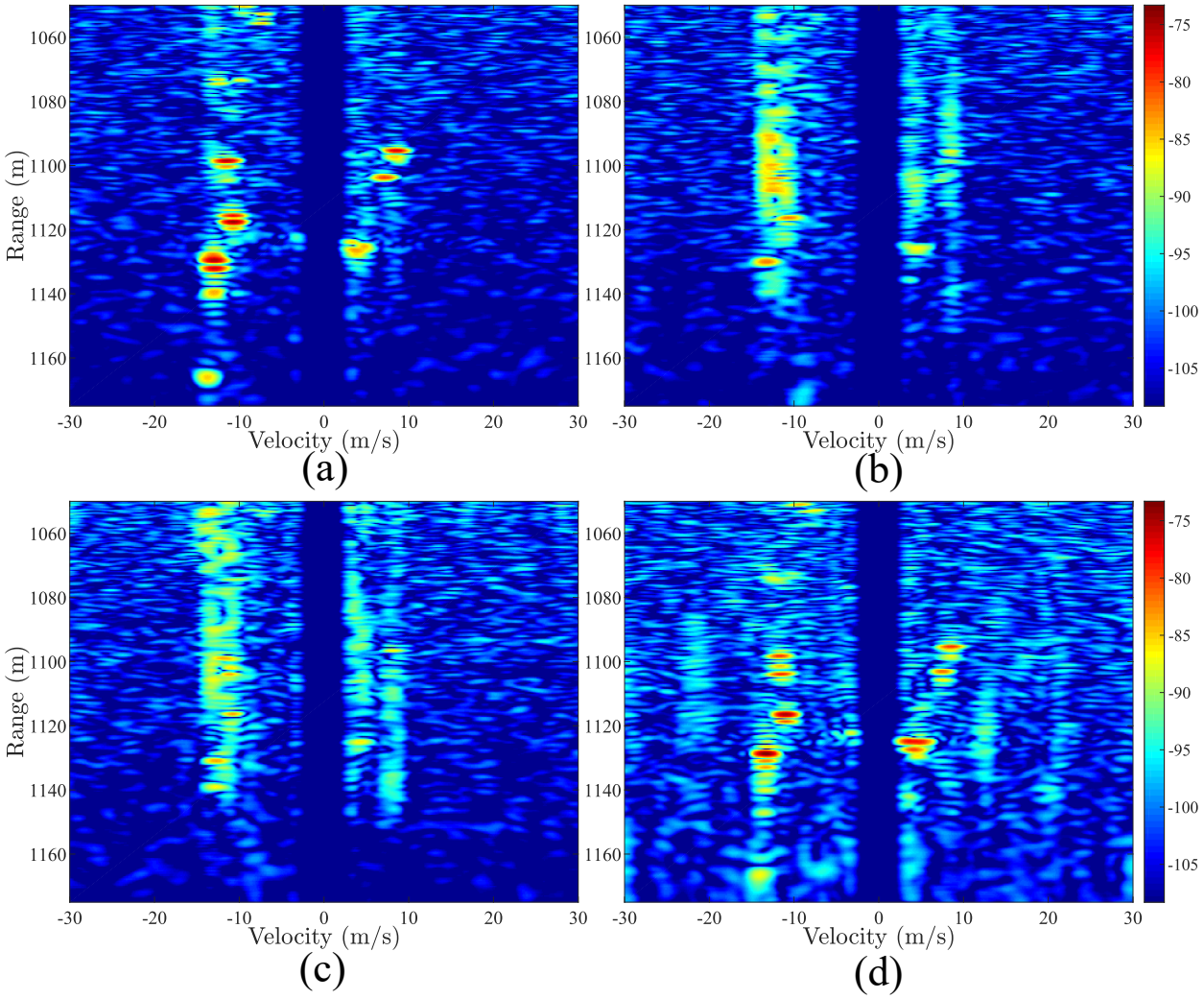

Figure 3.22: (a) HH, (b) HV, (c) VH, and (d) VV range-Doppler maps when transmitting simultaneous dual-pol LFM up/down-chirps and illuminating a busy intersection in Lawrence, KS.

Next, consider the cross-polarized (HV and VH) range-Doppler maps in Figures 3.22(b) and (c). An argument could be made that some targets are visible in the HV range-Doppler map with distinct peaks located around range 1228 meters through 1090 meters and Doppler -12 m/s. These peaks in the HV plot correspond to strong returns in the HH and VV plots. The range smearing in these plots is much worse due to the high levels of cross-correlation between the H and V polarized channels. High cross-correlation leads to poor polarization separability and inaccurate estimation of the cross-polarized portions of a target's scattering matrix. The simultaneous emission structure does benefit from all range-Doppler maps being coherent in regard to co- and cross-polarization.

Notice how large some of the return targets are in the co-pol plots. This could be due to range-Doppler coupling causing a spread in both dimensions.

3.3.4 Interleaved LFM

Next, consider an interleaved LFM emission structure using the same up- and down-chirped LFM waveforms from the previous section. The emission remains the same as described in section 3.3.3 up to where the dead-time is added to the passband waveforms. Instead the waveforms are zero-padded to create the emission schedule shown in Figure 3.1. The up-chirped LFM waveform followed by $(2PRI - T_{\mathrm{p}})$ zeros at a sampling rate of 10 GHz is placed on the H transmit channel. The V transmit channel is loaded with a down-chirped LFM sandwiched between (PRI) and $PRI - T_{\mathrm{p}}$ zeros. This zero-padding structure doubles the *PRI* of the individual channels to provide enough listening time for the receiver to collect returns from each pulse.

Receive processing for the interleaved LFM scheme varies slightly from what is discussed in section 3.3.2. The oscilloscope still collects 1800 frames per channel but for an interleaved transmit mode every other frame (even frames for the H channel and odd frames for the V channel) will possess only cross-pol information. However, the cross-pol responses will not be coherent from pulse to pulse due to lack of transmission simultaneity. The 1800 down-converted and resampled waveform pairs must be dissected into four sets determined by the odd and even indexed received pulses. The co-polarized received responses, $\mathbf{y}_{\mathrm{HH}}$ and $\mathbf{y}_{\mathrm{VV}}$, correspond to the odd numbered pulses from the H receive channel and the even numbered pulses from the V receive channel, respectively. Thus the total number of pulses is halved (as expected). The cross-pol responses, $\mathbf{y}_{\mathrm{HV}}$ and $\mathbf{y}_{\mathrm{VH}}$, are thus simply the even numbered H channel pulses and odd numbered V channel pulses, respectively. Range compression is thus modified from (3.7a-d) by replacing $\mathbf{y}_{\mathrm{H}}$ and $\mathbf{y}_{\mathrm{V}}$ with the corresponding co- and cross-pol pulse sets.

The correlations and spectra for the interleaved LFM test scenario remain the same as for the simultaneous LFM emisison scheme. Refer back to Figure 3.20 for autocorrelation characteristics and Figure 3.21 for spectral shape comparisons. Note, of course, that this emission is not simul-

taneous and thus the cross-correlation between the two waveforms does not provide any meaning. The returns observed in the cross-pol range-Doppler plots are entirely from cross-polarized responses and perhaps from the polarization purity of the test equipment.

Consider Figures 3.23(a)-(d) where the range-Doppler plots for the interleaved LFM scheme reside. One of the first observations one could make is that the large range sidelobes present in Figures 3.22(b) and (d) is missing. This is due to the interleaved pulse schedule imposing time separation between the waveforms instead of relying on the cross-correlation to separate cross-pol responses. The cross-pol returns also contain a level of ambiguity and uncertainty as to the purity of the received signals caused by possible leakage between the H and V channels within the hardware. This presents itself as a possible trade-off between interleaved and simultaneous dual-pol modes. The main trade-offs being "cleaner" co-pol responses with interleaved at the cost of coherence and determination of cross-pol returns.

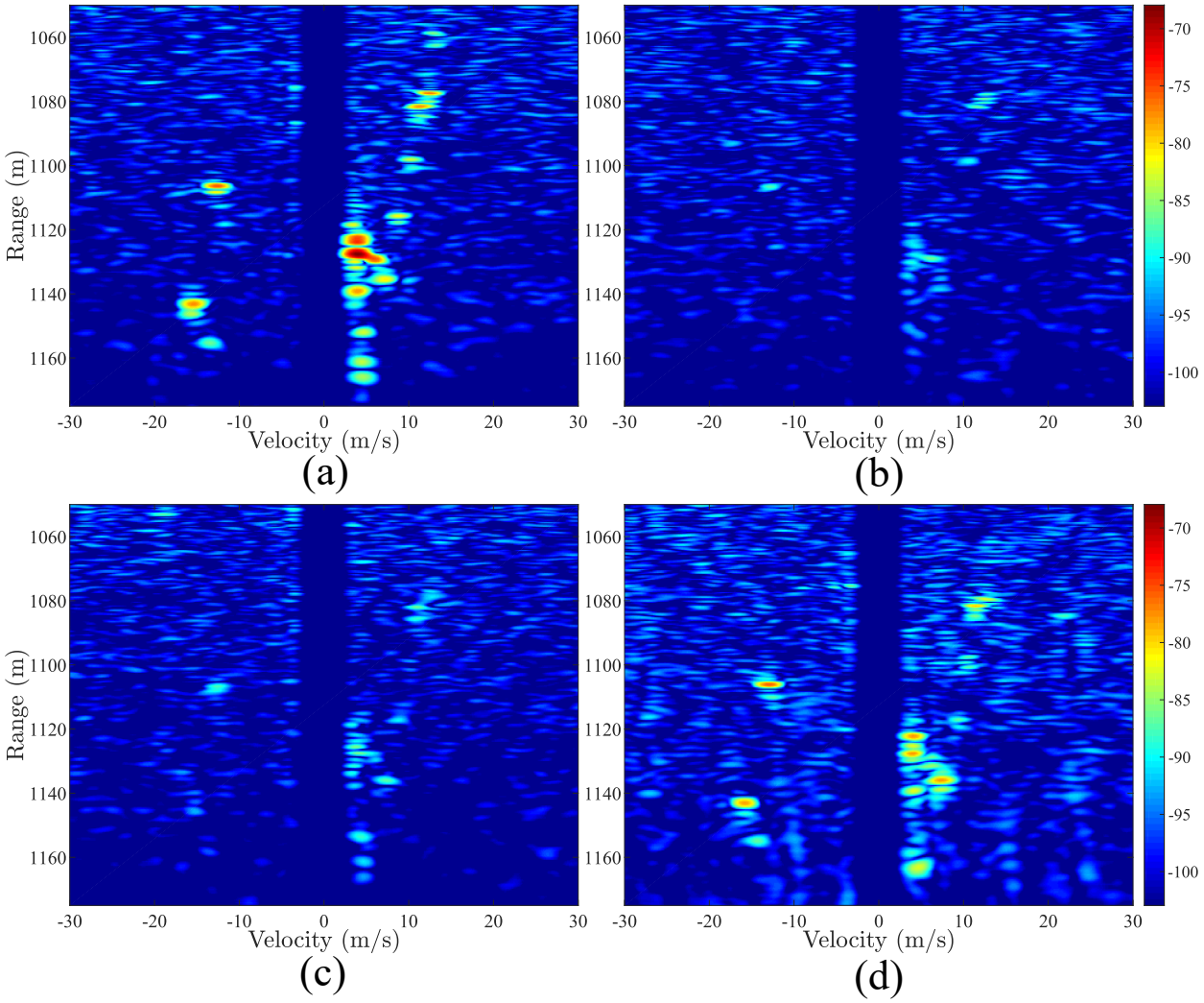

Figure 3.23: (a) HH, (b) HV, (c) VH, and (d) VV range-Doppler maps when transmitting LFM waveforms with interleaved orthogonally polarized pulses.

Theoretically there should only be noise and sidelobes from clutter in the cross-pol range-Doppler maps. However, upon close inspection there appears to be faint peaks that align with strong peaks from co-polarized targets. This phenomenon is most likely caused by leakage between the H and V receive channels in the antenna. Every RF device with multiple ports will exhibit some sort of relationship between each port. The parameter of interest here is the port-to-port isolation and cross-polarization rejection for the receive antenna. From the datasheet the cross-pol rejection offered by this antenna is listed as > 25 dB with V/H port isolation of > 20 dB [113]. By displaying a dynamic range of approximately 35 dB it is possible that the performance limitations of the test

equipment has been met and strong target returns are leaking between the two receive channels.

3.3.5 Simultaneous PRO-FM

The simultaneous dual-pol PRO-FM emission scheme is formulated almost identical to that of the simultaneous LFM from section 3.3.3. Each PRO-FM waveform pair is generated with $B_{3\text{dB}} = 200$ MHz at digital baseband using the generation scheme described in section 2.10. The waveforms are highly oversampled when generated to approximate a continuous emission. Each waveform pair is independently up-converted to a center frequency $F_{\text{c}} = 3.55$ GHz and then loaded onto the AWG for transmission. The key difference between the simultaneous LFM emission is that each of the 1800 waveforms for both polarization modes is different and never repeats. Because of this, receive processing requires the generation of 1800 different matched filters for each channel based upon loopback transmission, described in earlier sections.

First consider the correlations in Figure 3.24(a) and (b) where the auto/cross-correlations after coherent integration are shown. After coherent integration of 1800 pulses the autocorrelations for the H and V polarized PRO-FM waveforms has beaten the sidelobe level down to around -60 dB. The cross-correlation between the pulse pairs has also been reduced to peak at nearly -50 dB after coherent integration. This performance is to be expected based on previous PRO-FM experimental results [20, 45, 112]. The RMS auto and cross-correlations of the H and V channels display the expected performance on a per-pulse basis with autocorrelation sidelobes suppressed to around -35 dB and cross-correlation peaking at around -25 dB.

However, there are sidelobes that appear at approximately -42 dB in the autocorrelations for the PRO-FM waveforms. These peaks are believed to be a delayed version of the returns signal caused by a reflection at the input to the LNA connected to the input of the oscilloscope. The transmisison line connected between the receive antenna and the oscilloscope is 20 feet long with a LNA of the same make/model connected at both ends. This reflection travels a total length of 40 feet, corresponding to the delay between the peak of the autocorrelation and the peak of the reflected signal. Once the reflected signal has traversed back to the antenna-side LNA it is

then amplified and sent towards the oscilloscope. The amplification of the two LNAs in series is believed to have caused this. The sidelobe peaks that are believed to have been created by reflections in the receive chain between two LNA's are not present in the autocorrelations of the LFM pairs. This is due to the 42 dB separation between the mainlobe peak and the peaks from the reflections.

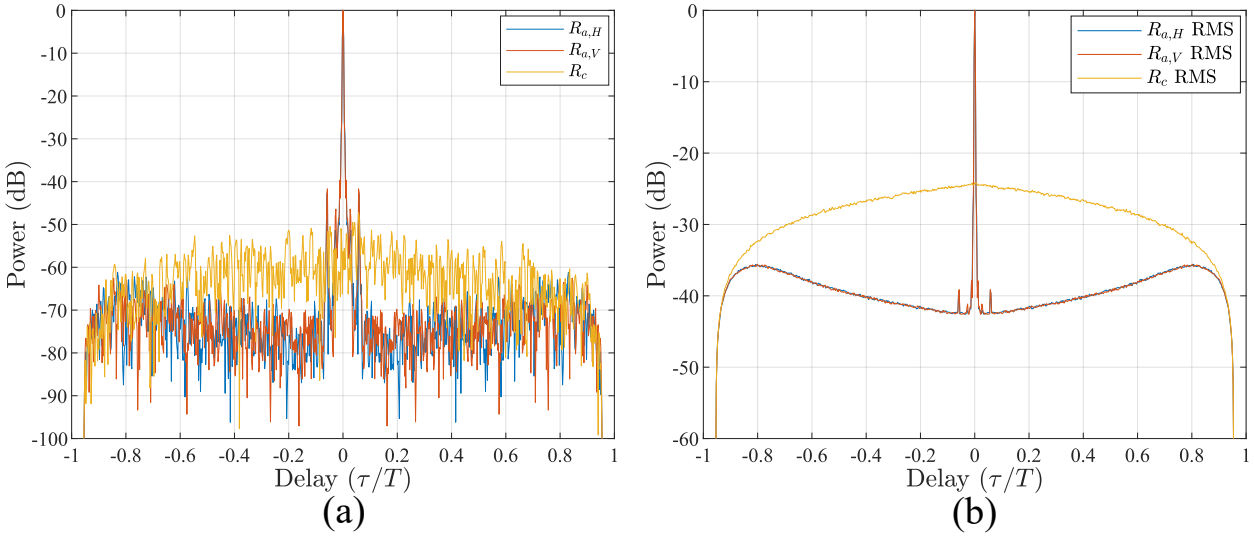

Figure 3.24: Auto and cross-correlations for 1800 simultaneously transmitted PRO-FM pulse pairs via loopback after coherent integration (a) and RMS correlations (b).

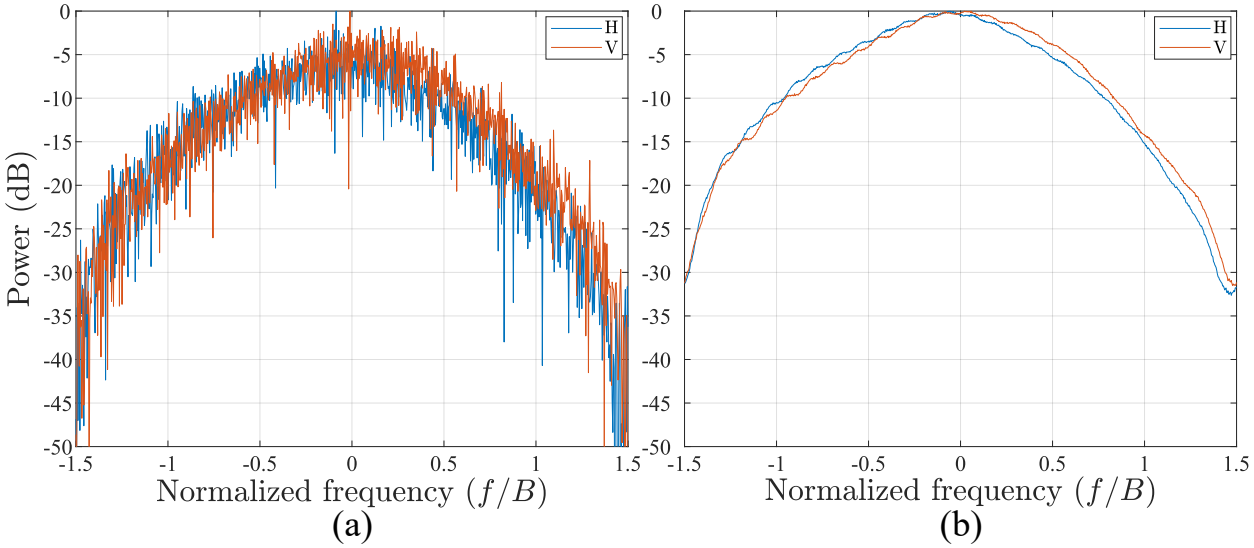

Figure 3.25: Spectra of simultaneously transmitted PRO-FM waveforms on polarizations H and V: (a) single waveform pair and (b) after coherent integration. Collected via loopback measurements.

Figure 3.25(a) and (b) depicts the spectra of the simultaneous PRO-FM emission on both orthogonally polarized channels for: (a) a single pulse and (b) coherent integration of 1800 waveform pairs. The Gaussian shape imposed during the PRO-FM optimization still retains its shape and good containment properties after loopback transmission. However, since this data was captured through loopback distortions have been introduced to the signals by hardware (as evident in the autocorrelations from Figures 3.24(a) and (b)). When comparing the spectra of the H and V channels after transmission to the simulated spectrum from Figure 2.17 the distortions become more apparent. A slight frequency up-shift in the V channel spectrum appears in figure 3.25(b). Small seemingly periodic ripples appear in both the H and V spectra for an unknown reason.

When observing the co-pol responses depicted in Figures 3.26(a)-(d) and comparing to the previous two transmission schemes many stark differences are apparent. Firstly, there is no smearing caused by range sidelobes due to pulse-to-pulse changes in sidelobe structure inherent to the PRO-FM waveform. The different sidelobes coherently integrate and lower as function of L as shown in Figure 3.24. The range resolution has also improved. Target returns appear much tighter in both Doppler and range. Note that a different scene was illuminated for each of the three test cases and direct side-by-side comparison of scatterers across different transmission modes is impossible. Notice that the noise floor appears to be higher with the PRO-FM test case. This is not noise however, but the random modulation of the range sidelobes inherent to the PRO-FM waveform.

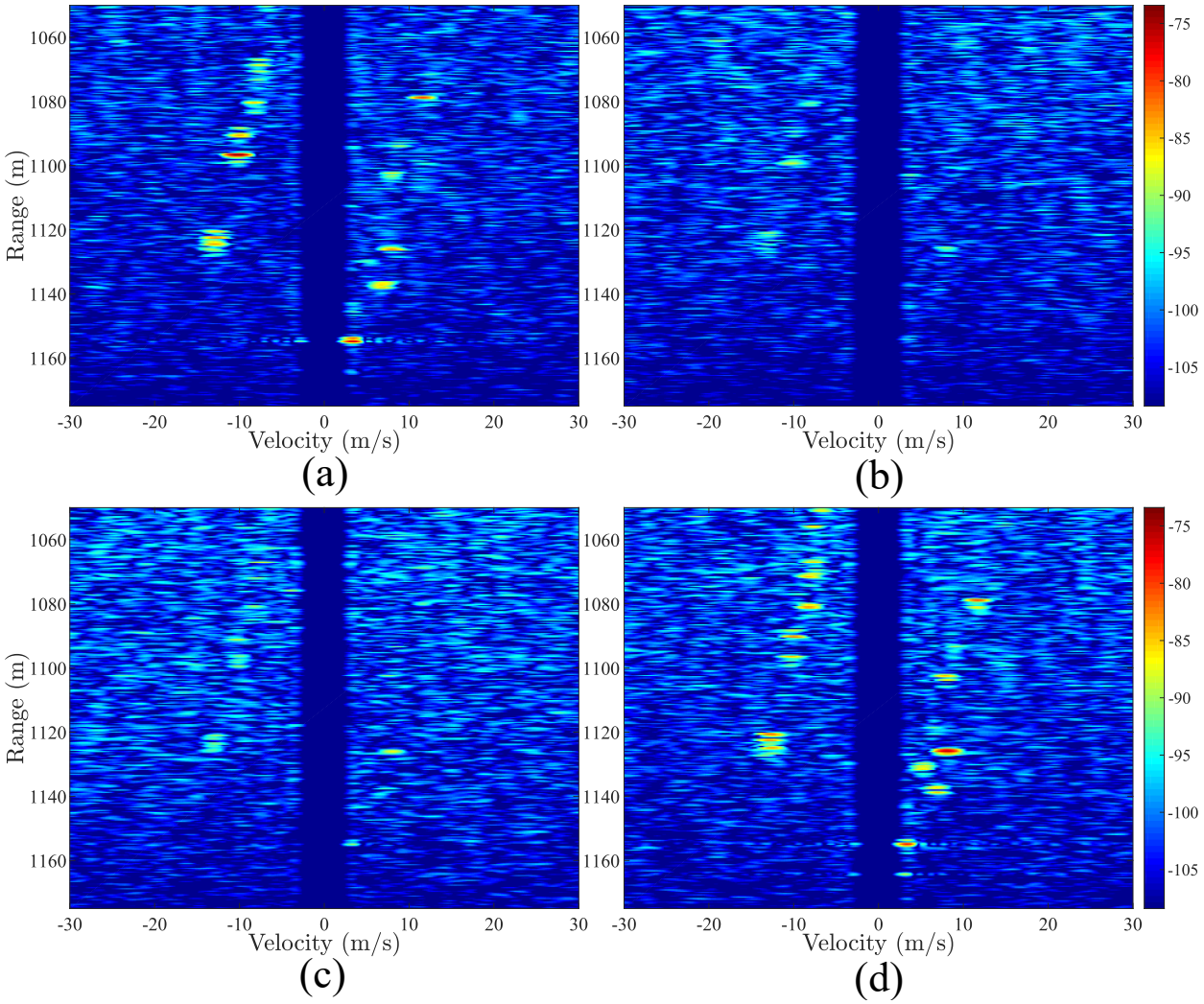

Figure 3.26: (a) HH, (b) HV, (c) VH, and (d) VV range-Doppler maps when transmitting simultaneous dual-pol PRO-FM waveforms.

The cross-pol responses for 1800 waveforms is lower than expected. A few small targets appear within the noise, however. The targets that do appear do not exhibit any range smearing due to good cross-correlation exhibited by the PRO-FM waveforms and provide a much better estimation of the cross-pol scattering characteristics of those targets. Compared to simultaneous LFM, simultaneous PRO-FM offers a "tidier" appearance with respect to range sidelobes and range resolution. The slightly worse HV and VH responses could be attributed to what is thought to be strong reflections occurring in the receive chain between two LNAs. Removing the Doppler windowing performed on the data would also improved receive SNR but would also introduce Doppler sidelobes (this is

the trade-space here).

3.4 Observations

This chapter has presented an emission scheme that simultaneously transmits independent, random, non-recurrent FM-noise waveforms on orthogonal polarizations H and V using the PRO-FM optimization scheme. This effectively implements a polarization diverse emission without the need for on-the-fly waveform design and expensive receive processing. Results from simulations and experimental open-air testing is described in earlier sections. The purpose of these simulations was to better characterize the emission scheme from [112] and set maximum performance criteria under ideal circumstances. From simulation the separability with respect to polarization purity was investigated with respect to independently generated pulse pairs. These simulations also provided a glance at the Doppler performance of this emission scheme. Open-air testing was conducted using test equipment to verify performance metrics observed in simulations.

The simultaneous dual-pol PRO-FM emission scheme was compared and contrasted to two baseline cases: simultaneous and interleaved dual-pol LFM. These LFM waveforms were identical from pulse-to-pulse (or every other pulse for the interleaved mode) and involved the transmission of a horizontally polarized up-chirp and a vertically polarized down-chirp. Note that each emission style was processed the same (or similar-enough with the interleaved LFM case). The simultaneous dual-pol emission scheme (test case 1) provided fully coherent co-/cross-pol responses and was the best in terms of average SNR. Unfortunately the LFM waveform suffers from high autocorrelation sidelobes and poor cross-correlation performance. This lead to high range sidelobes that fell off quickly in the co-pol returns and high cross-pol sidelobes enveloping almost all range in the cross-pol responses. These sidelobes can present challenges when targets are spaced closely together (like targets 2 and 5 were).

The interleaved dual-pol LFM emission scheme (test case 2) is similar to what is being implemented in certain fully polarimetric weather radars and others. Interleaved LFMs offer a more "pure" look at the cross-pol responses since the receiver is only seeing scattering from the cross-pol

targets. This eliminates the reliance on cross-correlation performance for HV and VH polarized responses. However, the received data is not be fully coherent due to the interleaved pulse structure. Full coherence requires simultaneous emission of both orthogonally polarized channels otherwise small phase discrepancies and different internal clutter motion from pulse-to-pulse will be injected into the responses. The biggest drawback to this emission scheme is the doubling of the *CPI* caused by a doubling of each channel's *PRI* to accomodate transmission and listening times for H and V. Each of the three test cases used the same *CPI* so the interleaved scheme suffered from only placing 900 pulses on target for each polarization mode which led to less coherent integration gain.

The simultaneous dual-pol PRO-FM emission (test case 3) exhibited similar performance in experimental testing as what was observed in simulation. Good auto- and cross-correlation performance carried over from simulation to experimental testing with the exception of what is believed to be strong reflections occurring in the receive chain. The receive SNR for co-/cross-pol responses was slightly worse than test case 1 but significantly better than test case 2. The PRO-FM waveform provides much better cross-correlation compared to test case 1 which eliminates the large range sidelobes observed in the cross-pol range-Doppler maps. This means that, while SNR may be slightly lower with PRO-FM, the estimation of scattering parameters for each target is more accurate. The strength of the returns from zero-Doppler clutter can significantly impact the ability for the dual-pol PRO-FM emission scheme to function properly. Extremely large clutter returns can swamp targets due to the range sidelobe modulation inherent to the random PRO-FM waveform. Experimental testing verified the validity of this approach. Transmitting and receiving on orthogonal polarizations allows for the complete polarimetric scattering matrix to be recreated. Dual-polarized PRO-FM could facilitate potential enhancements to target discrimination and possibly identification by better estimating scattering characteristics. This implementation also avoids the use of complex and computational expensive receive processing.

Chapter 4

Biomimetic Radar: Imitation of Fixational Eye Movements

Traditional phased array radars transmit waveforms possessing some form of modulation (whether amplitude, frequency, and/or phase), with a fixed phase offset relative to boresight during a single *PRI*. Should the transmission scheme involve beam steering, each subsequent pulse will typically have a new phase offset applied across the array, corresponding to a new look direction for the main beam. This method of beam steering allows the array to illuminate a swath the size of the null-to-null beamwidth and interrogate good information from approximately the 3-dB beamwidth during each pulse. One technique that is employed to widen the main beam, or to spoil the beam, is called beamspoiling. Beamspoiling invloves small random weights applied to each element in a random manner. This effectively reduces the directivity of the main beam and widens the main lobe providing broader beamwidths without physically changing any hardware. Beamspoiling imposes negative effects on the radar system like reduced SNR and lowered directivity (gain). What if the beam could be spread in a different manner?

Here, the waveform diverse array (WDA) [13, 14, 44, 117, 118] concept is expanded to combine FM-noise waveforms with an active multiple-input and multiple-output (MIMO) emission that will facilitate fast-time steering of the main beam. Simply put, the main beam location of the coherent MIMO emission will be modulated in fast-time, meaning intra-pulse beam steering. This emission is formulated to mimic the fixational eye movements (FEM) observed in mammals possessing fovea, or the portion of the eye in which visual acuity is the highest. The small micro-movements, called microsaccades, occur during long periods of fixation and are believed to improve visual acuity by enhancing contrast and aiding in the resolution of spatial ambiguities [37–39]. Better explained in Figure 4.1, the microsaccade motion involves a modulation of the fovea about the tar-

get or area of interest in a seemingly random manner. For instance, when staring into the distance, perhaps trying to identify an object, or even when taking a vision test as part of an eye examination (black letters on white paper) the eye will produce motions similar to the ones shown in Figure 4.1. These subconscious movements are the center of much debate in the bio-community but the consensus is that microsaccades improve vision.

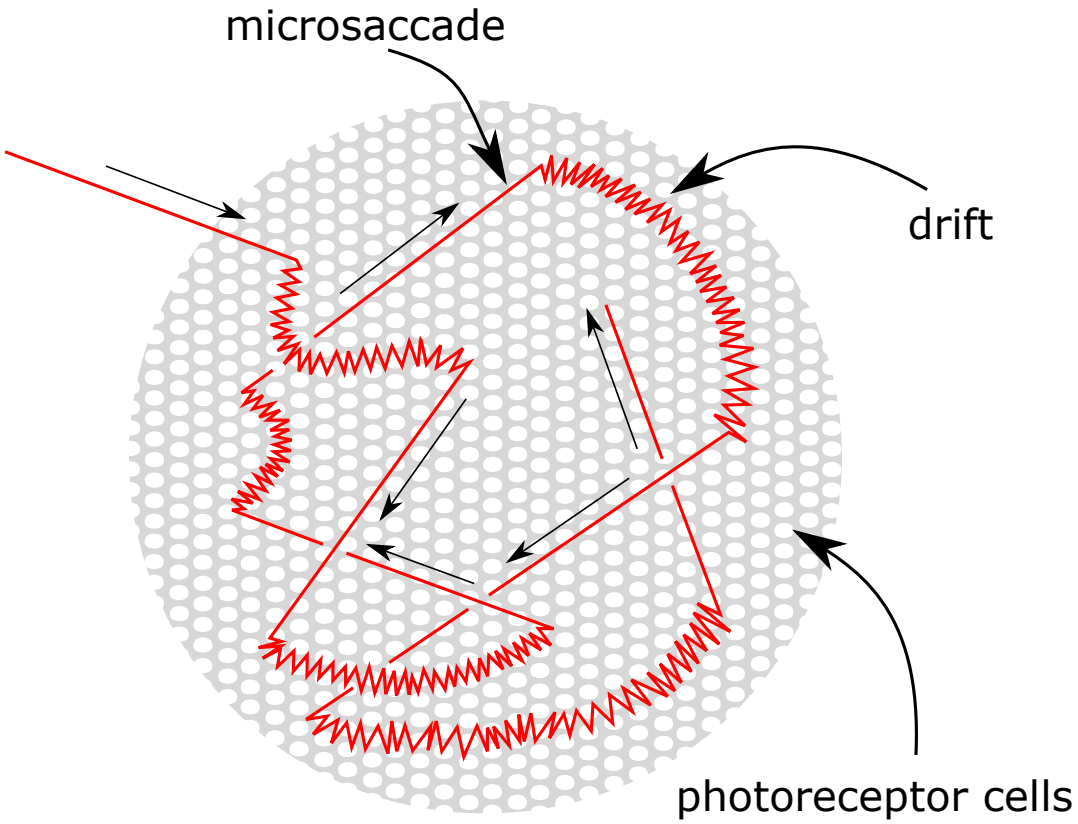

Figure 4.1: An example of eye movement during periods of fixation [1].

The use of the term MIMO may seem strange for this emission scheme. Significant portions of the MIMO literature focus on the design of the aggregate emission, whether designing orthogonal waveforms or some sort of optimization scheme to produce the desired radiation pattern [16] (and associated references). Because of this traditional MIMO lacks coherency between transmitting channels. Here, however, the use of multiple independent transmit channels is exploited to facilitate the fast-time dithering (or steering) of a *coherent* mainbeam. Each transmitting element of the

array (linear and planar arrays are focused here) is fed the same underlying waveform. Thus, the use of the word MIMO when describing this emission scheme may seem odd to some. However, the direction of the mainbeam is modulated during the pulse and thus providing the qualification to reside under the umbrella term: MIMO.

4.1 Motivation Behind Biomimetic Sensing

The technologies driving continued research on the topic of radar and sonar are advancing at a fast-pace, thus increasing capabilities once thought impossible [119]. From humble beginnings detecting ships in harbors [120] to mobile complex multifunction systems, the evolution of radar has come a long way. Similar to the technological evolution of radar systems, biological evolution has created active bio-sensors possessed by animals. These bio-systems are highly complex and provide accuracy and fidelity unparalleled by man-made counterparts [19]. These bio-sensors are used for myriad applications across a multitude of species that are analogous to application spaces of interest to radar engineers. These applications include but are not limited to tracking, navigation, target identification and classification, collision avoidance, and capture of prey. When considering the use of bio-sensors from a predator and prey point of view, fascinating likenesses to modern man-made systems arise. The evolution of these biological systems has spanned thousands or even millions of years and has thus been tweaked and optimized to meet a particular need and/or compensate for other inferior modes of sensing (e.g. eyesight of bats) [121].

Echo-locating bats make use of multiple complex emissions to to aid in the capture of prey. Bats are particularly interesting due to the high level of system integration contained within such a small platform. The emitted sonic pulses pulses are used to not only locate and capture prey, but to navigate complex environments with high levels of precision as well as identify what kind of prey was illuminated [122]. It has been discovered that bats transmit wideband and narrowband signals to perform multifunction sensing from an airborne moving platform in real time with great accuracy and efficiency [123] and even possess the ability to adaptively change the type of sonic pulse being sent out to meet certain environmental needs [124]. Because of this, using them as

a template to base man-made radar or sonar systems from should not come as a surprise. System design based off of biological sensors is motivated by exceptional performance observed in nature and are said to be "biomimetic". However, these biomimetic systems are still unable to compete with the "mediocre equipment" possessed by their biological counterparts despite employing highly complicated hardware and processing techniques [125].

While there is still much to learn from ever-evolving echo-locating mammals and insects, striving towards biomimetic system implementations for radar and sonar systems should not be overlooked. This chapter leverages certain aspects of vision to create a biomimetic radar emission scheme.

4.2 Spatially Modulated FM Noise Emissions

Typical radar systems transmit a modulated pulse in a single direction. When using an array capable of electronic steering this is accomplished by setting a fixed inter-element phase shift across the array, corresponding to the desired look direction. Barring this phase shift, the same underlying waveform is transmitted by each element. This same concept is used here but is extrapolated to incorporate the fast-time-varying spatial modulation element. This research aims to explore the applicability of random and non-repeating emissions to the waveform diverse array (WDA) by building off of previous research conducted in the area of spatial modulation. The WDA is an extrapolation of the frequency diverse array (FDA) [**?**, 13, 14, 117, 118] which describes an array that emits dissimilar waveforms on each radiating element.

The combination of spatial modulation with FM-noise waveforms creates the fixational eye movement radar (FEMR) emission scheme. The FEMR emission mimics the subconscious microsaccade movements performed by the eye through the emission of a coherent beam that dithers about a chosen center look direction as a function of fast-time. The waveform chosen for this emission scheme is the PRO-FM waveform due to the non-recurrent and spectral containment properties it provides. The PRO-FM waveform is designed to provide low range sidelobes through the use of a spectral shaping optimization. Different forms of spatial modulation are then employed

in conjunction with the PRO-FM waveform. The idea here is to combine a random FM waveform with a randomly steered emission to combine the range resolution improvements observed when transmitting the PRO-FM waveform and the spatial resolution enhancements from spatial modulation. This research begins with spatial modulation in a single spatial dimension to build a good foundation for the reader and is then extrapolated to a 2nd spatial dimension. The 2-D spatial modulation most closely mimics microsaccades and as such is the focus of this chapter.

4.2.1 FM-Noise Waveform Choice

While waveforms that better mimic noise in the truest sense of the word do exist, these implementations suffer from output power limitations due to amplitude modulation. The limitation on transmit power provides an application space confined to short-range radar systems due to high-power amplifiers requiring operation in the saturation region of their respect gain curves. Because of this, constant modulus signals are preferred to maintain good efficiency and limit amplifier switching during operation. The PRO-FM waveform offers a noise-like emission that provides constant amplitude signals to the transmit power amplifiers to facilitate its use in long-range applications.

The mathematical expressions and methods used to generate each PRO-FM waveform are explained in detail in section 2.10 but, for the sake of the reader, will be revisited here as well, albeit brief. The PRO-FM waveform is generated on a segment-by-segment basis, beginning with an independently generated randomized phase code for each segment. The phase codes are then passed through the PCFM architecture, outlined in section 2.9, to create the initial random waveform segments that will then be optimized. The spectral optimization is then completed by projecting between a desired spectral template $|G(f)|^2$ and time-domain envelope $u(t)$ in an alternating projections fashion. This process is shown in (2.51) and (2.52). Once the L segments possess a spectrum that sufficiently resembles the prescribed spectral template and a time-domain envelope that sufficiently resembles a rectangular window each successive segment is phase rotated as

$$s_\ell(t) = \exp\left(j\phi_{end,\ell-1}\right) s_{K,\ell}(t) \tag{4.1}$$

to avoid phase discontinuities. Here, $\phi_{end,\ell-1}$ is the ending phase of the previous segment. This step is not required when operating in a pulsed but for simplicity this work will use a continuous wave (CW) implementation. When operating in CW mode the transition between two adjacent waveforms must be continuous so as to avoid poor spectral containment caused by periodic abrupt and "explosive" spectral growth.

4.3 1-D Spatial Modulation

To introduce the concept of spatial modulation and the waveform diverse array (WDA) it is easiest to begin with a formulation in one spatial dimension. Doing so will allow the reader to develop the proper understanding before moving on to more complex instantiations, such as a second spatial dimension. Looking at spatial modulation in one dimension also allows for a simpler analysis of characteristics such as the time-varying beam pattern (TVBP), aggregate beam pattern (ABP), and spectral containment, among others.

For spatial modulation in the single dimension, consider a uniform linear array with elements equally spaced along the z-axis and with boresight being the y-axis. The uniform linear array (ULA) geometry used in this formulation of spatial modulation is a slightly modified version of the array shown section 2.8 and is depicted in 4.2. The inter-element spacing d and total number of elements M remains the same. The center look direction for each pulse (or waveform segment) is designated by ψ_{C} (instead of spherical coordinate θ) and is defined from $[-90^{\circ}, 90^{\circ}]$ with $\psi_{\mathrm{C}} = 0$ being boresight. Assuming that the waveforms being simulated adhere to the narrowband assumption as explained in section 2.8, the simulated ULA structure is as follows.

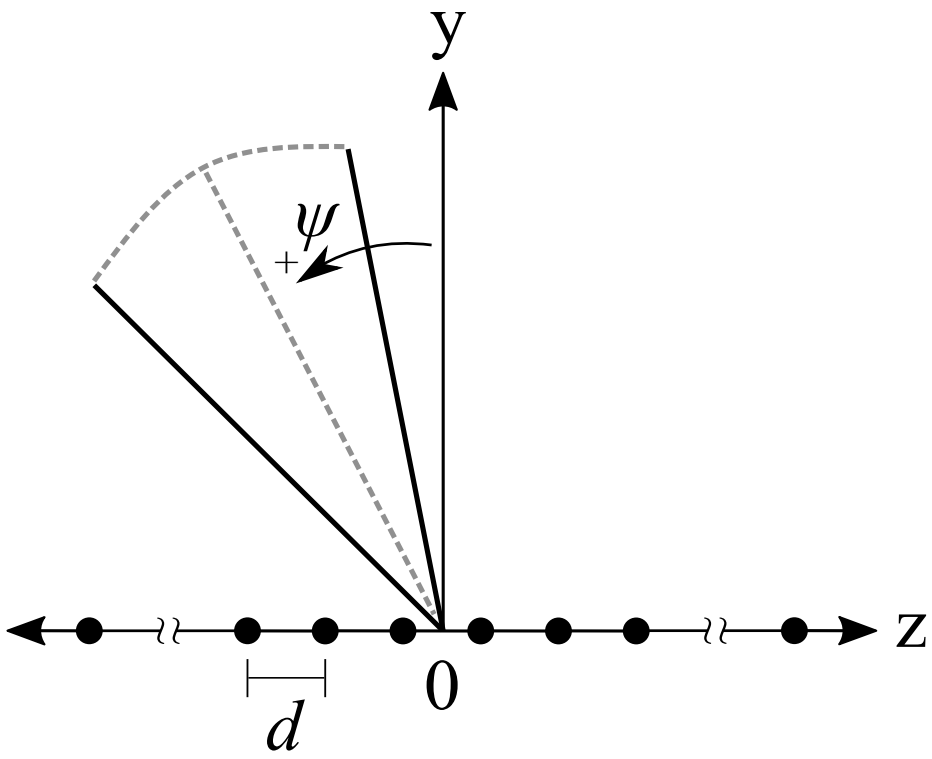

Figure 4.2: Uniform linear array geometry.

Building upon the formulation first developed in [1] the element indexing is handled as

$$m = \frac{-(M-1)}{2}, \frac{-(M-1)}{2}+1, \ldots, \frac{+(M-1)}{2}, \tag{4.2}$$

ensuring that the array centered at coordinate location $(0,0)$. Under the narrowband assumption, described in detail in section 2.8 of this report, the wavenumber for this array is

$$k = \frac{2\pi d}{\lambda}\sin(\psi). \tag{4.3}$$

The fast-time beam steering is controlled by generating a spatial offset sequence of length $N+1$, defined as $\{\Delta_0, \Delta_1, \ldots, \Delta_N\}$. This sequence is defined relative to current center look direction ψ_C and contains the spatial degree offsets for each fast-time sample of the steering code. During the nth code interval the coherent beam will steer from $(\psi_C + \Delta_{n-1})$ to the location described by $(\psi_C + \Delta_n)$. To mimic fixational eye movements the offsets are randomly generated within a prescribed bound

around the center look direction. To implement this direction change on an array the location in terms of degrees must be converted to phase. The electrical phase change corresponding to the nth sample is

$$\varepsilon_n = \frac{2\pi d}{\lambda}\Big(\sin(\psi_{\mathrm{C}}+\Delta_n) - \sin(\psi_{\mathrm{C}}+\Delta_{n-1})\Big) \tag{4.4}$$

for $n = 1,2,\ldots,N$, where the difference between adjacent values in the spatial offset sequence is calculated. The N total electrical phase changes are stored in the $N\times 1$ vector $\mathbf{x} = [\varepsilon_1,\varepsilon_2,\ldots,\varepsilon_N]$, which parameterizes the fast-time beam steering. Leveraging the PCFM architecture described in section 2.9 the continuous time spatial modulation sequence in terms of electrical angle is

$$b(t;\mathbf{x}) = \exp\left\{-j\left(\sum_{n=1}^{N}\varepsilon_n\int_0^t \mathrm{g}\big(\zeta-(n-1)T_p\big)d\zeta + \bar{\Delta}_0\right)\right\} \tag{4.5}$$

where the initial electrical angle is

$$\bar{\Delta}_0 = \frac{2\pi d}{\lambda}\sin\Big(\psi_C+\Delta_0\Big), \tag{4.6}$$

which ensures the signal remains continuous when switching to new center look directions on the proceeding segments. Thus, the emission from the mth antenna element of the ULA is thus

$$s_{m,\ell} = \frac{1}{\sqrt{T_{\mathrm{p}}}}s_\ell(t)b^m(t;\mathbf{x}) \tag{4.7}$$

for the ℓth PRO-FM waveform segment. From this formulation the baseband far-field emission as a function of time, t, and spatial angle, ψ, is defined as

$$g_\ell(t,\psi) = \frac{1}{M}\sum_m s_{m,\ell}e^{j(k(\psi)m)} \tag{4.8}$$

with associated aggregate beampattern (ABP)

$$B(\psi) = \frac{1}{TL}\sum_{\ell=1}^{L}\int_0^{T_{\mathrm{p}}}|g_\ell(t,\psi)|^2dt. \tag{4.9}$$

The far-field emission is calculated as the element-normalized summation of the M 1-D MIMO waveforms multiplied by a complex phaser containing the mth wavenumber. The ABP is found by integrating the time-varying beampattern (TVBP)

$$B_{\mathrm{TV}} = g(t,\psi)g^{*}(t,\psi) \tag{4.10}$$

over the pulsewidth T_{p}. Here, $(\bullet)^{*}$ denotes complex conjugation. The ABP of random spatially modulated emissions will be compared to a staring beam to observe the amount of main-beam spoilage. By observing the TVBP a better visual representation of fast-time random beam steering will be presented. The next section presents some 1-D random spatial modulation simulation results before moving on to the much more interesting 2-D random spatial modulation, actually simulating FEM produced by the human eye.

4.4 1-D Spatial Modulation Simulations

All simulation results provided in this section use the same underlying parameters. Shown in Figure 4.2 is the uniform linear array geometry used, with $M = 20$ elements centered at the origin when using the element indexing described in (4.2).

Three steering techniques will be evaluated and compared to compare the effects of random spatial modulation with previous work, consider the following steering scenarios. The first is a linear sweep, the next is the sinusoidal sweep, and the last is the randomized beam steering, which mimics FEM in one dimension. The linear steering pattern sweeps incrementally from $-\Delta_{\max}$ to $+\Delta_{\max}$. The sinusoidal pattern traces a cosine shaped path over the same range. The random steering pattern is generated by sampling a uniform distribution defined over the interval $\pm\Delta_{\max}$ with a mean value of ψ_{C}. A single PRO-FM waveform segment with $BT = 200$ was generated and emitted using the three steering techniques described above. The spatial modulation code is generated on a segment-wise basis, similar to the PRO-FM waveform, and is defined relative to the segment's center-look direction ψ_{C}. The range over which the fast-time beam steering is conducted

is determined by $\Delta_{\max}$.

The TVBP offers an intuitive look into how the fast-time beam steering is conducted. Note that the vertical axis is in (normalized) fast-time samples, meaning that the instantaneous beam pattern for that sample is represented by the horizontal cut from the selected figure. Also note that since the vertical axis is fast-time, and not range, the main beam of the emission is not bending or contorting out in space. Figure 4.3 displays the TVBP for the three steering patterns discussed, where Figure 4.3a is linear, Figure 4.3b sinusoidal, and Figure 4.3c random. Each steering pattern was defined with center look direction $\psi_C = 5^\circ$ and $\pm\Delta_{\max} = 5^\circ$. Inspecting the TVBPs shown in Figure 4.3 allows the reader to observe the chaotic random beam steering and contrast it with the more structured steering techniques. This random structure closely resembles that of the microsaccades shown in Figure 4.1. One important thing to note is that spectral containment performance degrades, especially for the random spatial modulation case, when steering (or dithering) across intervals larger than 10-25 degrees. Next, consider the impact each beam steering technique has on the aggregate beampattern, as shown in Figure 4.4. The spreading of the mainbeam and associated loss in emitted power for the three steering techniques relates directly to the width of the fast-time beam steering swath, Δ. In this particular case the random steering exhibits the most narrow main beam and the largest peak power. Note also that the peaks are normalized to show the loss in power relative to each steering technique. The broadening of the linear and half-wave sinusoid steering techniques equates less power on target, especially when observing the "dip" in the center of the half-wave ABP.

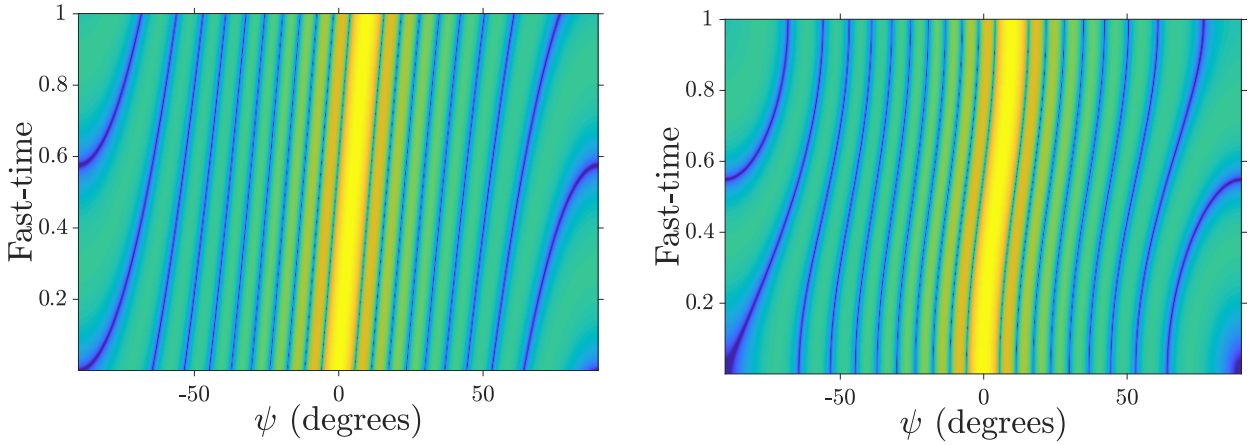

(a) Linear.

(b) Sinusoidal.

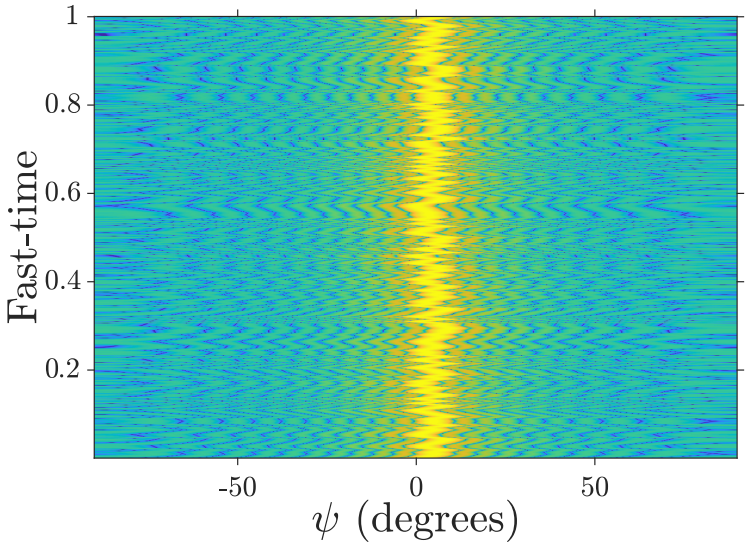

(c) Randomized.

Figure 4.3: Comparison of time-varying beam patterns for linear (a), sinusoidal (b), and random (c) fast-time beam steering for center-look direction $\psi_C = 5°$.

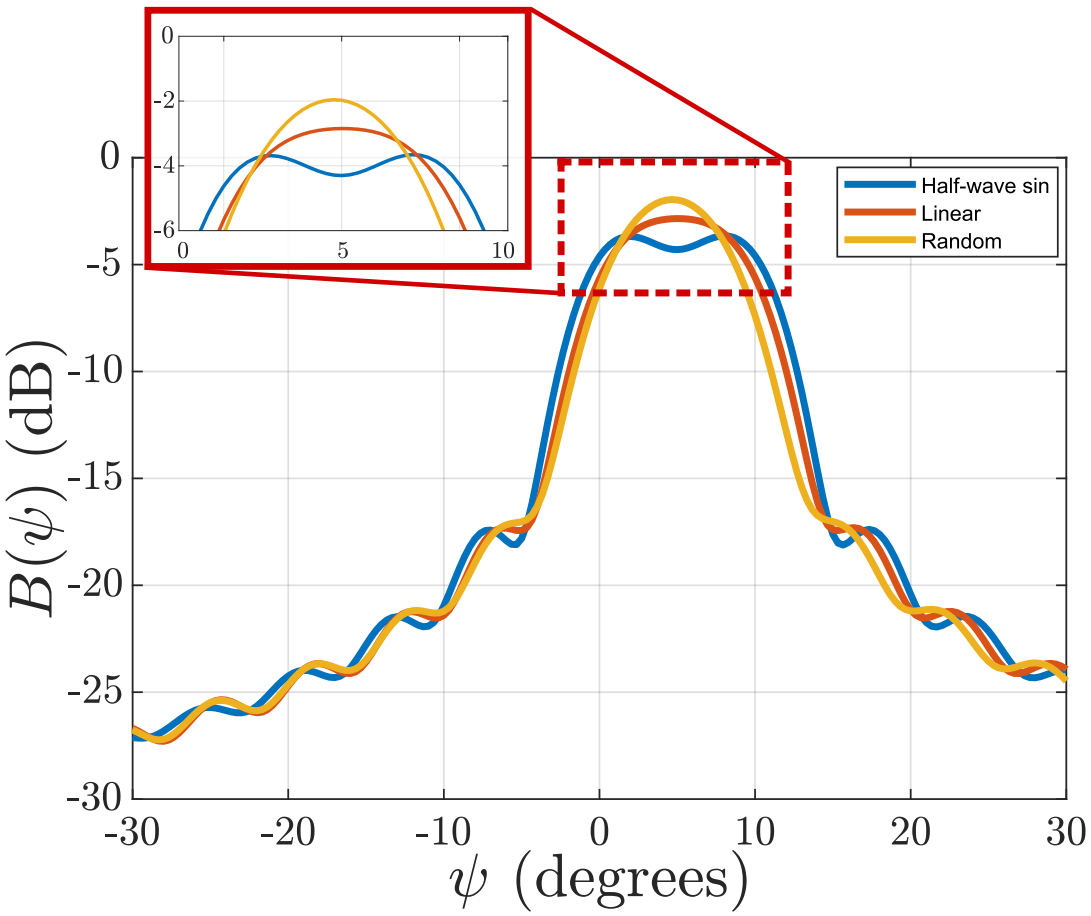

Figure 4.4: Aggregate beampattern comparison between the half-wave sinusoid, linear sweep, and random fast-time steering patterns for center-look direction $\psi_C = 5°$.

An interesting thing to note is how the main lobe of the randomized spatial modulation emission is slightly off-center from the center-look direction of 5°. Due to the steering being generated from a uniform PDF each new spatial offset can reside at any location bounded by $\psi_C \pm 5°$. If one were to look at the mean of the spatial offsets it would be slightly less than the current center look direction in this case. Over enough pulses or a long enough single segment the peak of the main lobe would be centered in the proper location. Next consider the peak normalized ABP responses for the three techniques in Figure 4.5. This figure allows for easy observation of the enhanced spatial resolution of random spatial modulation when compared to linear and half-wave sinusoid steering patterns. The tightening (or "slimming") of the mainlobe for the random spatially modulated emission shows the slight improvement to spatial resolution over the other two steering

techniques. As will be seen in section 4.6, random spatial modulation improves upon the spatial resolution of a stationary starring beam too.

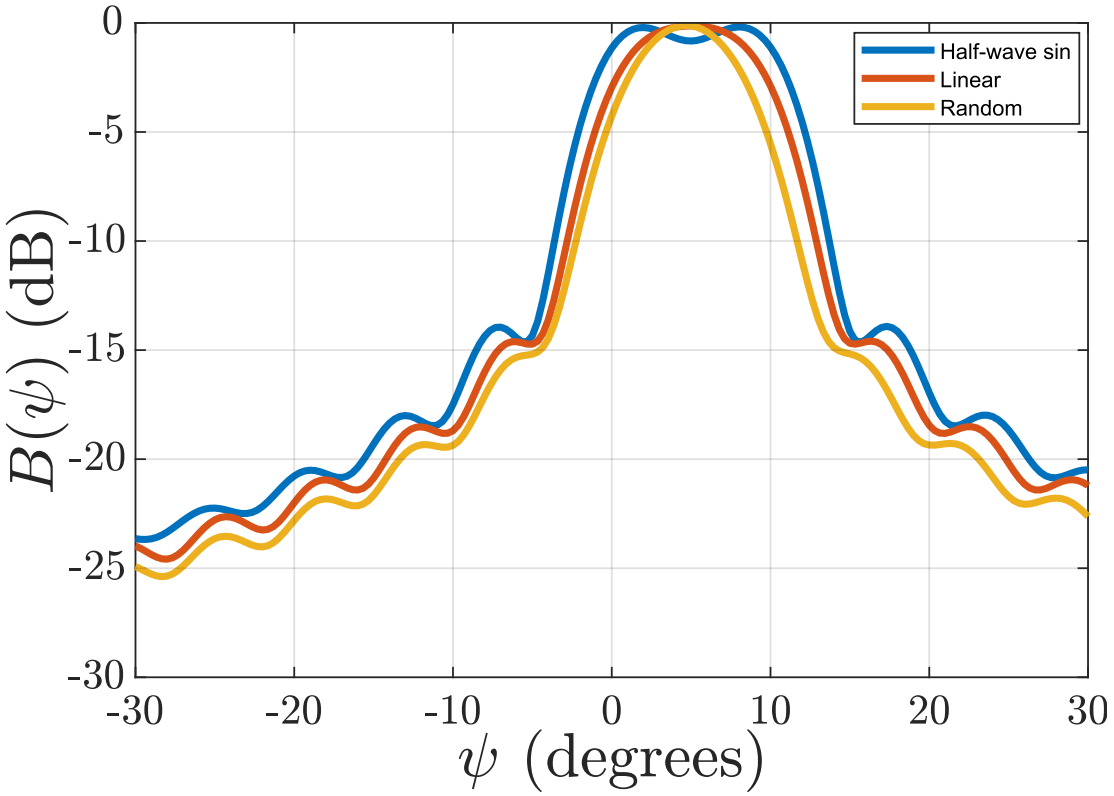

Figure 4.5: Peak normalized aggregate beampattern comparison between the half-wave sinusoid, linear sweep, and random fast-time steering patterns for center-look direction $\psi_C = 5^\circ$.

Next consider the effect of spatial modulation on the spectra of transmitted signals in Figures 4.6 and 4.7. Within each plot is the spectrum of three individual array elements. The three elements are the outermost elements of the ULA and the center or next to center element. Figure 4.6 depicts the spectrum of an LFM when linearly steered in fast-time. The purpose of this figure is to offer insight into how the bandwidth of the transmitted signal expands during linear spatial modulation. The offset of the yellow and blue traces from the red trace illustrate this expansion. The total growth in bandwidth can be calculated as the difference between the blue and yellow traces. Due to the relationship between frequency and phase, the spectrum of each array element will be shifted slightly lower or higher in frequency than the center-most element.

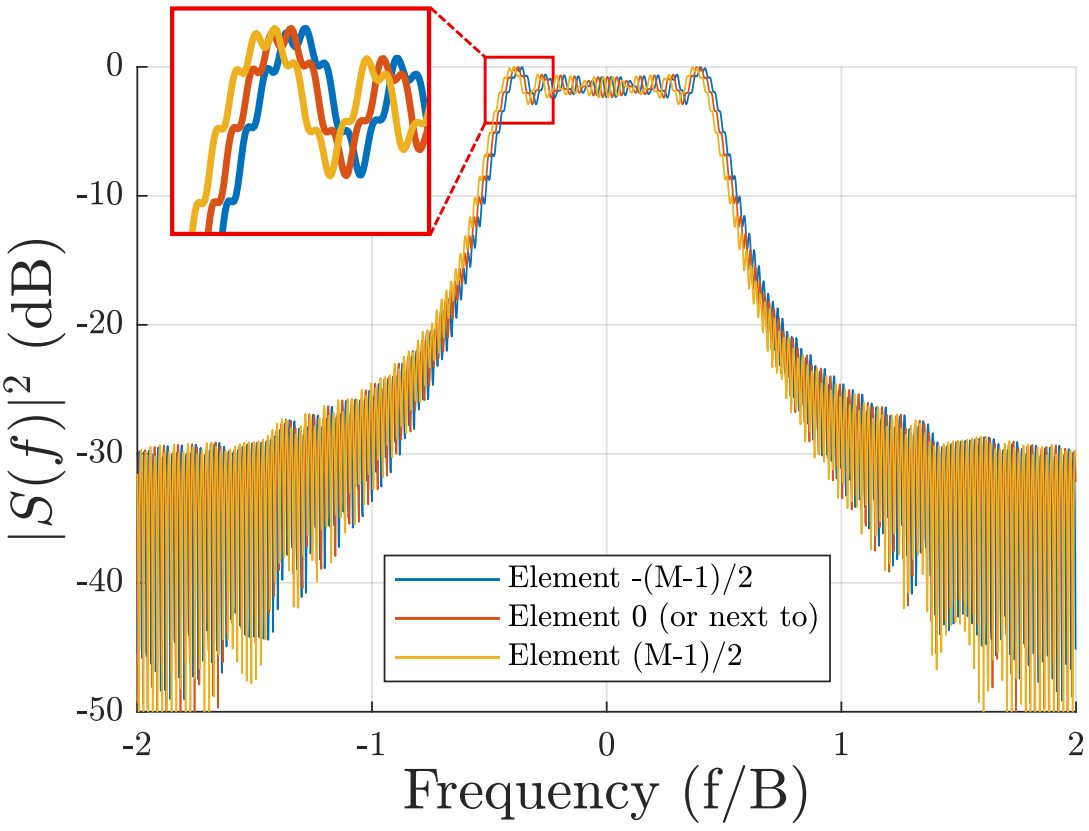

Figure 4.6: Transmit spectra of the first, middle (or next-to-middle), and last element of a ULA when using an LFM and linear spatial modulation.

Next is the spectra of the random spatially modulated signals when transmitting the PRO-FM waveform. This spectrum appears messy and the slight bandwidth expansion is difficult, if not impossible to observe with the eye. However, even though the spectrum appears spinous and messy the Gaussian-like ship is readily apparent. Any bandwidth expansion due to this emission scheme is difficult to observe also. Please note that all simulation results shown in this section use only a single pulse or waveforms segments and no coherent processing is implemented. Multiple pulses could be integrated to show tighter spectra and better responses. Single-pulse performance, however, is good enough for the sake of simulation and lends better insight into the effects that random spatial modulation has on the transmitted signal.

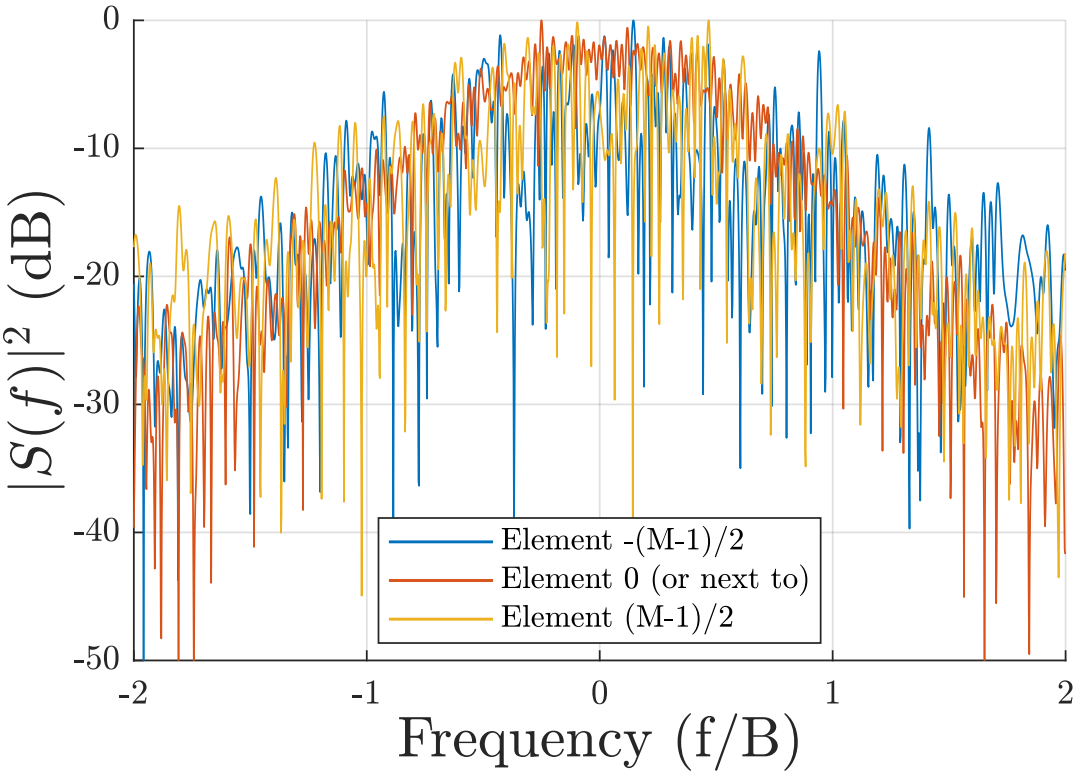

Figure 4.7: Transmit spectra of the first, middle (or next-to-middle), and last element of a ULA when using the PRO-FM waveform and random spatial modulation.

4.5 2-D Spatially Modulated FM Noise Emissions

This section will further extrapolate the previous spatial modulation formulation to incorporate a second spatial dimension with a FM noise emission. The 2-D spatially modulated emissions are forged using a special type of MIMO to form a fast-time-varying coherent beam, as developed in [1, 40, 41, 43, 44] and further explored in [42]. The PRO-FM waveform formulation described in detail in 2.10 and a specialized version extrapolated for use with the WDA, expressed in section 4.2. Once the spectral optimization of the L waveform segments is complete, a phase rotation is completed as described in (4.1). Thus the bank of waveforms $s_L(t)$ is prepared to be applied to spatial modulation.

The array geometry shown in Figure 4.8 describes a uniform planar array (UPA) with elements M_x and M_z in the x- and z-planes and array center located at the origin, coordinate location $(0,0)$.

The total number of array elements The spacing between adjacent elements is d with indexing described by

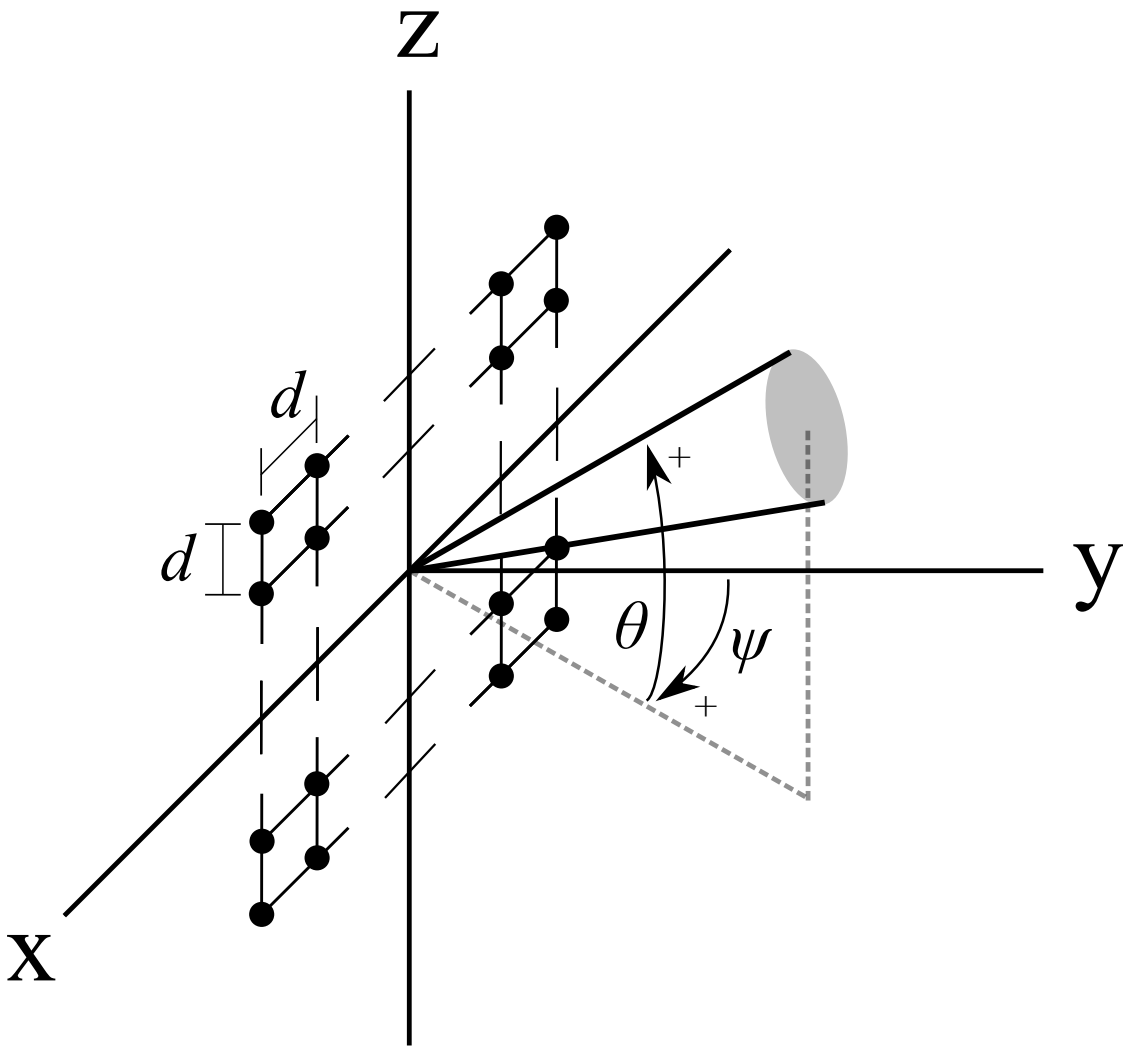

Figure 4.8: Uniform planar array geometry used to simulate 2-D spatial modulation emissions.

$$m_{\mathrm{x}} = \frac{-(M_{\mathrm{x}}-1)}{2}, \frac{-(M_{\mathrm{x}}-1)}{2}+1, \ldots, \frac{+(M_{\mathrm{x}}-1)}{2} \tag{4.11}$$

and

$$m_{\mathrm{z}} = \frac{-(M_{\mathrm{z}}-1)}{2}, \frac{-(M_{\mathrm{z}}-1)}{2}+1, \ldots, \frac{+(M_{\mathrm{z}}-1)}{2}. \tag{4.12}$$

This particular indexing is chosen such that the Azimuth angle, ψ, and elevation angle, θ, are zero at array boresight, ensuring the center of the array maintains coordinate location $(0,0)$, with range

$(-90^\circ, 90^\circ)$. The wave numbers

$$k_{\mathrm{x}}(\psi,\theta) = \frac{2\pi d}{\lambda}\sin\psi\cos\theta \tag{4.13}$$

and

$$k_{\mathrm{z}}(\theta) = \frac{2\pi d}{\lambda}\sin\theta \tag{4.14}$$

hold under the narrowband array assumption [84] with wavelength λ dependent on the center frequency.

A length $N+1$ code containing 2-D spatial offset values defined as $\{\Delta_0^{\mathrm{az}},\ \Delta_0^{\mathrm{az}},\ \ldots,\ \Delta_0^{\mathrm{az}}\}$ and $\{\Delta_0^{\mathrm{el}},\ \Delta_0^{\mathrm{el}},\ \ldots,\ \Delta_0^{\mathrm{el}}\}$ is generated for each waveform pulse (or segment) which designates the fast-time beam steering relative to array center look direction $(\psi_{\mathrm{C}},\ \theta_{\mathrm{C}})$. The offsets in azimuth and elevation are independently generated to avoid possible correlation. During the *n*th segment of the spatial code, the beam coherently sweeps from the previous offset location $(\psi_{n-1},\ \theta_{n-1})$ to the current modified center look direction described by $\psi_n = \psi_{\mathrm{C}} + \Delta_n^{\mathrm{az}}$ and $\theta_n = \theta_{\mathrm{C}} + \theta_n^{\mathrm{el}}$.

The PCFM architecture (described in detail in section 2.9) is used to transform the spatial offset codes into continuous phase-offset sequences that can be applied to continuous waveforms. As described earlier, to point the mainbeam of an array to a certain coordinate location in space via electronic steering the coordinate values must be transformed into a phase offset to be applied to each element. The continuous-time PCFM phase offset is defined as

$$\varepsilon_{\mathrm{x},n} = \frac{2\pi d}{\lambda}\Big[\sin\psi_n\cos\theta_n - \sin\psi_{n-1}\cos\theta_{n-1}\Big] \tag{4.15}$$

for azimuth and

$$\varepsilon_{\mathrm{z},n} = \frac{2\pi d}{\lambda}\Big[\sin\theta_n - \sin\theta_{n-1}\Big] \tag{4.16}$$

for elevation. Indexing is characterized from $n = 1,\ \ldots,\ N-1$ and are stored in $N\times 1$ vectors $\mathbf{x}_{\mathrm{x}} = \big[\varepsilon_{\mathrm{x},1},\ \ldots,\ \varepsilon_{\mathrm{x},N}\big]^T$ and $\mathbf{x}_{\mathrm{z}} = \big[\varepsilon_{\mathrm{z},1},\ \ldots,\ \varepsilon_{\mathrm{z},N}\big]^T$ which parameterize the azimuth and elevation spatial modulations. These vectors contain a sequence of phase-offsets that will be applied to the

signals sent to each array element to control the fast-time steering directions.

The spatially modulated signals in each dimension are thus

$$b_{\mathrm{x}}(t;\mathbf{x}_{\mathrm{x}}) = \exp\left\{ -j\left(\sum_{n=1}^{N} \varepsilon_{\mathrm{x},n} \int_0^t \mathrm{g}\big(\zeta-(n-1)T_p\big)d\zeta + \bar{\Delta}_{\mathrm{x},0} \right) \right\} \tag{4.17}$$

and

$$b_{\mathrm{z}}(t;\mathbf{x}_{\mathrm{z}}) = \exp\left\{ -j\left(\sum_{n=1}^{N} \varepsilon_{\mathrm{z},n} \int_0^t \mathrm{g}\big(\zeta-(n-1)T_p\big)d\zeta + \bar{\Delta}_{\mathrm{z},0} \right) \right\} \tag{4.18}$$

for azimith and elevation respectively, where $\mathrm{g}(t)$ is some desired shaping filter over duration T_{p}, that integrates to 1 over the interval bounded by $\big[0, T_{\mathrm{p}}\big]$. The initial electrical angles are

$$\bar{\Delta}_{\mathrm{x},0} = \frac{2\pi d}{\lambda} \sin\left(\psi_C + \Delta_0^{\mathrm{az}}\right) \cos\left(\theta_C + \Delta_0^{\mathrm{el}}\right) \tag{4.19}$$

and

$$\bar{\Delta}_{\mathrm{z},0} = \frac{2\pi d}{\lambda} \sin\left(\theta_C + \Delta_0^{\mathrm{el}}\right) \tag{4.20}$$

for each center look direction $\big(\psi_{\mathrm{C}}, \theta_{\mathrm{C}}\big)$ and corresponding center look direction with spatial offset $\big(\psi_{\mathrm{C}} + \Delta_0^{\mathrm{az}}, \theta_{\mathrm{C}} + \Delta_0^{\mathrm{el}}\big)$.

The spatial offset sequences $\big\{\Delta_0^{\mathrm{az}}, \Delta_1^{\mathrm{az}}, \ldots, \Delta_N^{\mathrm{az}}\big\}$ and $\big\{\Delta_0^{\mathrm{el}}, \Delta_1^{\mathrm{el}}, \ldots, \Delta_N^{\mathrm{el}}\big\}$ are created by randomly sampling from a prescribed PDF that is formed to subtend a solid angle in space and is symmetric about the center look directions mentioned above. By randomly and independently sampling the chosen PDF, the fast-time steering will mimic FEM produced when staring or focusing on an object for extended periods of time. To illustrate this implementation consider Figures 4.9 and 4.10. The center cut of a Gaussian distribution truncated at -5° and 5° so as to stay within $\pm 5^\circ$ of the center look direction is shown in Figure 4.9. Figure 4.10 illustrates how the same truncated Gaussian PDF in 2-D space for a center look direction of $(15^\circ,\ 10^\circ)$. Do note that the bounds on the PDF are defined with respect to the center look direction and not in absolute azimuth or absolute elevation.

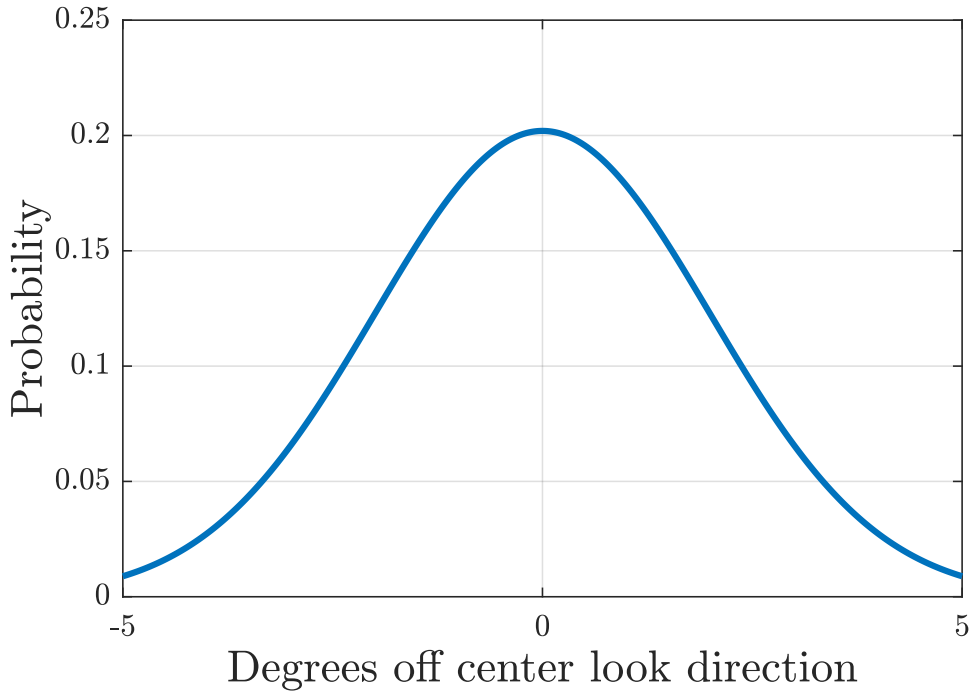

Figure 4.9: Example PDF for fast-time beamsteering (Truncated Gaussian).

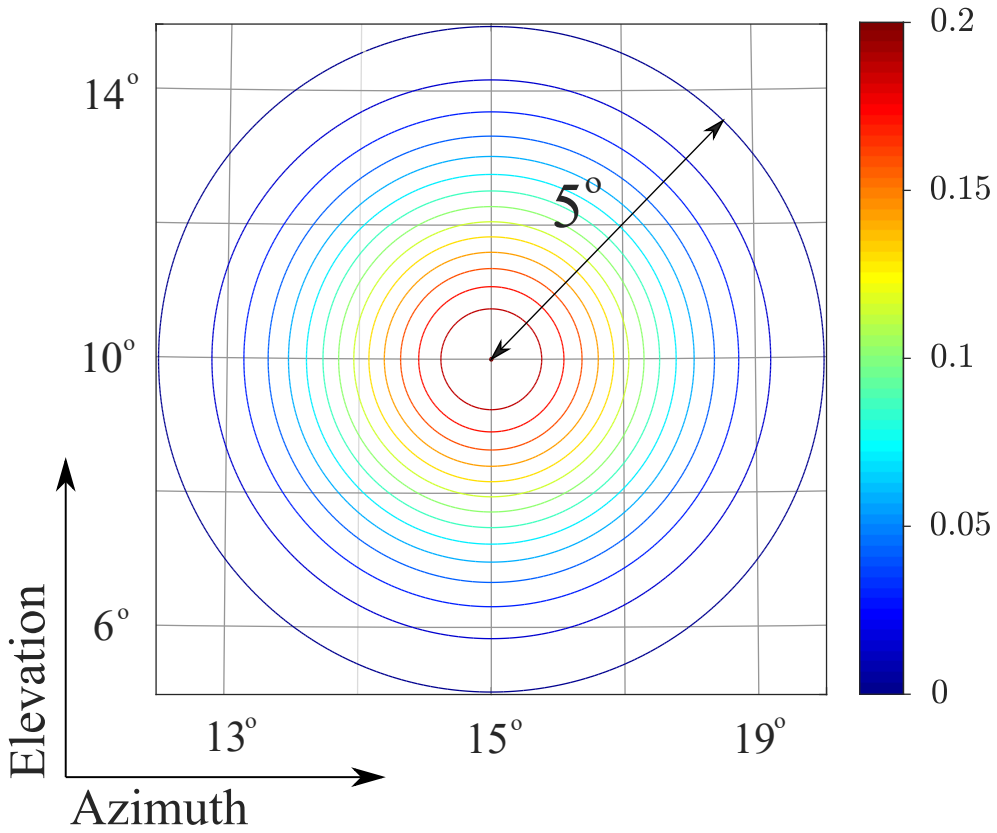

Figure 4.10: Truncated Gaussian PDF in 2-D for $\psi_C = 15°$ and $\theta_C = 10°$.

Each of the L PRO-FM waveform segments will have L corresponding spatial modulation codes $\mathbf{x}_{\mathrm{x},\ell}$ and $\mathbf{x}_{\mathrm{z},\ell}$ as well as individually defined center look directions $(\psi_{\mathrm{C}}, \theta_{\mathrm{C}})$. The center look direction for this emission scheme can change at a maximum rate equal to the time width T_{p} of each segment. If the center look direction lingers in the same direction for multiple segments then a mismatch in phase and consequent discontinuity will occur if the proceeding waveform is not modified by (4.1), completed by setting $\Delta^{\mathrm{az}}_{0,\ell} = \Delta^{\mathrm{az}}_{N,\ell-1}$ and $\Delta^{\mathrm{el}}_{0,\ell} = \Delta^{\mathrm{el}}_{N,\ell-1}$. Otherwise, if time-adjacent waveform segments require different center look directions a transition stage of duration one code interval is inserted between the waveforms to steer the coherent beam from $(\psi_{\mathrm{C},\ell-1} + \Delta^{\mathrm{az}}_{N,\ell-1},\ \theta_{\mathrm{C},\ell-1} + \Delta^{\mathrm{el}}_{N,\ell-1})$ to $(\psi_{\mathrm{C},\ell} + \Delta^{\mathrm{az}}_{0,\ell},\ \theta_{\mathrm{C},\ell} + \Delta^{\mathrm{el}}_{0,\ell})$.

Thus, combining the the spatial modulation signals produced in (4.17) and (4.18) with the ℓth PRO-FM waveform segment from (4.1) yields the set of MIMO waveforms

$$s_{\mathbf{m},\ell}(t, \psi_{\mathrm{C}}, \theta_{\mathrm{C}}) = \frac{1}{\sqrt{T_{\mathrm{p}}}} s_{\ell}(t) \Big(b_{\mathrm{x}}(t; \mathbf{x}_{\mathrm{x},\ell}) \Big)^{m_{\mathrm{x}}} \Big(b_{\mathrm{z}}(t; \mathbf{x}_{\mathrm{z},\ell}) \Big)^{m_{\mathrm{z}}} \tag{4.21}$$

that are generated by the array element indexed as $\mathbf{m} = (m_{\mathrm{x}}, m_{\mathrm{z}})$ for the ℓth waveform segment. This normalizaiton term provides unit energy to each transmit antenna element with $(\bullet)^{m_{\mathrm{x}}}$ and $(\bullet)^{m_{\mathrm{z}}}$ producing the Vandermonde response, facilitating beam steering in azimuth and elevation. The PCFM architecture described in section 2.9 can be used to generate $M_{\mathrm{x}} M_{\mathrm{z}}$ physical 2-D MIMO emissions. Thus, a normalized baseband formulation of the far-field emission during the ℓth segment is

$$\mathrm{g}_{\ell}(t, \psi, \theta) = \frac{1}{M_{\mathrm{x}} M_{\mathrm{z}}} \sum_{m_{\mathrm{x}}} \sum_{m_{\mathrm{z}}} s_{\mathbf{m},\ell}(t) e^{j\left(k_{\mathrm{x}}(\psi,\theta) m_{\mathrm{x}} + k_{\mathrm{z}}(\theta) m_{\mathrm{z}}\right)}. \tag{4.22}$$

The aggregate beam pattern (ABP) [1, 40–42, 44] of the resulting emission is also defined as

$$B(\psi, \theta) = \frac{1}{TL} \sum_{\ell=1}^{L} \int_{0}^{T_{\mathrm{p}}} \left| \mathrm{g}_{\ell}\big(t, \psi, \theta\big) \right|^2 dt \tag{4.23}$$

and time-varying beam pattern (TVBP) as

$$B_{\mathrm{TV}}(t,\psi,\theta) = g_{\ell}(t,\psi,\theta)\; g_{\ell}^{*}(t,\psi,\theta) \tag{4.24}$$

where $(\bullet)^{*}$ denotes conjugation. The ABP of the FEMR emission will be used to display benefits with regard to spatial resolution enhancement at the cost of SNR. The TVBP of a 2-D array emission is difficult to view in a report format and requires recording and playback of a movie to effectively describe what is occurring. Because of this the TVBP of the 2-D emission will not be shown in this report.

4.6 2-D Spatial Modulation Simulations

The assessment of the random spatial modulation employed by the fixational eye movement radar (FEMR) emission scheme will be completed by comparing the impact of PDF selection and how it relates spatial resolution enhancement with loss in SNR. The loss in SNR occurs due to the smearing of the main beam when its direction of emission is modulated with fast-time. The examples shown include changing the look direction of adjacent waveform segments and discrimination of closely-spaced targets. The FEMR emission will be compared to other array emission types that do not possess spatial modulation, including a staring beam and spoiled beam.

4.6.1 Relationship Between PDF Choice and SNR

Beginning with the impact on receive SNR determined solely by the fast-time beamsteering PDF, which can be of any arbitrary shape, consider the following example. Figure 4.11 shows three possible choices for the spatial offset PDF. The three example PDFs shown are the truncated Gaussian, complementary truncated Gaussian, and uniform. We define the complementary Gaussian PDF as an "upside-down" Gaussian in shape which presents a bimodal structure by placing the higher probabilities toward the limits of the PDF. Doing this will allow for greater diversity in spatial modulation. Consider a scenario where the target scene contains a single scatterer located at array

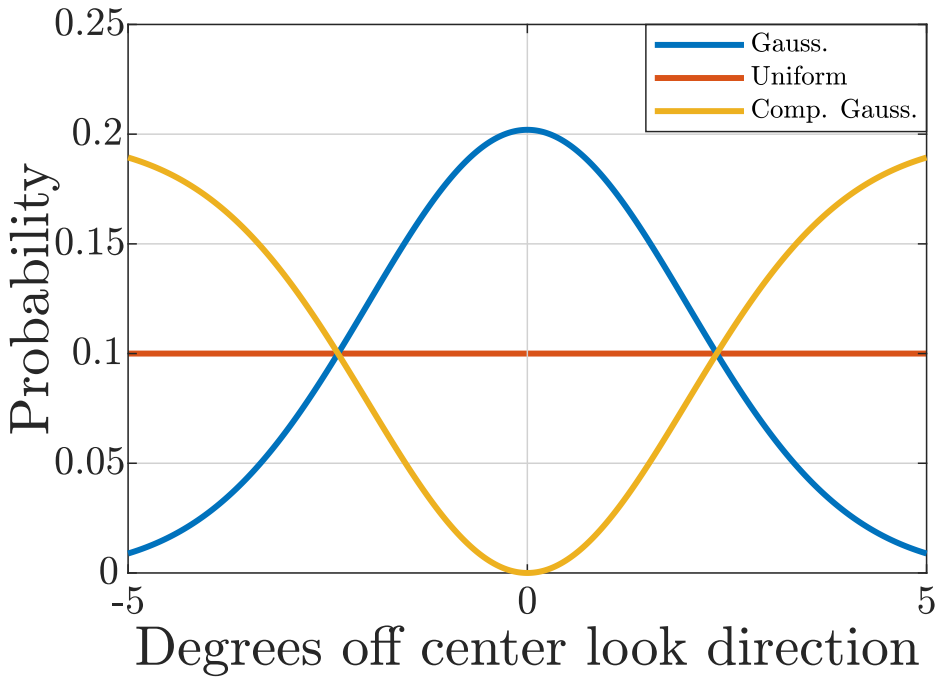

Figure 4.11: Truncated Gaussian, uniform, and complementary truncated Gaussian PDFs for random spatial modulation.

boresight and will be illuminated by a $M_x = 20$ by $M_z = 20$ UPA. The scene will be illuminated using the three PDFs shown in Figure 4.11 and the same PRO-FM waveform segment with BT of 200. Notice that each PDF is truncated to $\pm 5^\circ$ of the center look direction which corresponds to the null-to-null beamwidth (roughly $\pm 5.7^\circ$) for a starring beam at boresight. Due to the array having the same number of horizontal and vertical elements the azimuth and elevation responses will be the same, and as such we show only the azimuth aggregate beampattern responses.

Figure 4.12a illustrates the loss in SNR experienced when using different PDFs to control spatial modulation as compared to a staring beam. The staring beam displays no loss while the truncated Gaussian, uniform, and complementary truncated Gaussian PDFs exhibit decreases in SNR. Next the improvements in spatial resolution can be seen in Figure 4.12b as compared to the baseline staring case. The spatial resolution enhancement depends largely upon the PDF choice and, by observation, could be surmised that larger mean spatial modulation deviations equates better enhancements to spatial resolution. There also seems to be a direct correlation between the amount of spatial resolution enhancement and the amount of SNR loss. These figures illustrate

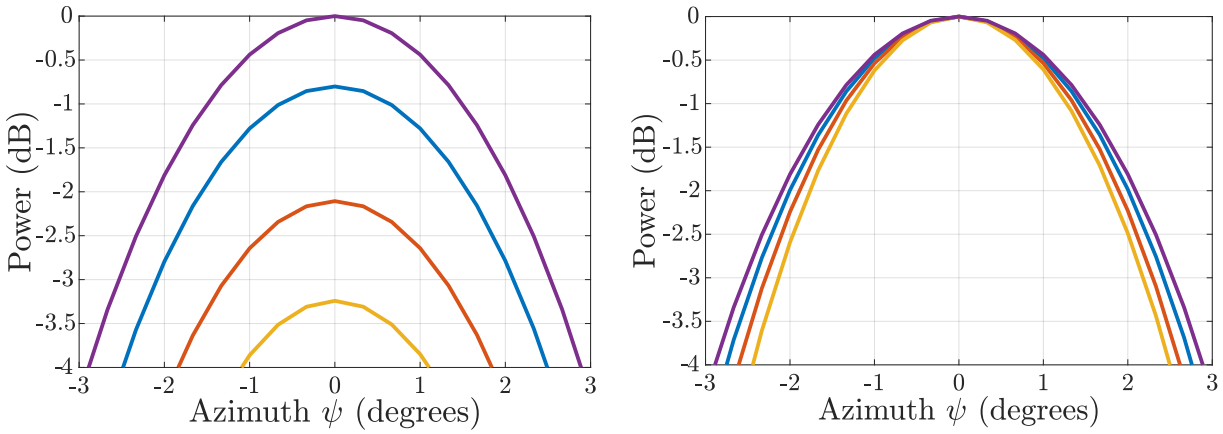

(a) Spatial ambiguity function.

(b) Normalized spatial ambiguity function.

Figure 4.12: Center cut of the azimuth-elevation ambiguity function comparing trade-off between SNR loss (a) and spatial resolution enhancement (b) for staring beam (purple), truncated Gaussian PDF (blue), uniform PDF (red), and complementary truncated Gaussian PDF (yellow).

the trade-offs between enhanced spatial resolution and SNR loss due to the size of the deviations with respect to center look direction (ψ_C, θ_C). Table 4.1 quantifies the information shown visually in Figure 4.12 to provide better insight into the benefits and costs associated with each PDF type. The improvement to spatial resolution is determined by the magnitude of the difference between the width of the baseline staring beam and the spatially modulated beams. Note that there is a slight difference between the spatial resolution enhancement in azimuth and elevation in each row of table 4.1 caused by the independent sampling of the spatial offset codes for each dimension. These percentage improvements will vary slightly from segment-to-segment caused by this random sampling.

Table 4.1: Spatial resolution enhancement and SNR loss for different random spatial modulation PDFs

Spatial Modulation Type	**Spatial Resolution** (%)		**SNR Loss** (dB)
	Azimuth	Elevation	Azimuth/Elevation
Staring beam	100	100	0
Truncated Gaussian	95.47	95.43	0.85
Uniform	90.57	89.85	2.10
Comp. Truncated Gaussian	85.15	85.80	3.25

4.6.2 Changing Look Directions

Next consider the situation where the center look direction changes from segment to segment. This function could be useful for tracking multiple targets or when scanning multiple areas simultaneously. The spatial modulation was generated using the truncated Gaussian PDF shown in Figure 4.11 with center look direction (ψ_C, θ_C) being the mean of the PDF. Two PRO-FM waveform segments were generated, each with time-bandwidth product 200. Both segments were over-sampled by 4 relative to the 3-dB bandwidth to ensure ample fidelity in simulation. The two waveform segments were emitted in different respective spatial look directions $(0^\circ, -25^\circ)$ and $(15^\circ, 10^\circ)$, meaning one segment was emitted in the first location and the next segment was emitted in the second location. A short, one code element long (so 4 discrete samples), steering sequence is embedded between the segments to facilitate continuous steering between the two look directions.

The aggregate beam pattern (ABP) of this simulated emission is shown in Figure 4.13a, calculated using (4.23), with spatial modulation being controlled by the truncated Gaussian PDF. There are two distinct mainlobes present in the ABP plot located at the corresponding emission locations. The transition stage can be seen in Figure 4.13b as the straight line connecting the last sample of the first segment to the first sample of the proceeding segment. This transition stage is inserted between adjacent segments so as to provide a continuous transition from one center-look direction to the next. Figure 4.14 shows how the bimodal nature of the complementary truncated Gaussian PDF affects the ABP, as compared to the monomodal truncated Gaussian. The differences when comparing 4.13a and 4.14a are easily observable in that the complementary Gaussian ABP adds spreading in the spatial sidelobes as well as a widening of the mainlobe.

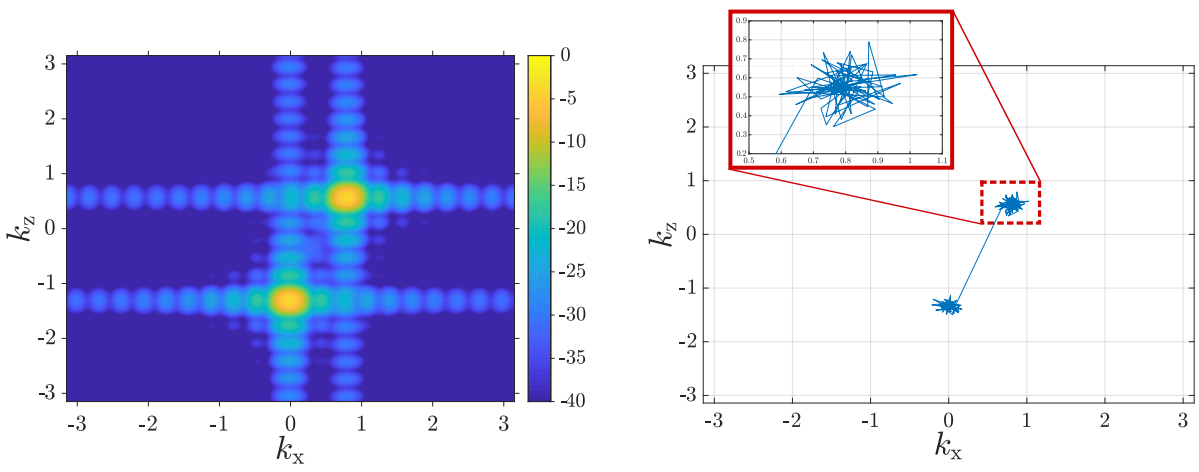

(a) (b)

Figure 4.13: Aggregate beampattern (a) and instantaneous mainlobe trace (b) in wavenumber space for random spatial modulation emitting in two different look directions, controlled by the truncated Gaussian PDF.

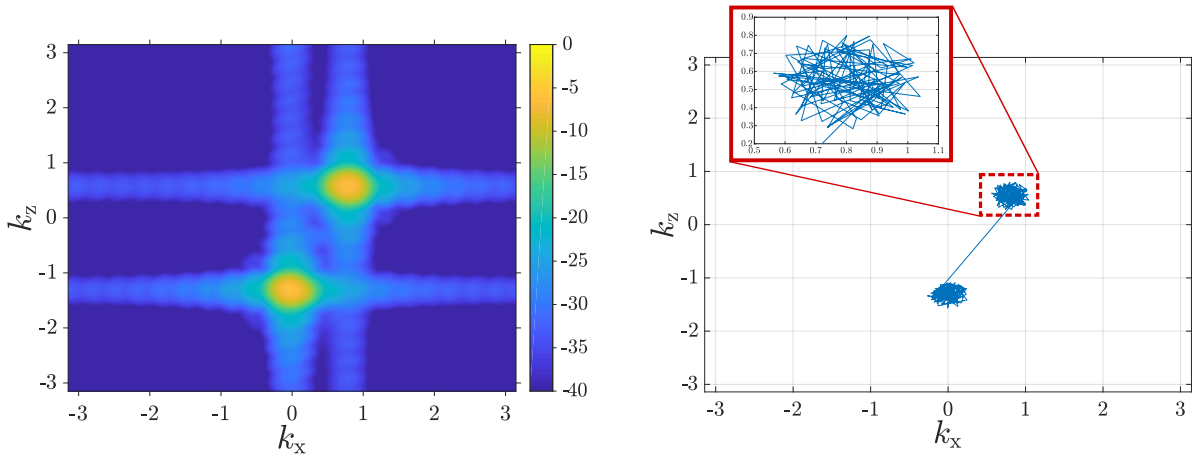

(a) (b)

Figure 4.14: Aggregate beampattern (a) and instantaneous mainlobe trace (b) in wavenumber space for random spatial modulation emitting in two different look directions, controlled by the complementary truncated Gaussian PDF.

Figures 4.13b and 4.14b display the instantaneous mainlobe trace for the spatially modulated emissions. Each figure contains a subfigure that offers a better look at the peak trace for the second look direction. Due to the mean deviation of the spatial offset step size being much smaller with the truncated Gaussian PDF, the mainbeam remains closer to the center of each look direction with very few large fast-time sweeps. The complementary truncated Gaussian displays ubiquitous large

spatial offset steps, hence the spreading observed in the associated ABP. The comparison of these two figures offers a brief glimpse at how PDF choice can influence the radiated beam pattern for each segment. Figure 4.15 displays the ABP as it would appear to an observer located close to the second center-look direction for these two waveform segments. This figure provides a good look at the directivity of this emission pattern with associated sidelobe structure.

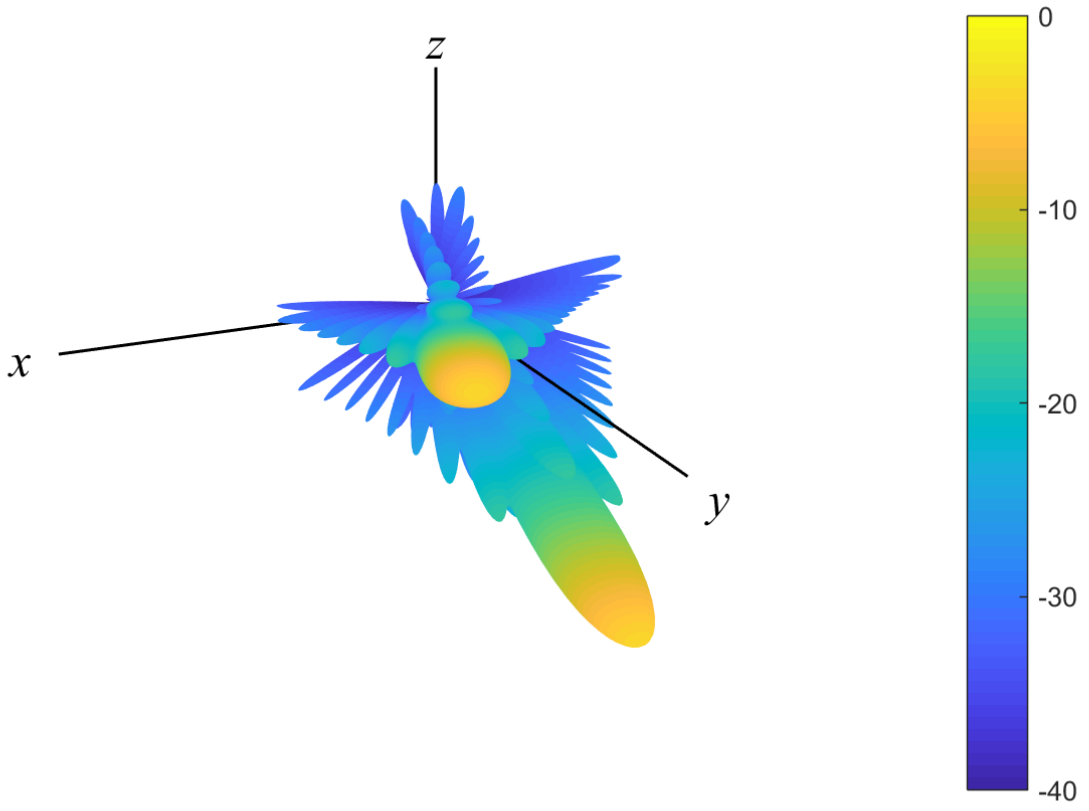

Figure 4.15: A 3D representation of the aggregate beam pattern for two adjacent 2-D spatially modulated waveform segments centered at $(0°, -25°)$ and $(15°, 10°)$.

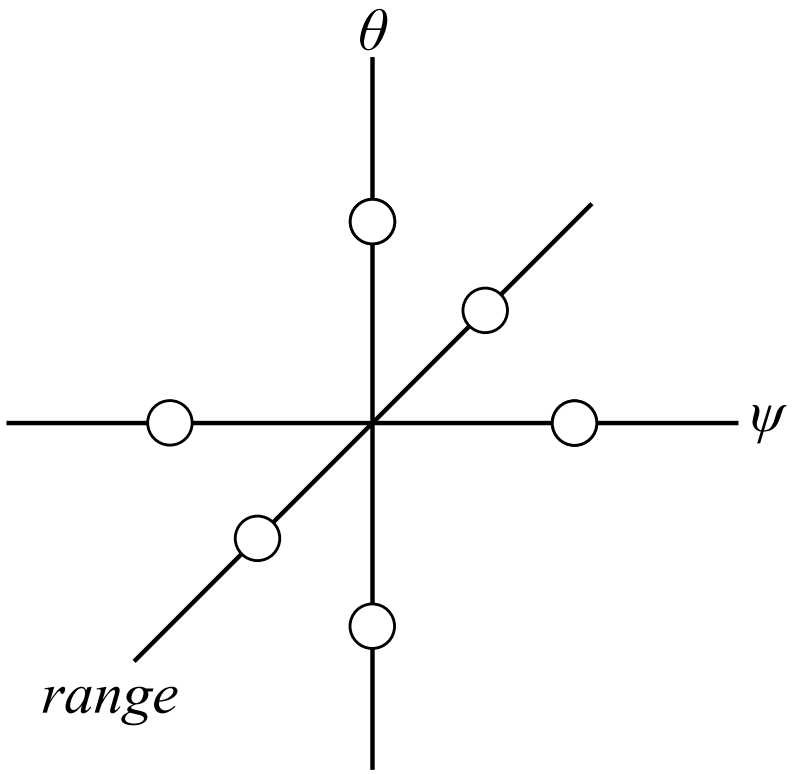

Figure 4.16: "Jack" configuration of scatterers in range, azimuth, and elevation, where spatial separation is $\pm 4.5^\circ$ relative to center look direction $(0,0)$.

4.6.3 Discrimination of Closely Spaced Targets

Next, the ability for FEMR to discriminate between closely spaced scatterers will be investigated. Consider the target configuration in Figure 4.16, which resembles a toy jack, where scatterers are offset in both spatial dimensions as well as range. This scene will be illuminated using three different emissions schemes: a staring beam, phase-only beam spoiling [89], and random spatial modulation controlled by the complementary truncated Gaussian PDF from Figure 4.11. Each scheme will utilize the same PRO-FM waveform segment with $BT = 200$, transmitted in center-look direction $(0,0)$ from a $M_{\mathrm{x}} = 20 \times M_{\mathrm{z}} = 20$ uniform planar array. The 6 scatterers were scaled such that the receive SNR of each would be 20 dB if illuminated directly with a staring beam and were assigned independent and random phase. The same noise is applied to each scene as well. To isolate the effects of random fast-time spatial modulation, and to offer an honest comparison

to the other two techniques, only the matched filter will be used for receive processing. The ability for each emission scheme to resolve targets spaced closely in range as well as 2-D space will be compared with azimuth-elevation and range-elevation plots. Note that the reason a range-azimuth plot is not shown is that the responses in azimuth and elevation are the same due to the complementary nature of uniform planar arrays.

First, the staring beam will be investigated. Figure 4.17 displays a cut of the azimuth-elevation response and Figure 4.18 displays a cut of the range-elevation response when matched filtering using only the far-field emission of a staring beam. Notice that the staring case is unable to resolve any of the four targets (possibly one, but a possible sidelobe located in the bottom right of the plot shows a larger response) offset in space. Target separation in spatial angles ϕ and ψ is poor as well. The next figure shows the range-elevation cut where the staring beam easily detects the targets offset in range but seems to miss the two targets offset in elevation, and is assumed to miss the corresponding targets offset in azimuth but are not shown.

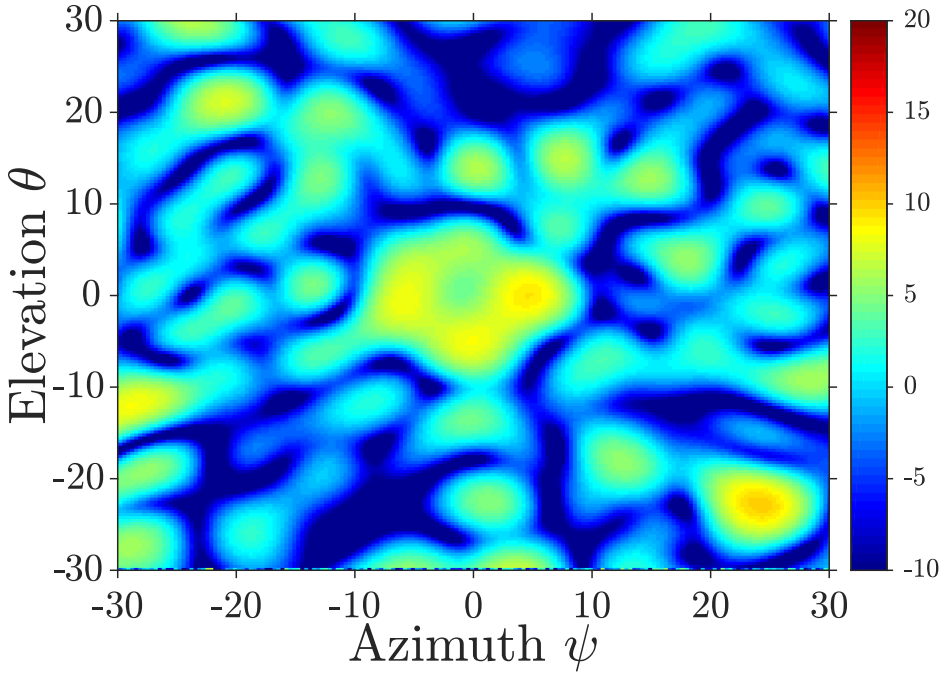

Figure 4.17: Azimuth-elevation cut for a staring beam.

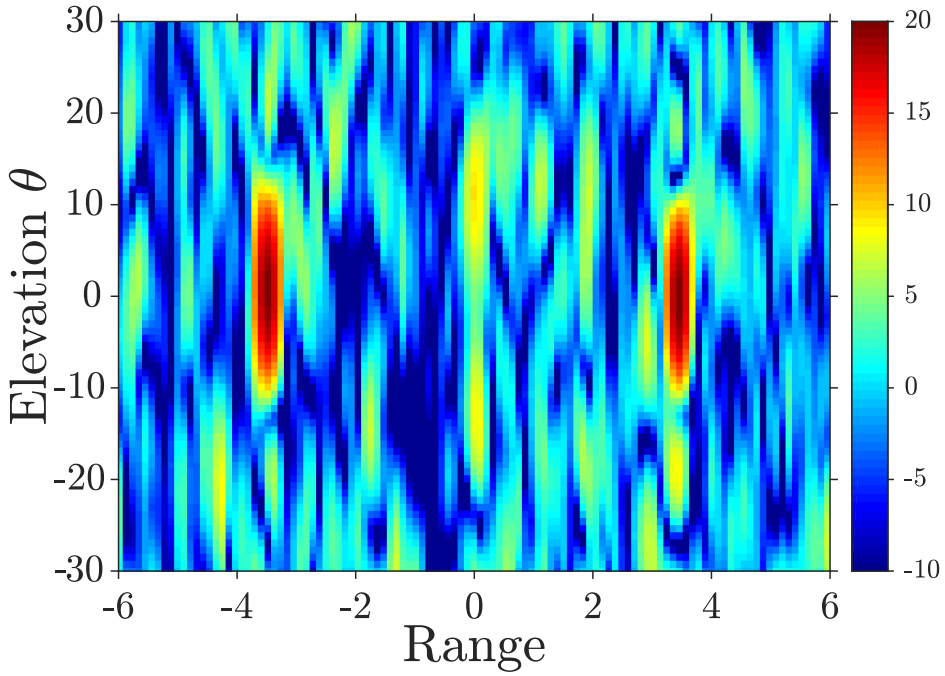

Figure 4.18: Range-elevation cut for a staring beam.

Next, the static phase-only beam spoiled emission will be evaluated. Figures 4.19 and 4.20 display the azimuth-elevation and range-elevation responses. The phase-only beam spoiling was administered by applying a relatively small random dithering to a staring transmit beam. Beam spoiling is employed to provide wider main beam coverage of a target scene. When comparing the azimuth-elevation cuts of the staring beam with the beam spoiled emission there seems to be better target visibility when randomly dithering on transmit but all four targets are clearly not discernible from each other. The improvement in the range-elevation plot is negligible with regard to the scatterers offset in spatial angle. A loss in SNR is apparent for the targets offset in range as well.

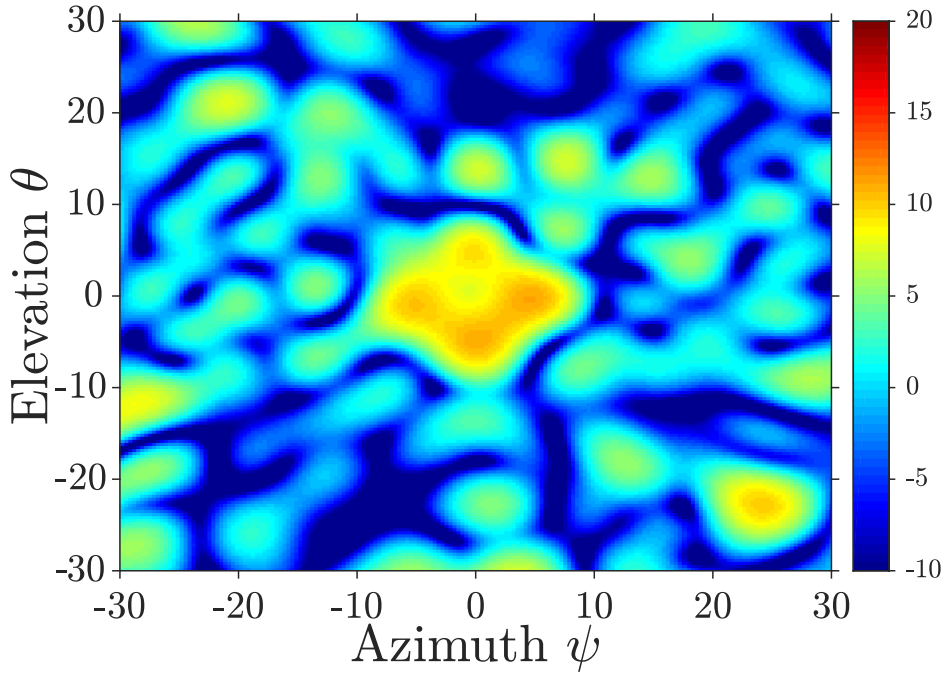

Figure 4.19: Azimuth-elevation cut for a static spatially-dithered beam.

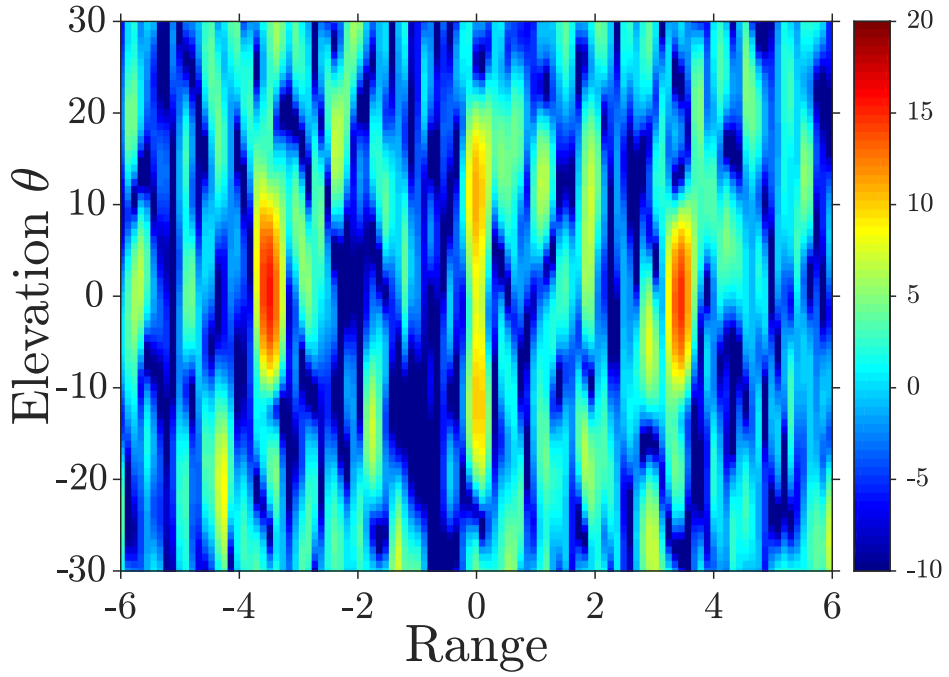

Figure 4.20: Range-elevation cut for a static spatially-dithered beam.

Lastly, the FEMR emission will be evaluated when utilizing the complementary truncated Gaussian PDF to control the spatial offset sequences. Note that the same noise vector for the pre-

vious two emission techniques was also used for this simulation. Since the matched filter is also randomly changing with respect to spatial angle the sidelobes of the emission combine to form a a different scene for each waveform segment as long as different spatial offset sequences are used for each segment. This combining of sidelobes is what causes the azimuth-elevation and range-elevation plots for the spatially modulated emission to look different from the staring and static beam spoiled emissions. It is interesting to note that the noise appears to have finer granularity, almost appearing like an improvement to the resolution of the azimuth-elevation and range-elevation plots. Here the targets offset in spatial angle are easily observable with four distinct peaks shown in Figure 4.21. The separability between each peak is greater than 3 dB as well.

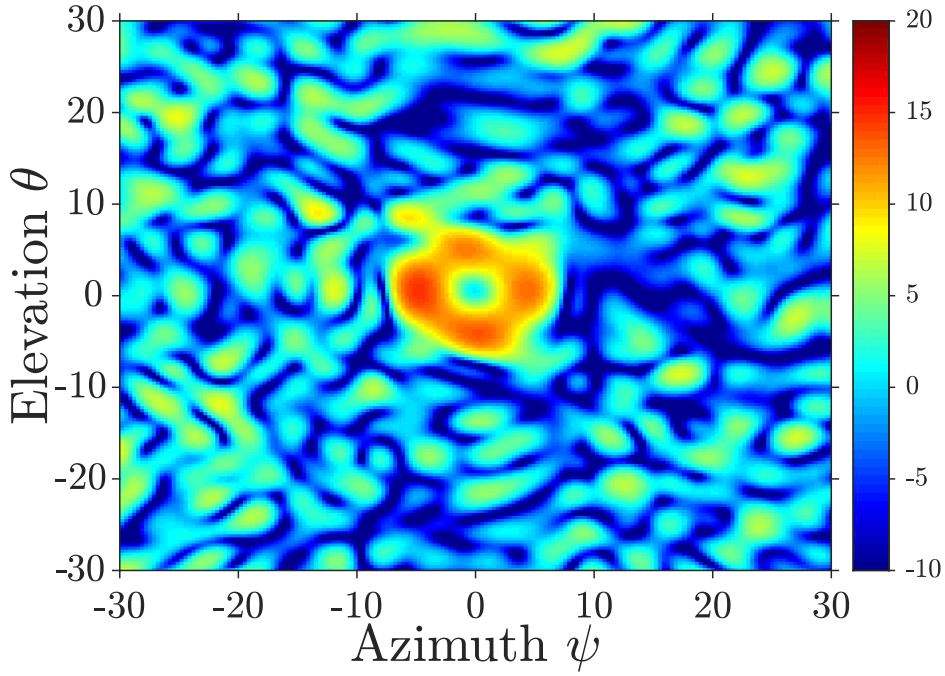

Figure 4.21: Azimuth-elevation cut for a random spatially modulated beam controlled by the complementary truncated Gaussian PDF.

Figure 4.22 displays the range-elevation cut of the match filtered response. While there is a slight loss in receive SNR for each target, the separability between all four is quite good. The targets offset in range are easily discernible amongst the noisy background while showing off the improvement to spatial resolution when compared to Figure 4.18. The targets offset in elevation are easily observable with good separation and receive SNR.

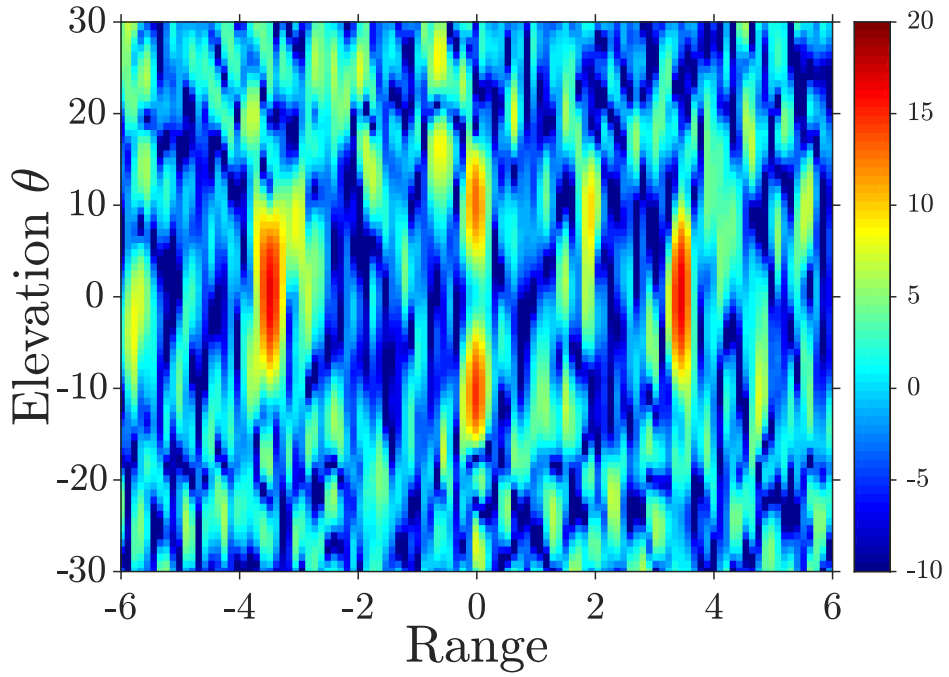

Figure 4.22: Range-elevation cut for a random spatially modulated beam controlled by the complementary truncated Gaussian PDF.

4.6.4 Example Steering Shapes

This section serves as a gallery of sorts for various steering patterns or shapes that were extrapolated from the base spatial modulation framework. The purpose of this section is to convey the near limitless flexibility this emission scheme provides in terms of controlling the aggregate beam pattern and random dithering shape/style. All patterns are generated using the 2-D spatial modulation formulation described in detail within section 4.5. Each emission uses a corresponding number of independent PRO-FM waveform segments described in the figure text for each scheme. Note that some of these patterns may not hold any significance from the standpoint of a practical application but instead serve to show that any shape is possible given the proper constraints.

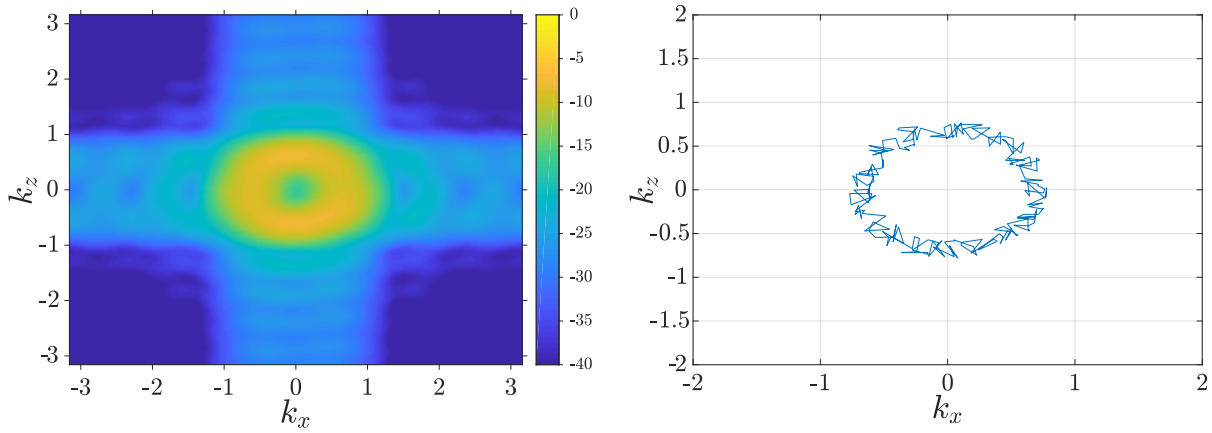

Figure 4.23: Fast-time conical scan (wreath) with random dithering.

Figure 4.23 depicts the aggregate beam pattern (left) and instantaneous peak-trace of what could be called a fast-time conical scan pattern. This pattern is created by imposing random dithering while the array steers in a circle. This shape is also affectionately referred to as the "wreath" steering pattern because the random offsets added to the circle give the appearance of a wreath-like shape. This pattern is constructed from a single PRO-FM waveform segment and corresponding 2-D spatial modulation segment, meaning each pulse (or CW segment) will traverse the entire circle. This steering pattern could have applications to tracking or large area search because the entire circle is traversed with a single pulse/segment. This technique would be much more appealing to standard conical scan due to traditional conical scan requiring many pulses as well as mechanical motion to steer in the complete circle. This method also shows how easy generating arbitrary shapes and applying random spatial offsets to the underlying structure is.

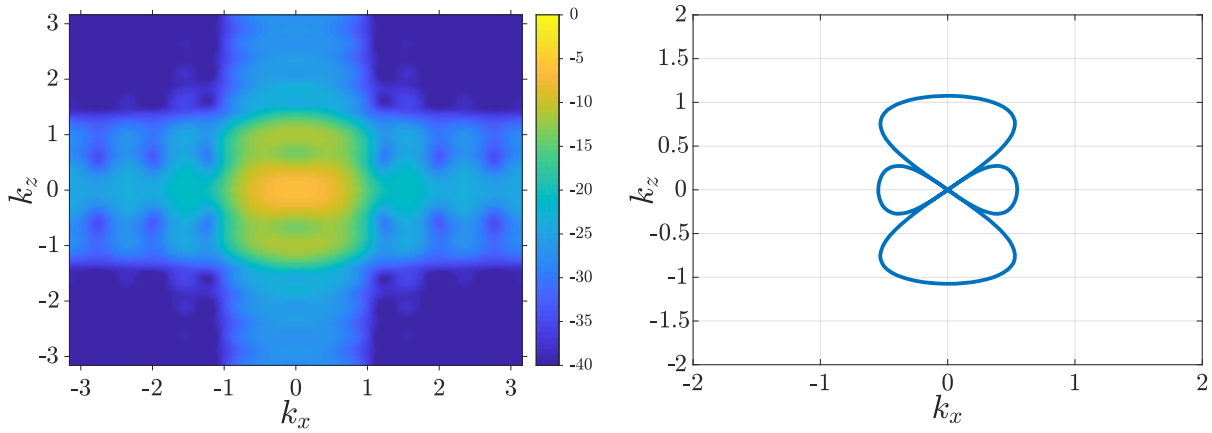

Figure 4.24: A double figure-eight steering pattern over two segments with no dithering.

Figure 4.24 displays a steering shape consisting of two spatial modulation segments combined with two independently generated PRO-FM waveform segments, with the first steering segment being a horizontal figure-eight and the second steering segment being a larger vertical figure-eight. The aggregate beampattern can be seen in the left portion of the figure with the instantaneous mainbeam peak-trace (or "etch-a-sketch") plot shown on the right. No random dithering has been applied to the "double figure-eight" shape but could easily be done. This shape was made just to show how simple shapes can easily be made and modified. However, a shape similar to this could have some use when tracking multiple targets as a form of double fast-time conical scan for tracking two targets where the center of each figure-eight loop contains a target of interest.

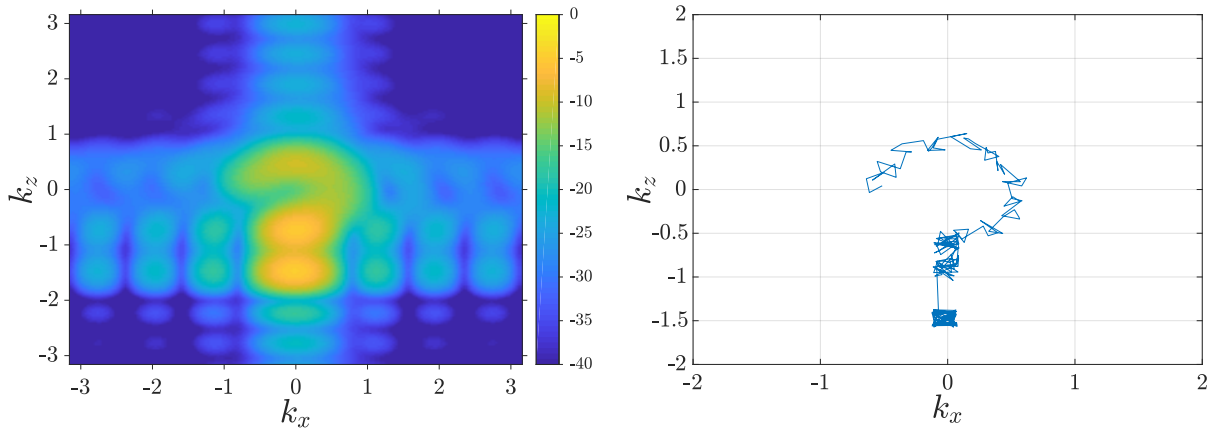

Figure 4.25: A question mark with random dithering.

Figure 4.25 shows the aggregate beampattern (left) and instantaneous mainbeam peak trace, or etch-a-sketch, (right). This steering pattern was created to show the flexibility of 2-D spatial modulation. There are three waveform and steering segments with the first composing $3\pi/2$ radians of a complete circle, the second steering in a straight line progressing downwards in elevation, and the final composing the dot at the bottom of the question mark. Note that the short transition code element can be seen between the second and third segments. The random dithering was generated via the complementary truncated Gaussian PDF with relatively tight bounds on the PDF steering range to maintain a recognizably shaped aggregate beampattern.

4.7 Observations

Previous research on spatial modulation [1, 40, 41, 43, 44] laid the foundation for 2-D random spatial modulation and subsequent FEMR emission scheme [42]. The FEMR emission has been determined to effectively mimic the passive actuation of the eye with an active, and coherent, MIMO emission. The fast-time steering of the coherent beam is created by sampling from a predefined and arbitrarily shaped PDF. Examples of possible PDFs are shown in section 4.6.1. The width (extent of spatial angles) of the PDF as well as the shape can be changed to control the spread and placement of power within 2-D space. If considering the FEMR emission scheme at the system level a multimode functionality could be implemented where target returns feed back into the generation of the spatial offset sequences and switch between a wider "search mode" and more narrowed "interrogation mode".

The target separation for the simulations in section 4.6.3 was chosen to lie close to the nulls of a staring beam for the selected array geometry. Because of this, these results displayed poor target separability when using a static staring beam since very little power was placed on those targets. The next set of simulations involved broadening the main beam to place more power on the spatially distributed targets. This resulted in slightly improved receive SNR but little in the way of improved separability. The FEMR emission, when using a modestly wide bounded spatial modulation PDF, was able to place enough power on the spatially offset targets to offer good separability

and SNR. These simulations demonstrate the detrimental effects on target detection when closely spaced targets reside slightly outside of the 3 dB beamwidth of a staring and beamspoiled beam. These detection drawbacks can be mitigated through the use of spatial modulation to ensure power is placed on target. Keep in mind that these results use only a single pulse (or waveform segment) and thus no coherent integration is occurring. With inclusion of multiple pulses and subsequent coherent integration the results would provide performance improvements matching standard coherent processing gain. This series of simulations was formulated to emphasize the single pulse performance of the FEMR.

Unfortunately the simulation results above have not been verified with experimental free-space measurements due to the lack of a MIMO testbed. This testbed would require arbitrary waveform generation capabilities at the element level as well as complex phase synchronization between the transmitting elements to reduce inter-element distortions of the underlying PRO-FM waveform. However, because such care and attention has been placed into making the emissions constant modulus and continuous, there is no reason why 2-D random spatial modulation would not be amenable to hardware in its current formulation. With hardware-in-the-loop emission optimization detrimental calibration effects could be handled during emisison formulation.

Chapter 5

Conclusions and Future Work

Current radar technologies utilizing arbitrary waveform generation capabilities provide remarkable control and on-the-fly tunability to both the transmitter and receiver. This adaptability has created new research areas and solved problems once thought impossible. This work exploits the many desirable properties associated with waveform diversity to explore a polarization diverse and a biomimetic emission schemes employing FM-noise waveforms. Using both simulated and experimental results two possible applications for FM-noise radar emissions have been presented. The first offering a relatively computationally efficient implementation for a simultaneous dual-polarized emission that leverages high dimensionality to avoid expensive adaptive processing techniques. The second mimicking fixational eye movements observed in mammals via a biomimetic implementation of MIMO involving fast-time beam steering.

This proposed simultaneous dual polarized FM-noise emission scheme leverages the high dimensionality of the PRO-FM waveform to provide co/cross-polarization receive separability given enough transmitted pulses. The benefit to this approach is potentially lower computational cost by avoiding the use of expensive adaptive receive processing techniques by instead using a large-enough number of pulses to afford similar results. The chosen FM-noise waveform was the pseudo-random optimized (PRO) FM noise radar emission due to it being constant modulus, continuous, and maintaining good spectral spectral containment, unlike traditional noise waveforms with AM effects. Because the PRO-FM waveforms are randomly and independently formed, the simultaneous emission of orthogonal polarizations can be formulated such that with coherent processing over enough pulses (or CW segments) the orthogonally polarized emissions are separable. This eliminates the need to alternate illumination modes and avoids the associated reduction in PRF.

Simultaneous emission also ensures complete coherence between all four co- and cross-polarized returns (HH, HV, VH, and VV).

The use of pre-summing, typically used to aid in the reduction of data requirements for SAR processing, was found to enhance the incoherent combination of sidelobes when processing the received echoes. One thing to note is that the polarization isolation of the test equipment was a limiting factor on the cross-polarized separation performance. Further investigations into these hardware-based performance limitations with antennas offering better isolation is required to experimentally validate the good polarization isolation suggested in simulation. This emission scheme could be applied to other orthogonal polarization modes like right-hand and left-hand circular or $\pm 45^{\circ}$, but would be application specific. These other modes could be implemented via hardware or when designing the waveform pairs. Intuitively, the performance of other polarization modes should mirror the results shown above but experimental validation of these assumptions is required. This simultaneous emission mode could be further enhanced with subsequent polarimetric processing [12, 126] that will be investigated in future work.

An emission scheme mimicking the fixational eye movements observed in mammals was presented that utilized a particular form of active MIMO emission to steer a coherent mainbeam in fast-time. This implementation builds upon previous work on spatial modulation and the waveform diverse array to include an FM-noise emission. Previous work on spatial modulation has classified and derived performance metrics for basic steering shapes. The FEMR emission scheme merged randomness with fast-time beam steering to effectively mimic microsaccades. These microsaccades (or fixational eye movements) occur duing long periods of fixation and are thought to enhance visual acuity by aiding in the resolution of spatial ambiguities. The FEMR emission is formulated to dither about a center-look direction by sampling from any arbitrarily shaped PDF. An independent spatial offset sequence is generated for each new PRO-FM waveform segment to be emitted.

From the simulation results displayed in sections 4.6.1 to 4.6.3 the FEMR emission improves spatial resolution based on the size of the random dithering conducted about the center-look di-

rection. A trade-off between receive SNR and enhanced spatial resolution was also discovered, again based on the PDF used. Implementing multiple consecutive center-look directions in a CW mode was also investigated. The enhanced ability to discriminate between closely spaced targets was also compared to a staring beam and a beamspoiled beam. Experimentally demonstrating the FEMR emission emission scheme using some form of MIMO testbed, whether using a linear or planar array, would provide more insight into the applicability of fast-time beamsteering. Due to the great care with respect to maintaining a continuous and constant modulus signal to each antenna element the implementation of FEMR onto a digital array should be possible with its current form.

References

[1] S. D. Blunt, P. McCormick, T. Higgins, and M. Rangaswamy, "Spatially-modulated radar waveforms inspired by fixational eye movement," in *2014 IEEE Radar Conference*, May 2014, pp. 0900–0905.

[2] R. M. Page, "The early history of radar," *Proceedings of the IRE*, vol. 50, no. 5, pp. 1232–1236, May 1962.

[3] R. J. James, "A history of radar," *IEE Review*, vol. 35, no. 9, pp. 343–349, Oct 1989.

[4] T. K. Sarkar, R. Mailloux, A. A. Oliner, M. Salazar-Palma, and D. L. Sengupta, *A History of Phased Array Antennas*. Wiley-IEEE Press, 2006, pp. 577–.

[5] R. L. Haupt and Y. Rahmat-Samii, "Antenna array developments: A perspective on the past, present and future," *IEEE Antennas and Propagation Magazine*, vol. 57, no. 1, pp. 86–96, Feb 2015.

[6] S. D. Blunt and E. L. Mokole, "Overview of radar waveform diversity," *IEEE Aerospace and Electronic Systems Magazine*, vol. 31, no. 11, pp. 2–42, November 2016.

[7] H. Griffiths, S. Blunt, L. Cohen, and L. Savy, "Challenge problems in spectrum engineering and waveform diversity," pp. 1–5, April 2013.

[8] M. Wicks, E. Mokole, S. Blunt, and B. Schneible, *Principles of Waveform Diversity and Design*. Institution of Engineering and Technology, 2010.

[9] S. Pillai, K. Li, I. Selesnick, and B. Himed, *Waveform Diversity: Theory & Applications: Theory & Application*. McGraw-Hill Education, 2011.

[10] N. Levanon and E. Mozeson, *Radar Signals*, ser. Wiley - IEEE. Wiley, 2004.

[11] D. Giuli, "Polarization diversity in radars," *Proceedings of the IEEE*, vol. 74, no. 2, pp. 245–269, Feb 1986.

[12] D. L. Evans, T. G. Farr, J. J. van Zyl, and H. A. Zebker, "Radar polarimetry: analysis tools and applications," vol. 26, no. 6, pp. 774–789, November 1988.

[13] P. Antonik, M. C. Wicks, H. D. Griffiths, and C. J. Baker, "Frequency diverse array radars," in *2006 IEEE Conference on Radar*, April 2006, pp. 3 pp.–.

[14] P. F. Sammartino, C. J. Baker, and H. D. Griffiths, "Frequency diverse mimo techniques for radar," *IEEE Transactions on Aerospace and Electronic Systems*, vol. 49, no. 1, pp. 201–222, Jan 2013.

[15] E. Fishler, A. Haimovich, R. Blum, D. Chizhik, L. Cimini, and R. Valenzuela, "Mimo radar: an idea whose time has come," in *Proceedings of the 2004 IEEE Radar Conference (IEEE Cat. No.04CH37509)*, April 2004, pp. 71–78.

[16] J. Li, Ed., *MIMO Radar Signal Processing*. Wiley-IEEE Press, 2008.

[17] F. Daum and J. Huang, "Mimo radar: Snake oil or good idea?" *IEEE Aerospace and Electronic Systems Magazine*, vol. 24, no. 5, pp. 8–12, May 2009.

[18] D. J. Rabideau and P. Parker, "Ubiquitous mimo multifunction digital array radar," in *The Thrity-Seventh Asilomar Conference on Signals, Systems Computers, 2003*, vol. 1, Nov 2003, pp. 1057–1064 Vol.1.

[19] A. Balleri, Ed., *Biologically-Inspired Radar and Sonar: Lessons from nature*. Institution of Engineering and Technology, 2017.

[20] J. Jakabosky, S. D. Blunt, and B. Himed, "Waveform design and receive processing for nonrecurrent nonlinear fmcw radar," in *2015 IEEE Radar Conference (RadarCon)*, May 2015, pp. 1376–1381.

[21] C. A. Mohr, P. M. McCormick, and S. D. Blunt, "Optimized complementary waveform subsets within an fm noise radar cpi," in *2018 IEEE Radar Conference (RadarConf18)*, April 2018, pp. 0687–0692.

[22] J. W. Owen, B. Ravenscroft, B. H. Kirk, S. D. Blunt, C. T. Allen, A. F. Martone, K. D. Sherbondy, and R. M. Narayanan, "Experimental demonstration of cognitive spectrum sensing amp; notching for radar," in *2018 IEEE Radar Conference (RadarConf18)*, April 2018, pp. 0957–0962.

[23] B. Ravenscroft, S. D. Blunt, C. Allen, A. Marione, and K. Sherbondy, "Analysis of spectral notching in fm noise radar using measured interference," in *International Conference on Radar Systems (Radar 2017)*, Oct 2017, pp. 1–6.

[24] J. Jakabosky, S. D. Blunt, and A. Martone, "Incorporating hopped spectral gaps into non-recurrent nonlinear fmcw radar emissions," in *2015 IEEE 6th International Workshop on Computational Advances in Multi-Sensor Adaptive Processing (CAMSAP)*, Dec 2015, pp. 281–284.

[25] S. D. Blunt, M. R. Cook, and J. Stiles, "Embedding information into radar emissions via waveform implementation," in *2010 International Waveform Diversity and Design Conference*, Aug 2010, pp. 000 195–000 199.

[26] C. Sahin, J. G. Metcalf, and S. D. Blunt, "Characterization of range sidelobe modulation arising from radar-embedded communications," in *International Conference on Radar Systems (Radar 2017)*, Oct 2017, pp. 1–6.

[27] B. Ravenscroft, P. M. McCormick, S. D. Blunt, J. Jakabosky, and J. G. Metcalf, "Tandem-hopped ofdm communications in spectral gaps of fm noise radar," in *International Conference on Radar Systems (Radar 2017)*, May 2017, pp. 1262–1267.

[28] B. Ravenscroft, P. M. McCormick, S. D. Blunt, E. Perrins, and J. G. Metcalf, "A power-efficient formulation of tandem-hopped radar amp; communications," in *2018 IEEE Radar Conference (RadarConf18)*, April 2018, pp. 1061–1066.

[29] C. Sahin, J. Jakabosky, P. M. McCormick, J. G. Metcalf, and S. D. Blunt, "A novel approach for embedding communications symbols into physical radar waveforms," in *2017 IEEE Radar Conference (RadarConf)*, May 2017, pp. 1498–1503.

[30] C. Sahin, J. G. Metcalf, and S. D. Blunt, "Filter design to address range sidelobe modulation in transmit-encoded radar-embedded communications," in *2017 IEEE Radar Conference (RadarConf)*, May 2017, pp. 1509–1514.

[31] J. Jakabosky, B. Ravenscroft, S. D. Blunt, and A. Martone, "Gapped spectrum shaping for tandem-hopped radar/communications amp; cognitive sensing," in *2016 IEEE Radar Conference (RadarConf)*, May 2016, pp. 1–6.

[32] J. Owen, S. D. Blunt, K. Gallagher, P. McCormick, C. Allen, and K. Sherbondy, "Nonlinear radar via intermodulation of fm noise waveform pairs," in *2018 IEEE Radar Conference (RadarConf18)*, April 2018, pp. 0951–0956.

[33] T. Higgins, K. Gerlach, A. K. Shackelford, and S. D. Blunt, "Aspects of non-identical multiple pulse compression," in *2011 IEEE RadarCon (RADAR)*, May 2011, pp. 895–900.

[34] M. R. Cook, S. D. Blunt, and J. Jakabosky, "Optimization of waveform diversity and performance for pulse-agile radar," in *2011 IEEE RadarCon (RADAR)*, May 2011, pp. 812–817.

[35] T. Higgins, S. D. Blunt, and A. K. Shackelford, "Time-range adaptive processing for pulse agile radar," in *2010 International Waveform Diversity and Design Conference*, Aug 2010, pp. 115–120.

[36] D. Giuli, L. Facheris, M. Fossi, and A. Rossettini, "Simultaneous scattering matrix measurement through signal coding," in *IEEE International Conference on Radar*, May 1990, pp. 258–262.

[37] M. Rolfs, "Microsaccades: Small steps on a long way," *Vision Research*, vol. 49, no. 20, pp. 2415 – 2441, 2009.

[38] E. Ahissar and A. Arieli, "Seeing via miniature eye movements: A dynamic hypothesis for vision," *Frontiers in Computational Neuroscience*, vol. 6, p. 89, 2012.

[39] J. Cui, M. Wilke, N. K. Logothetis, D. A. Leopold, and H. Liang, "Visibility states modulate microsaccade rate and direction," *Vision Research*, vol. 49, no. 2, pp. 228 – 236, 2009.

[40] P. McCormick and S. D. Blunt, "Fast-time 2-d spatial modulation of physical radar emissions," in *2015 16th International Radar Symposium (IRS)*, June 2015, pp. 505–510.

[41] S. D. Blunt, P. Mccormick, T. Higgins, and M. Rangaswamy, "Physical emission of spatially-modulated radar," *IET Radar, Sonar Navigation*, vol. 8, no. 9, pp. 1234–1246, 2014.

[42] G. Zook, P. M. McCormick, and S. D. Blunt, "Fixational eye movement radar: Random spatial modulation," in *2018 IEEE Radar Conference*, May 2018.

[43] P. M. McCormick, T. Higgins, S. D. Blunt, and M. Rangaswamy, "Adaptive receive processing of spatially modulated physical radar emissions," *IEEE Journal of Selected Topics in Signal Processing*, vol. 9, no. 8, pp. 1415–1426, Dec 2015.

[44] J. Jakabosky, P. Mccormick, and S. D. Blunt, "Implementation and design of physical radar waveform diversity," *IEEE Aerospace and Electronic Systems Magazine*, vol. 31, no. 12, pp. 26–33, December 2016.

[45] J. Jakabosky, S. D. Blunt, and B. Himed, "Spectral-shape optimized fm noise radar for pulse agility," in *2016 IEEE Radar Conference (RadarConf)*, May 2016, pp. 1–6.

[46] M. Vespe, G. Jones, and C. J. Baker, "Lessons for radar," *IEEE Signal Processing Magazine*, vol. 26, no. 1, pp. 65–75, Jan 2009.

[47] T. G. Leighton, S. D. Meers, and P. R. White, "Propagation through nonlinear time-dependent bubble clouds and the estimation of bubble populations from measured acoustic characteristics," *Proceedings of the Royal Society of London A: Mathematical, Physical and Engineering Sciences*, vol. 460, no. 2049, pp. 2521–2550, 2004.

[48] C. J. Baker, G. E. Smith, A. Balleri, M. Holderied, and H. D. Griffiths, "Biomimetic echolocation with application to radar and sonar sensing," *Proceedings of the IEEE*, vol. 102, no. 4, pp. 447–458, April 2014.

[49] S. Haykin, Y. Xue, and P. Setoodeh, "Cognitive radar: Step toward bridging the gap between neuroscience and engineering," *Proceedings of the IEEE*, vol. 100, no. 11, pp. 3102–3130, Nov 2012.

[50] M. Richards, J. Scheer, and W. Holm, *Principles of Modern Radar - Volume 1: Basic Principles*. SciTech Publishing, Incorporated, 2010.

[51] M. Richards, W. Holm, W. Melvin, J. Scheer, and J. Scheer, *Principles of Modern Radar: Advanced Techniques*, ser. EBSCO ebook academic collection. Institution of Engineering and Technology, 2012.

[52] M. Richards, W. Melvin, J. Scheer, J. Scheer, and W. Holm, *Principles of Modern Radar: Radar Applications*, ser. Electromagnetics and Radar. Institution of Engineering and Technology, 2014.

[53] M. Skolnik, Ed., *Radar Handbook*, ser. Volume 3. McGraw-Hill, 2008.

[54] R. B. Dybdal, "Radar cross section measurements," *Defense Technical Information Center*, September 1986.

[55] T. Dogaru, L. Nguyen, and C. Le, "Computer models of the human body signature for sensing through the wall radar applications," *Army Research laboratory Technical Reports*, pp. 1–56, September 2007.

[56] S. Stratton and R. Bender, "Radar cross-section (rcs) measurements of a dismount with rocket-propelled grenade (rpg) launcher at ka-band," *Army Research laboratory Technical Reports*, pp. 1–45, July 2006.

[57] C. Kenyon and T. Dogaru, "Numerical computation of the radar cross section of rockets and artillery rounds," *Army Research laboratory Technical Reports*, pp. 1–32, September 2015.

[58] M. Skolnik, *Introduction to Radar Systems*. Tata McGraw Hill, 2001.

[59] N. Willis, *Bistatic radar*, ser. Artech House radar library. Artech House, 1991.

[60] R. A. Heising, "Modulation in radio telephony," *Proceedings of the Institute of Radio Engineers*, vol. 9, no. 4, pp. 305–352, Aug 1921.

[61] D. M. Hemmingsen, P. M. McCormick, S. D. Blunt, C. Allen, A. Martone, K. Sherbondy, and D. Wikner, "Waveform-diverse stretch processing," in *2018 IEEE Radar Conference (RadarConf18)*, April 2018, pp. 0963–0968.

[62] C. D. Graves, "Radar polarization power scattering matrix," vol. 44, no. 2, pp. 248–252, Feb 1956.

[63] R. C. Jones, "A new calculus for the treatment of optical systems, i. description and discussion of the calculus," *J. Opt. Soc. Am.*, vol. 31, no. 7, pp. 488–493, Jul 1941.

[64] H. Hurwitz and R. C. Jones, "A new calculus for the treatment of optical systems, ii. proof of three general equivalence theorems," *J. Opt. Soc. Am.*, vol. 31, no. 7, pp. 493–499, Jul 1941.

[65] R. C. Jones, "A new calculus for the treatment of optical systems, iii. the stokes theory of optical activity," *J. Opt. Soc. Am.*, vol. 31, no. 7, pp. 500–503, Jul 1941.

[66] G. G. Stokes, "On the composition nad resolution of streams of polarized light from different sources," *Transactions of the Cambridge Philosophical Society*, vol. 9, pp. 199–416, 1852.

[67] M. Born and E. Wolf, *Principles of Optics*, 3rd ed. Pergamon Press, 1965.

[68] G. A. Emmons and P. M. Alexander, "Polarization scattering matrices for polarimetric radar," *Defense Technical Information Center*, March 1983.

[69] J. S. Ussailis, L. A. Leiker, R. M. G. IV, and J. I. Metcalf, *Defensive Technical Information Center*, July 1982.

[70] P. McCormick, J. Jakabosky, S. D. Blunt, C. Allen, and B. Himed, "Joint polarization/waveform design and adaptive receive processing," in *2015 IEEE Radar Conference (RadarCon)*, May 2015, pp. 1382–1387.

[71] D. Henke, P. McCormick, S. D. Blunt, and T. Higgins, "Practical aspects of optimal mismatch filtering and adaptive pulse compression for fm waveforms," in *2015 IEEE Radar Conference (RadarCon)*, May 2015, pp. 1149–1155.

[72] P. M. McCormick and S. D. Blunt, "Shared-spectrum multistatic radar: Experimental demonstration using fm waveforms," in *2018 IEEE Radar Conference (RadarConf18)*, April 2018, pp. 0929–0934.

[73] W. L. Melvin, "A stap overview," *IEEE Aerospace and Electronic Systems Magazine*, vol. 19, no. 1, pp. 19–35, Jan 2004.

[74] G. W. Stallibrass, "Some navigational and air traffic control problems of civil aviation and the application of radio to their reduction," *Radio Engineers, Journal of the British Institution of*, vol. 12, no. 1, pp. 3–, January 1952.

[75] "Air traffic control systems," *IEEE Aerospace and Electronic Systems Magazine*, vol. 15, no. 10, pp. 70–78, Oct 2000.

[76] R. J. Fitzgerald, "Effects of range-doppler coupling on chirp radar tracking accuracy," *IEEE Transactions on Aerospace and Electronic Systems*, vol. AES-10, no. 4, pp. 528–532, July 1974.

[77] F. J. Harris, "On the use of windows for harmonic analysis with the discrete fourier transform," *Proceedings of the IEEE*, vol. 66, no. 1, pp. 51–83, Jan 1978.

[78] S. Benedetto and E. Biglieri, *Principles of digital transmission: with wireless applications*, ser. Information technology, transmission, processing, and storage. Springer US, 2006.

[79] J. Ward, "Space-time adaptive processing for airborne radar," *Lincoln Lab Tech. Report*, December 1994.

[80] P. M. McCormick, S. D. Blunt, and J. G. Metcalf, "Simultaneous radar and communications emissions from a common aperture, part i: Theory," in *2017 IEEE Radar Conference (RadarConf)*, May 2017, pp. 1685–1690.

[81] P. M. McCormick, B. Ravenscroft, S. D. Blunt, A. J. Duly, and J. G. Metcalf, "Simultaneous radar and communication emissions from a common aperture, part ii: Experimentation," in *2017 IEEE Radar Conference (RadarConf)*, May 2017, pp. 1697–1702.

[82] P. M. McCormick, S. D. Blunt, and J. G. Metcalf, "Wideband mimo frequency-modulated emission design with space-frequency nulling," *IEEE Journal of Selected Topics in Signal Processing*, vol. 11, no. 2, pp. 363–378, March 2017.

[83] ——, "Joint spectrum/beampattern design of wideband fm mimo radar emissions," in *2016 IEEE Radar Conference (RadarConf)*, May 2016, pp. 1–6.

[84] H. Van Trees, *Optimum Array Processing: Part IV of Detection, Estimation, and Modulation Theory*, ser. Detection, Estimation, and Modulation Theory. Wiley, 2004.

[85] W.L. Stutzman and G.A. Thiele, *Antenna theory and design*, John Wiley amp; Sons, 2012.

[86] D. F. Kelley and W. L. Stutzman, "Array antenna pattern modeling methods that include mutual coupling effects," *IEEE Transactions on Antennas and Propagation*, vol. 41, no. 12, pp. 1625–1632, Dec 1993.

[87] R. Hansen, *Phased Array Antennas*, ser. Wiley Series in Microwave and Optical Engineering. Wiley, 2009.

[88] H. Holter and H. Steyskal, "On the size requirement for finite phased-array models," *IEEE Transactions on Antennas and Propagation*, vol. 50, no. 6, pp. 836–840, Jun 2002.

[89] J. C. Kerce, G. C. Brown, and M. A. Mitchell, "Phase-only transmit beam broadening for improved radar search performance," in *2007 IEEE Radar Conference*, 2007.

[90] R. Barker, "Group synchronization of binary digital systems," *Butterworth Scientific Publications*, pp. 273–287, 1953.

[91] *Specifications of the Bluetooth System*, Special Interest Group, Nov 2003.

[92] *IRIG Standard 106–00: Telemetry Standards, Range Commanders Council Telemetry Group*, Range Commanders Council, White Sands, Missle Range, New Mexico.

[93] *Bandwidth-Efficient Modulations: Summary of Definitions, Implementations, and Performance*, Report Concerning Space Data System Standards, Informational Report CCSDS 413.0-G-2.

[94] S. Blunt, M. Cook, E. Perrins, and J. de Graaf, "Cpm-based radar waveforms for efficiently andlimiting a transmitted spectrum," in *2009 IEEE Radar Conference*, May 2009, pp. 1–6.

[95] S. D. Blunt, M. Cook, J. Jakabosky, J. D. Graaf, and E. Perrins, "Polyphase-coded fm (pcfm) radar waveforms, part i: implementation," *IEEE Transactions on Aerospace and Electronic Systems*, vol. 50, no. 3, pp. 2218–2229, July 2014.

[96] S. D. Blunt, J. Jakabosky, M. Cook, J. Stiles, S. Seguin, and E. L. Mokole, "Polyphase-coded fm (pcfm) radar waveforms, part ii: optimization," *IEEE Transactions on Aerospace and Electronic Systems*, vol. 50, no. 3, pp. 2230–2241, July 2014.

[97] J. Jakabosky, P. Anglin, M. R. Cook, S. D. Blunt, and J. Stiles, "Non-linear fm waveform design using marginal fisher's information within the cpm framework," in *2011 IEEE Radar-Con (RADAR)*, May 2011, pp. 513–518.

[98] J. Jakabosky, S. D. Blunt, M. R. Cook, J. Stiles, and S. A. Seguin, "Transmitter-in-the-loop optimization of physical radar emissions," in *2012 IEEE Radar Conference*, May 2012, pp. 0874–0879.

[99] L. Ryan, J. Jakabosky, S. D. Blunt, C. Allen, and L. Cohen, "Optimizing polyphase-coded fm waveforms within a linc transmit architecture," in *2014 IEEE Radar Conference*, May 2014, pp. 0835–0839.

[100] J. Jakabosky, S. D. Blunt, and B. Himed, "Optimization of "over-coded" radar waveforms," in *2014 IEEE Radar Conference*, May 2014, pp. 1460–1465.

[101] P. S. Tan, J. Jakabosky, J. M. Stiles, and S. D. Blunt, "2015," in *2015 IEEE Radar Conference (RadarCon)*, May 2015, pp. 0467–0472.

[102] P. S. Tan, J. M. Stiles, and S. D. Blunt, "Physically realizing an optimized sparse spectrum via joint design of a collection of fm waveforms," in *2018 IEEE Radar Conference (RadarConf18)*, April 2018, pp. 0703–0708.

[103] P. M. McCormick and S. D. Blunt, "Nonlinear conjugate gradient optimization of polyphase-coded fm radar waveforms," in *2017 IEEE Radar Conference (RadarConf)*, May 2017, pp. 1675–1680.

[104] ——, "Gradient-based coded-fm waveform design using legendre polynomials," in *International COnference on Radar Systems (Radar 2017)*, Oct 2017, pp. 1–6.

[105] C. A. Mohr, P. M. McCormick, S. D. Blunt, and C. Mott, "Spectrally-efficient fm noise radar waveforms optimized in the logarithmic domain," in *2018 IEEE Radar Conference (RadarConf18)*, April 2018, pp. 0839–0844.

[106] J. Jakabosky, S. D. Blunt, and T. Higgins, "Ultra-low sidelobe waveform design via spectral shaping and linc transmit architecture," in *2015 IEEE Radar Conference (RadarCon)*, May 2015, pp. 1021–1026.

[107] V. Bringi and V. Chandrasekar, *Polarimetric Doppler Weather Radar: Principles and Applications*. Cambridge University Press, 2001.

[108] Y. Xu, R. M. Narayanan, X. Xu, and J. O. Curtis, "Polarimetric processing of coherent random noise radar data for buried object detection," *IEEE Transactions on Geoscience and Remote Sensing*, vol. 39, no. 3, pp. 467–478, Mar 2001.

[109] R. M. Narayanan and C. Kumru, "Implementation of fully polarimetric random noise radar," *IEEE Antennas and Wireless Propagation Letters*, vol. 4, pp. 125–128, 2005.

[110] L. Maslikowski, K. Kulpa, D. Glushko, and F. Yanovsky, "Atmospheric precipitation sensing with a short-range c-band noise radar," in *2013 14th International Radar Symposium (IRS)*, vol. 2, June 2013, pp. 791–798.

[111] A. Stove, G. Galati, G. Pavan, F. D. Palo, K. Lukin, K. Kulpa, J. S. Kulpa, and . Maślikowski, "The nato set-184 noise radar trials," in *2016 17th International Radar Symposium (IRS)*, May 2016, pp. 1–6.

[112] G. Zook, P. M. McCormick, S. D. Blunt, C. Allen, and J. Jakabosky, "Dual-polarized fm noise radar," in *2017 IET International Conference on Radar Systems*, 2017.

[113] *Parabolic Reflector*, KP Performance Antennas.

[114] *AWG70000 Arbitrary Waveform Generator*, Tektronix, August 2015, primary user manual.

[115] E. Analog Devices Inc. and W. Kester, *Mixed-signal and DSP Design Techniques*, ser. Analog Devices series. Elsevier Science, 2003.

[116] W. Brown, G. Houser, and R. Jenkins, "Synthetic aperture processing with limited storage and presumming," *IEEE Transactions on Aerospace and Electronic Systems*, vol. AES-9, no. 2, pp. 166–176, March 1973.

[117] T. Higgins and S. D. Blunt, "Analysis of range-angle coupled beamforming with frequency-diverse chirps," in *2009 International Waveform Diversity and Design Conference*, Feb 2009, pp. 140–144.

[118] W. Q. Wang, H. C. So, and A. Farina, "An overview on time/frequency modulated array processing," *IEEE Journal of Selected Topics in Signal Processing*, vol. 11, no. 2, pp. 228–246, March 2017.

[119] G. E. Moore, "Cramming more components onto integrated circuits," *Proceedings of the IEEE*, vol. 86, no. 1, pp. 82–85, Jan 1998.

[120] S. G. Marconi, "Radio telegraphy," *Proceedings of the Institute of Radio Engineers*, vol. 10, no. 4, pp. 215–238, Aug 1922.

[121] J. Simmons and R. A. Stein, "Acoustic imaging in bat sonar: Echolocation signals and the evolution of echolocation," vol. 135, pp. 61–84, 03 1980.

[122] J. A. Simmons and J. E. Gaudette, "Special section on biologically-inspired radar and sonar systems - bbiosonar echo processing by frequency-modulated bats," *IET Radar, Sonar Navigation*, vol. 6, no. 6, pp. 556–565, July 2012.

[123] M. J. Wohlgemuth, J. Luo, and C. F. Moss, "Three-dimensional auditory localization in the echolocating bat," *Current Opinion in Neurobiology*, vol. 41, pp. 78 – 86, 2016, microcircuit computation and evolution.

[124] T. R. Neil, "The biosonar arms race between bats and insects."

[125] J. F. Vincent, O. A. Bogatyreva, N. R. Bogatyrev, A. Bowyer, and A.-K. Pahl, "Biomimetics: its practice and theory," *Journal of The Royal Society Interface*, vol. 3, no. 9, pp. 471–482, 2006.

[126] R. Touzi, S. Goze, T. L. Toan, A. Lopes, and E. Mougin, "Polarimetric discriminators for sar images," vol. 30, no. 5, pp. 973–980, September 1992.